UCLouvain

École polytechnique de Louvain

Development and numerical assessment of an analytical model for dose estimation in FLASH proton therapy with 3D range modulators

Author: **Elisa DEVRESSE**
Supervisor: **John LEE**
Readers: **Edmond STERPIN, Sylvain DEFFET**
Academic year 2021–2022
Master [120] in Mathematical Engineering

Acknowledgements

I would like to thank my supervisor, John Lee, for his comments and suggestions on the writing of the thesis. Thank you for giving me the opportunity to work on this topic.

I would especially like to thank Sylvain Deffet for his time, help and guidance throughout the project. The numerous meetings allowed me to stay on course and to progress in the realization of the research.

I would also like to thank Prof. Edmond Sterpin for taking the time to participate on the jury.

Thanks to my family for their support during this year and my friends also working on their thesis that helped me to keep going.

Abstract

Radiation therapy is one of the oldest and most used treatments for cancer. Recently, a new technique using ultra-high dose rates called FLASH proton therapy showed promising results for the treatment of cancer with advantages over the conventional method. A patient specific range modulator must be modelized to match the Spread Out Bragg Peak (SOBP) with the tumor to treat. However, the most accurate existing simulations models use Monte Carlo and are too slow. The aim of this work is to develop an analytical model that gives acceptable results with a 3D range modulator in an reasonable time. The realization of this model is mainly based on the convolution principle. The scattering of the beam as it penetrates the water is modeled by successive convolutions of the beam with a Gaussian whose standard deviation has been calculated using MCsquare. The other central element of the simulation is the energy loss also coming from a model like MCsquare instead of a database like PSTAR to take into account the range straggling phenomenon. The results of the studied model are consistent and can be used to get a first idea of the dose distribution in a reasonable time. But they are not sufficiently accurate for a direct clinical use. Moreover, the study of geometrical characteristics of the range modulator shows their importance for the dose distribution and gives perspectives for future use of this model. Finally, it allows, in an acceptable time, a vizualisation of the individual impact of each element constituting a range modulator. This can help to better understand the advantages and disadvantages of each possible configuration. This analytical model is a tool to simulate more quickly a proton beam. It may contribute to find the shape of the 3D range modulator allowing the desired dose distribution .

Keywords: Radiotherapy, FLASH Proton therapy, 3D range modulator, analytic, MCsquare

Contents

List of Figures

List of Tables

1

Introduction

Today, cancer is one of the most common causes of death. Many treatments have been developed over the past few decades. One of the treatments available today is radiation therapy. This is based on radiation of the tumor from an external source in most cases. However, this type of procedure requires a balance between controlling the tumor and limiting toxicity to healthy tissue. The most commonly used particles today are photons and electrons. Nevertheless, new heavier particles such as protons have shown to have interesting properties for cancer treatment.

The photon, like the electron, will lose a large part of its energy at low thickness in the patient. The proton unlike the lighter particles loses its energy at a certain depth at the end of the proton path followed by an exponential decrease. The characteristic dose curve of the proton is called the Bragg peak and allows the dose to be reduced before and after the target. The attractiveness of proton therapy is explained by the physics of the proton but also by the biological impact during the treatment. The use of heavier particles has been shown to have indeed more impact on cells [8].

The distribution of dose can be modified by playing with several Bragg peaks and deposit the dose at the desired location. The volume of a tumor requires irradiating a larger area laterally and longitudinally than what a single energy proton beam can do. This dose stretching is called Spread-out Bragg Peak (SOBP). The Bragg superposition increases the dose before the tumor but is still much smaller than with photons or electrons. For this reason, proton therapy will be favored in the treatment of childhood cancer [20] but also in certain types of cancer such as prostate cancer, lung cancer, etc [5]. Nowadays, the most commonly used delivery system is pencil beam scanning [21]. This will go through the tumor layer by layer and allows a complex dose distribution. However, to achieve several bragg peaks of different depths, it is necessary to change the beam energy. This change of energy takes some time. This time difference adds uncertainty to the range. Uncertainties are important to take into account especially in the case of proton therapy. A bad management of the uncertainties in the range can indeed lead to an overdose of the healthy tissues or an underdose of the tumor.

Recently, it has been discovered that the use of ultra-high dose radiation therapy (FLASH therapy) can attack the tumor in the same way while limiting the harmful effect on the surrounding healthy tissue [22]. The use of FLASH also decrease the uncertainty created by the time delivery. We will focus here on FLASH proton therapy. This method is characterized by a dose higher than 40 Gy/s compared to the conventional dose rate of 5 Gy/min [23]. Several studies have been conducted on the subject and show the benefits of this new technique [24, 25]. However, the explanation behind this phenomenon remains unknown and is still under research [5, 26]. The creation of SOBP in this case must be created passively. Simeonov's study [9] was interested in the development of a 3D range modulator to create a highly conformal dose with one mono-energetic beam.

Different models already exist to simulate a proton beam. The most efficient ones are those using Monte Carlo. However, these methods are slower. For this reason, a fast Monte Carlo model named MCsquare has been developed. If using Monte Carlo increases the execution time one idea would be to use an analytic model. However, while the existing analytical models are certainly faster, they give less accurate results. The development of a fast and accurate enough model for clinical use would be beneficial to the cancer research.

The goal of this thesis is to develop an analytic model that allows finding results in a reasonable time. In a second time, we will use this model to study the effect of the geometrical characteristics of the 3D range modulator on the dose distribution. In this context, we will study in detail the impact of each part of the beam on the target.

More specifically, this research aims to create an analytical model that:

- transcribes the modeling of proton beam transport by simple steps,
- allows to find results faster than in a classical Monte Carlo model,
- allows to analyze initial fluences other than Gaussian,
- allows to isolate the contribution of each part of the initial fluence on the final dose distribution in an acceptable time.

The second aim of this thesis is to show examples of what it can model and see the benefits it brings. To achieve this, this thesis is divided into 7 parts.

- The first part gives a brief overview on radiotherapy. It is here that we present the scourge of cancer and everything that is around the treatment of radiotherapy including proton therapy and FLASH proton therapy. In this section, we will show why the use of FLASH proton therapy is so promising.
- The second part explains the physics behind proton therapy and specifically the behavior of protons in matter. In addition, we will present a central term of the model, the water equivalence.
- The third part presents the mathematics of proton transport and how we model it. We begin with the simple example of a mono energetic beam to then move on the more complex case of a multi-energy beam. The FLASH proton therapy is based on the creation of multi energetic beam from a range modulator to create a SOBP.
- The fourth part presents the parameters and components used in our simulation.
- The fifth part analyzes the results of the basic and known situation and compares them with the ones found by MCsquare. This part allows us to validate our model.
- The sixth part contains the results of all the simulations and research done with our model. The results are divided into two parts. First we look at the impact of a multiple pyramidal shape vs a simple pyramidal shape on the distribution dose. Then, we isolate one point of the initial fluence to see its effect on the dose distribution.

- The seventh part conclude our thesis with a discussion of these results and the vision of what this model can bring in the future.

The present analysis will show that there is some potential for improvement in the time delivery of results using this model. We are convinced that, while work remains to be done to develop an effective model, this could be used to propose a first version of range modulator which can then be introduced in a more accurate model like MCsquare.

2

Radiotherapy

In this chapter, we will briefly introduce one of the most frequent causes of death, cancer. In this context, we will also present the treatments which have been developed over the years in the fight against cancer, radiotherapy in particular. After an explanation of the main characteristics of radiotherapy, we will see the different possible side effects of this therapy, which will allow us to understand the intensive search for solutions which limit the effects on the human body. In recent years, the development of proton therapy, a type of radiotherapy, has been growing. In this context, researchers developed new techniques like FLASH proton therapy. We will highlight the benefits of these new techniques and highlight the advances in this area.

2.1 Cancer

Cancer is one of the leading causes of death in the world, causing almost one in six deaths worldwide by 2020 [27]. Scientists have been searching for effective treatments for over a century. One of the known techniques is chemotherapy, which has been used since the 1930s [28].

This disease is characterized by uncontrolled growth of cells that will later shape tumors. Two types of tumors can develop: malignant or benign tumors. The first type is cancerous. Once cancerous cells are formed, they can migrate to other sites by metastasis. This characteristic of spread is what differentiates benign tumors from cancer.

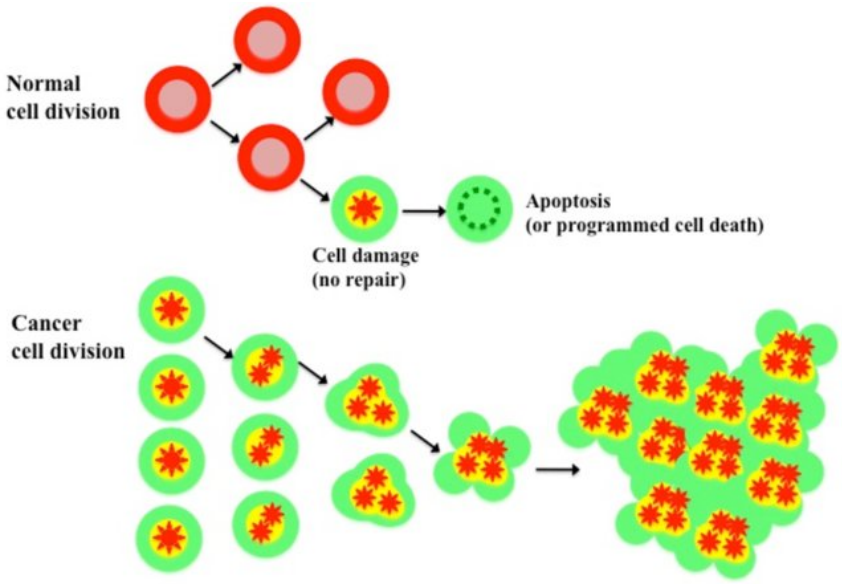

Figure 1: *Schematic of normal cell (above) and cancer cell division (below) [1].*

Cell renewal normally manages to find a balance between the activity of the genes that allow proliferation and the genes that suppress it. DNA mutations can have no effect or cause a deregulation of the cell division

system [8]. When the DNA is damaged the cancerous cells won't be repaired or die, but will continue to grow and shape abnormal cells (see Figure 1).

There exist several treatment options: radiotherapy, surgery, chemotherapy, etc. The choice of treatment will depend on the type of cancer and its stage. The location of the tumor is important due to the radiosensitivity of the different healthy and cancerous cells. The chosen treatment can be either one or a combination of the options.

2.2 Basic concept of Radiotherapy

Medicine has used radiotherapy as a cancer treatment for over a century. Nowadays it treats around 50% of cancer [11]. It is called a local treatment because it affects the cells only in the treated area. Two types of therapy can be differentiated: internal and external therapy. The source can either be placed inside the patient or can be administrated by a beam of radiation generated outside the patient.

The aim of radiotherapy is to destroy all cancer cells and is based on ionizing radiation [1]. Different types of particles can irradiate patients, and each will have various physical interactions. For charged particles, the main interaction with the tissue is through an ionization process. Conversely, for neutral particles, it is by generating secondary charged particles which will then deposit energy through ionization [8].

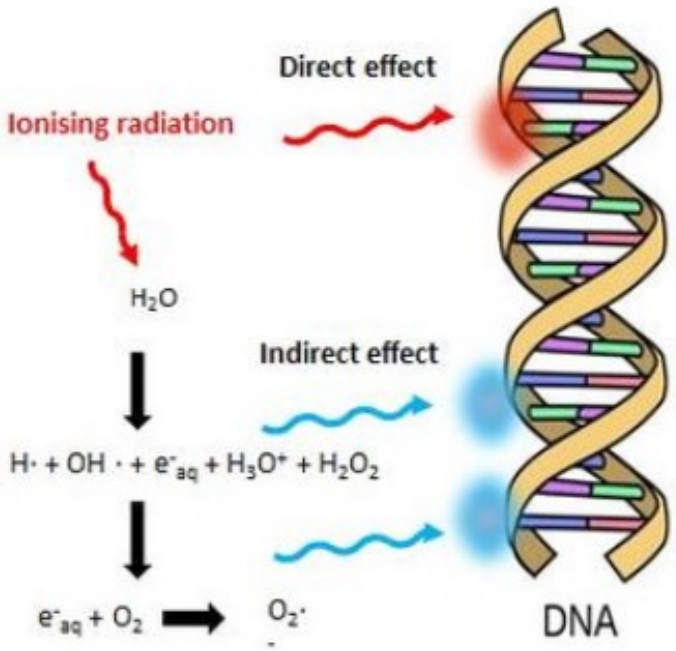

Figure 2: *Schematic of how ionizing radiation utilized for radiotherapy can damage DNA [2].*

DNA plays a key role in the treatment due to its high sensitivity to radiation. It can be seen in Figure 2 that the radiation will either damage the DNA directly or indirectly via the generation of reactive oxygen species.

[1] Radiation that has enough energy to ionize a molecule by detaching an electron.

When a cell is damaged, our DNA provides for a repair system, which is automatically initiated. The goal of radiotherapy is to destroy enough of the DNA so that the repair fails, and the cell dies. The treatment will be divided into 30 to 40 daily fractions to improve the therapeutic advantage as compared to a single delivery. It gives more time for the healthy cells to repair their DNA [8].

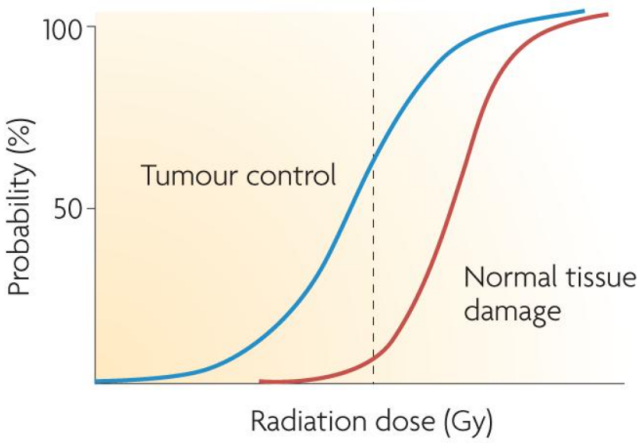

Figure 3: *Probability of tumor cure and late normal tissue damage [3].*

In theory, since the probability to destroy the cell grows with the increase of the dose, the more the tumor is irradiated the better. However, as radiation also kills healthy cells, it is important to strike a balance between curing the disease and limiting the effect of this treatment on the patient. To achieve this, we must look at the absorbed dose in the tumor but also in the tissues around it. However, there seems to be a favorable difference between the radiation of the normal and malignant cells. Indeed, the reparation mechanism of healthy cells is more efficient. Figure 3 shows this differentiated impact of an increase of the radiation on the probability of tumor control[2] and the probability of severe late normal tissue damage[3]. It remains vital to try to limit the effect of the therapy on healthy cells. It is to improve the quality of life of patients that new technologies like intensity-modulated radiotherapy have been developed [3] and are used to match up to the shape of the tumor. One of the new advanced technologies is the use of heavier particle like proton and carbon.

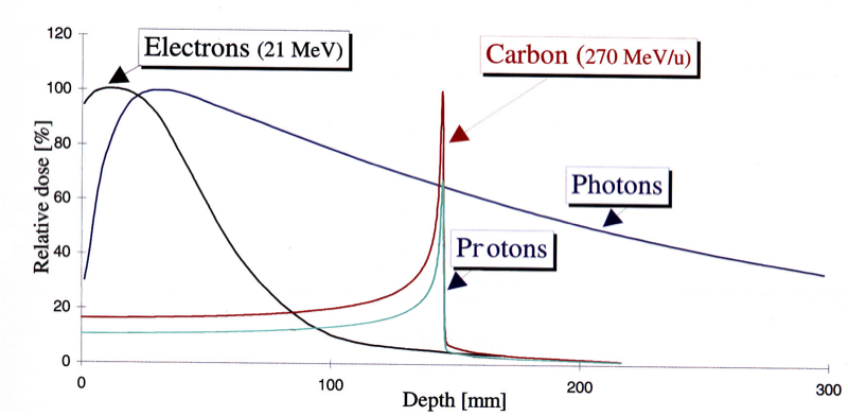

Figure 4: *Energy deposit by different particles as they penetrate matter [4].*

[2]The tumor control probability is the probability that a certain dose kill the tumor cell.
[3]The normal tissue damage probability is the probability that a certain dose will lead to complication due to radiation toxicity.

Several type of particles can be used. Figure 4 shows that the energy deposited at a certain depth will depend on the type of particle we use and at what energy. The X-ray beam is the most used radiation delivery method. However, photons are uncharged particles and loose a significant portion of the energy at the beginning and the more it penetrates the matter, the less energy is absorbed. Due to this curve trend, it will be necessary to have a high enough energy at the start to deliver the necessary absorbed dose at the tumor. This implies that the cells on the way to the tumor will be strongly irradiated and damaged. The same can be observed with electrons. This type of curve is the biggest disadvantage of photons and electrons compared to heavier charged particle, such as protons. One advantage of protons is indeed its dose curve shape and its Bragg peak (the marked spike of the curve). This allows irradiating mainly in the tumor while limitating the effects on healthy cells located behind the tumor (see Figure 5). Moreover, the relative dose is much lower before than with photons. Despite the clear appeal of protons, today most radiotherapy uses photons and electrons due to the advanced technology with these particles. However, the use of proton therapy has intensified over recent years [29].

One way to decrease the absorbed dose in healthy tissue is to send beams from different locations and thus divide the energy by the number of beams sent (see on the left of Figure 5). The aim is to irradiate as uniformly as possible, while decreasing the impact on healthy cells. Dose inhomogeneity has been shown to be inefficient in the idea that the tumor control probability will be lower than with a uniformly mean dose [30].

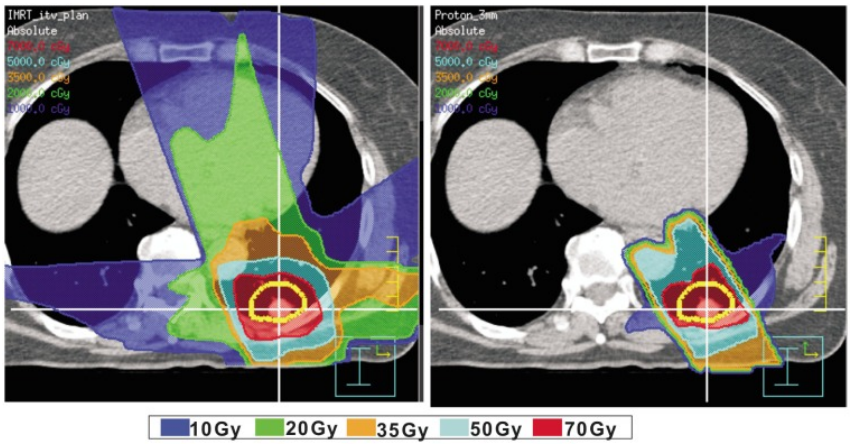

Figure 5: *Comparison of photon intensity-modulated radiation therapy plan (left) and proton therapy plan (right) [5].*

2.3 Side Effects

As explained above, the principle of radiotherapy is to kill cells. It is therefore important to limit the damage to healthy cells and prevent the destruction of organs. Radiotherapy has two types of effect: deterministic and stochastic. The cell death of tissue is the deterministic effect of radiotherapy. The dose threshold for these effects is comprised between 0.15 and 10 Gy [31]. On the other hand, The stochastic effect are defined by the permanent DNA alteration. It can cause genetic changes and cancer [31]. However, it is not possible to define a threshold dose for the stochastic effects.

In Table 1 we can see a gradation of the possible side effects, from 0 with no effect to 5 with death. Most of

the patients will suffer of at least skin toxicity.

Grade	Observation
0	No change over baseline
1	Follicular, faint or dull erythema/epilation/dry desquamation/decreased sweating
2	Tender or bright erythema, patchy moist desquamation/ moderate edema
3	Confluent moist desquamation other than skin folds, pitting edema
4	Ulceration, hemorrhage, necrosis
5	Any toxicity which causes death

Table 1: *Radiation therapy toxicity grading [19].*

2.4 Proton therapy

The history of proton therapy began in 1946, when Robert R. Wilson first outlines the advantages of proton radiation therapy [32]. Proton therapy, as already mentioned, has a more advantageous dose profile and has a reduced total energy deposited in the patient compared to photon techniques. The curve shape permits indeed a maximum dose delivery at the tumor and a lower dose in normal tissue. Protons are more interesting for the reasons outlined above but also for biological reasons. Some radiation types are biologically more efficient than others. For the same delivered physical dose, the biological damage of heavier charged particles has higher effect. This effect can be quantified by the relative biological effectiveness (RBE). Accordingly, protons will have 1.1 more effect than photons [8].

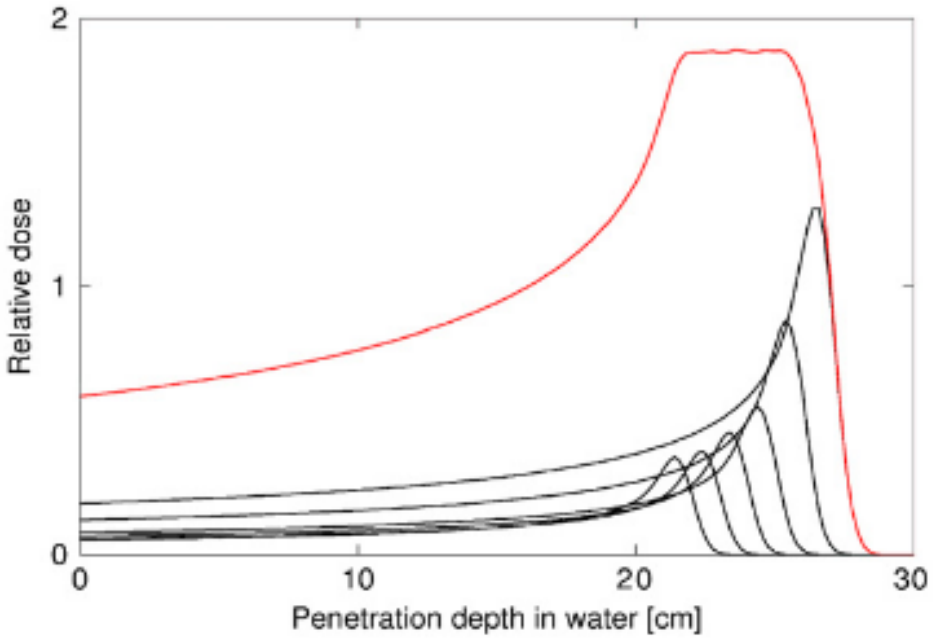

Figure 6: *Spread-out Bragg peak created by combining 6 beams with different energies [6].*

Moreover, we can play on the superposition of several pristine Bragg curve [4] to shape a spread-out Bragg peak (SOBP). The spread-out Bragg peak allows us to play with the depth of the uniform dose distribution and to irradiate a larger tumor volume. To perform this uniform dose the peak should not be equally weighted (see Figure 6). The more proximal the peak is, the less weight it should have [30]. The SOBP induces a higher dose before the Bragg peak, but it is still lower than with X-rays.

Proton therapy has led to important medical breakthroughs, partly in the treatment of tumors for children because their tissue is more sensitive to radiation [20], but also in the treatment of certain types of cancer like prostate cancer, lung cancer , etc [5]. Indeed, the fact that proton therapy can reduce the dose to the adjacent normal tissue makes it one of the principal ion treatments proposed in these cases [5].

As with other types of radiation therapy, the dose administered must be such that the surrounding tissue is affected as little as possible. This can be achieved by changing the number of beams delivered with different locations and modulating the intensity of the beam.

2.4.1 Facility

One of the main reasons explaining the limited use of proton therapy is the facility required for the treatment. Indeed, the cost and size (more or less 30M/55M [33]) of the facility makes it difficult to develop.

The first part of the facility is an accelerator. In this case, it is a cyclotron (the upper part of Figure 7) which will generate and accelerate the protons to a certain energy, efficient for the treatment. This process can be divided in two steps. First, we use an electric field to separate the proton and the electron of a hydrogen molecule [5]. In a second step, a magnetic field and a voltage differential is maintained constant to permit the protons to move in a circle and gain energy.

Since the cyclotron produce protons at a fixed energy, a beam degrader can be used to change the energy of the beam. To spread out the beam, a modulator wheel permits to produce different levels of energy which will stop at different depth (see the spread out Bragg peak in Figure 6) [34]. These processes will have the combined effects of reducing the energy and scattering the beam.

A beam transport system directs the beam from the accelerator to the treatment delivery system using magnets. The gantry enables to direct the beam line exactly on the tumor thanks to the 360° rotation. The gantry and the space at the center of it must be quite large. It needs enough space for the patient and all imaging equipment indeed.

The last part is called the nozzle and delivers the protons. It is composed of different components depending on the type of delivery. This delivery system will be passive or active and permits to cover the lateral extent of the tumor [35]. An example of passive delivery system is the double scattering (DBS) which have several issues. The use of a passive scattering produces a lot of secondary neutrons. Many of them can contribute to

[4] A pristine Bragg curve is a Bragg curve of a mono-energetic proton beam.

the whole body dose to the patient and may increase the incidence of secondary tumors [5]. Nowadays, proton therapy tends to use an active delivery system called pencil beam scanning.

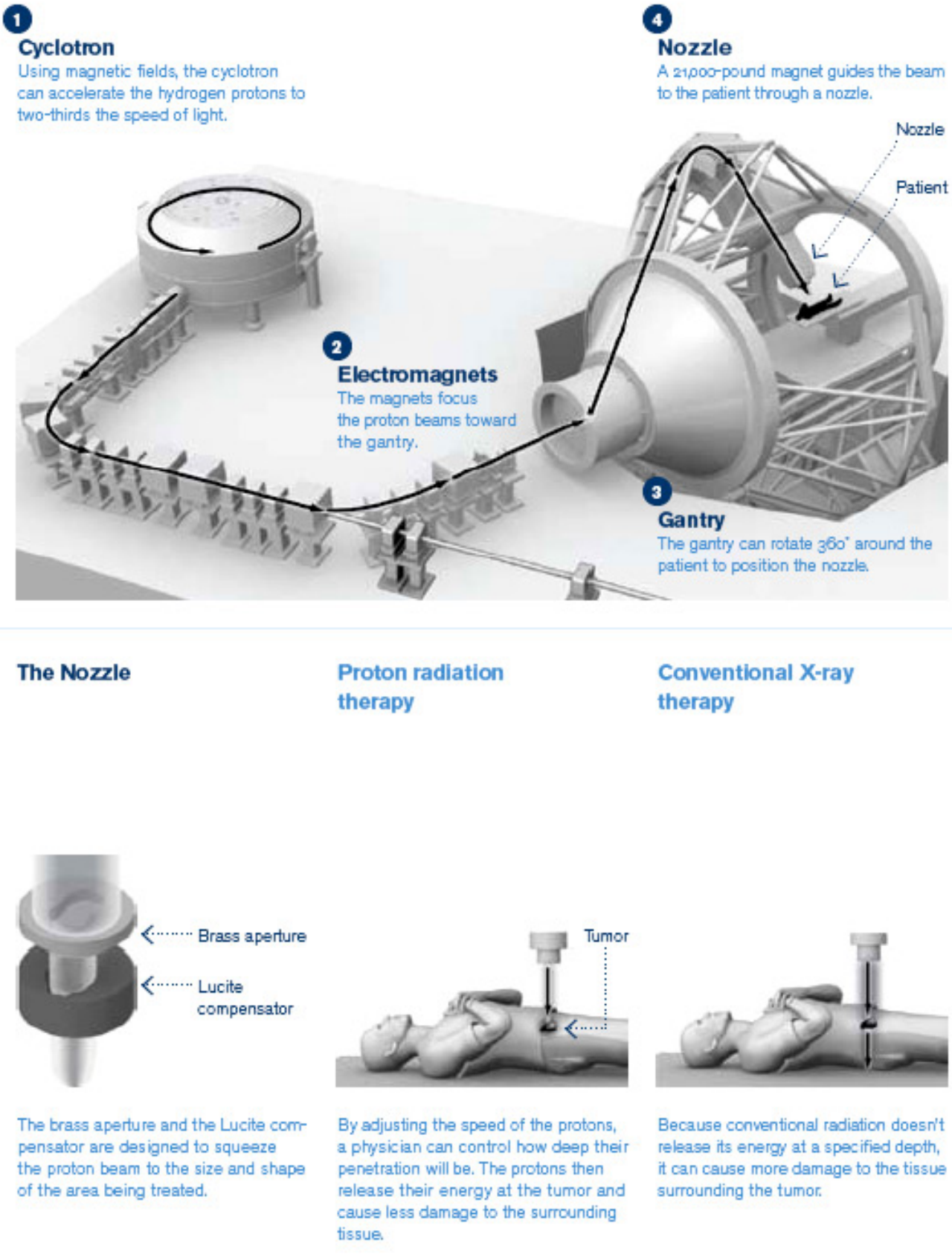

Figure 7: *Composition of the facility for Proton therapy (above) and zoom on the nozzle and the patient (below) [7].*

2.4.2 Pencil Beam Scanning

Pencil Beam Scanning is the newest delivery system for proton therapy and provide a more conformal dose distribution to the target volume than traditional proton double scattering and uniform scanning technique [21]. It goes through the cancer layer by layer (see Figure 8). In this technique we can adjust the magnetic energy according to actual need for a specific tumor. Other factors can be adapted such as the depth, the maximum energy, the width, etc.

A proton beam is moved using magnetic scanning while adapting the intensity to produce the planned dose frame by frame where each corresponds to one energy [36]. Using a pencil beam scanning permits to deliver a more complex heterogeneous dose distribution.

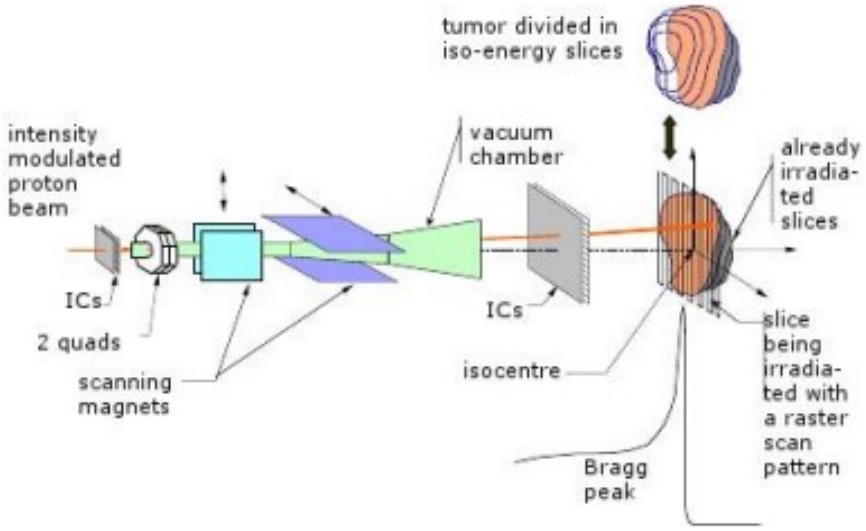

Figure 8: *Representation of a proton beamline with pencil beam scanning delivery [8]*

In this technique, the pencil beam is not scattered before being sent to the patient. It gives this sharp Bragg peak [5] which is the desired behavior. However, to irradiate the totality of the tumor it is necessary to send beams of different energies. Between each of them a certain time elapse. This time lapse is important because it may affect the homogeneity of the dose, i.e. the longer between two beams, the more likely the patient will move and hence the more uncertainties we will have.

2.4.3 Uncertainties

Uncertainty in the range is an important problem to consider especially with proton beam. Indeed, unlike with the photons where the maximum dose is deposited at the beginning, the proton will lose his energy mostly just before the range. The uncertainties are multiple depending on if we are in a moving or a static geometry. There are two types of uncertainties: systematics errors that reduce the accuracy of processing and random errors that occur from time to time and reduce the precision [8].

[5] An explanation of the reason why a scattered beam will cause a less sharp Bragg peak is available in Section 3.5.3

The uncertainties of the exact position of the Bragg peak can come from different elements. First, the accuracy of the processing depends indeed on the quality of the imaging [37]. However, imaging systems have limitations in spatial and temporal resolution [8]. In addition, the pre treatment is a frozen image of the patient at a specific time and does not take into account possible anatomical changes before and during treatment.

An additional uncertainty comes from the lack of specific tools for proton therapy. For example, the uncertainty of movement can be taken into account by adding additional margins. The planned target volume increases the robustness of the treatment plan. However, the target volume margin calculation tool was originally designed for radiation therapy and is still used for proton therapy, despite the lack of consideration of uncertainty coming from the use of protons.

Analytical dose calculation algorithms have limitations in predicting range dose partially because they do not model proton scattering correctly [13]. These uncertainties are especially present with complex geometries. Monte Carlo algorithms handle complex geometries better. One additional uncertainty in Monte Carlo models comes from the implementation of physics settings, one of the most uncertain is the value of the mean exitation energy. This can add 1.5-2% uncertainty to the range [13]. Even the composition of the materials used may not be known accurately enough.

Another uncertainty that is best handled with Monte Carlo is the Hounsfield unit (HU) conversion. In analytical models the conversion to relative stopping power can cause large changes in the range if there is a small error. However, with Monte Carlo, it does not assign relative doses but density and composition of matter [13] and the uncertainties due to this conversion are smaller.

All these uncertainties have to be taken into account during the dose planning. Determining margins correctly is crucial. Margins underestimating in proton therapy may indeed result in an under-dosage of the tumor or over-dosage to normal tissue past or before the target. To be comfortable enough to reduce the volume of treatments, it is necessary to have a deep understanding of these uncertainties. Historically proton centers have adopted a range uncertainty planning margin of approximately 3.5% +1mm expansion along the beam direction [38].

Table 2 shows different sources of uncertainties in the proton range estimation. We can see that the uncertainties can be between 2.4%+1.2mm and 4.6%+1.2mm depending on the level of heterogeneity and Monte Carlo allows a decrease of the uncertainty.

Source of range uncertainty in the patient	Range uncertainty without Monte Carlo	Range uncertainty with Monte Carlo
Independent of dose calculation:		
Measurement uncertainty in water for commissioning	± 0.3 mm	± 0.3 mm
Compensator design	± 0.2 mm	± 0.2 mm
Beam reproducibility	± 0.2 mm	± 0.2 mm
Patient setup	± 0.7 mm	± 0.7 mm
Dose calculation:		
Biology (always positive) ^	+ ~0.8%	+ ~0.8%
CT imaging and calibration	± 0.5%	± 0.5%
CT conversion to tissue (excluding I-values)	± 0.5%	± 0.2%
CT grid size	± 0.3%	± 0.3%
Mean excitation energy (I-values) in tissues	± 1.5%	± 1.5%
Range degradation; complex inhomogeneities	0.7%	± 0.1 %
Range degradation; local lateral inhomogeneities *	± 2.5%	± 0.1 %
Total (excluding *, ^)	2.7% + 1.2 mm	2.4% + 1.2 mm
Total (excluding ^)	4.6% + 1.2 mm	2.4% + 1.2 mm

Table 2: *Estimated proton range uncertainties and their sources and the potential of Monte Carlo for reducing the uncertainty [13].*

2.5 FLASH Proton therapy

One of the most recent discovery in the field is FLASH proton therapy. It is based on the principle of FLASH radio therapy (FLASH-RT) using proton. FLASH consists in sending a dose rate of more than 40 Gy/s. It has been observed experimentally that a higher dose rate allows indeed an equal control of the tumor but with less harmful effects on both the short and long term on the surrounding tissues [22]. Most studies explore the effect with an electron beam. The difficulty with electron is to achieve a conformal dose distribution and treating deep seated tumors [39].

Several studies [23, 24, 26] have shown the potential of FLASH therapy. A study has been done on mini pigs and cats due to their similarities with the human body. The results in the pigs show that FLASH-RT minimize the normal tissue damage at the skin level even with high dose. In the cats, no late side effects were seen apart from depilation. This study has been performed with electrons due to the ease to create electron beams with high dose rate (such a beam can be produced from a few Gy/min to thousands of Gy/s) [24]. However theses studies show how this method is promising for the future.

The minimal dose rate for conventional proton therapy is 2 Gy/min for a single field to 1 liter volume. For the delivery at FLASH rate (delivered in 100 ms), the system must be capable of delivering an average current of 300nA at the patient (20 Gy/s). In the existing proton accelerator technologies, only the isochronous cyclotrons

are capable of delivering such a current [25]. For the moment, the number of protons delivered is governed by dose monitors. For the FLASH therapy, it will be important to add a security that acts quickly enough to stop the beam once the desired dose is attained and prevent the patient to be overdosed. It must be faster than the delivery time of one spot, faster than 100ms.

In the existing systems, there are different difficulties to reach this amount of energy and different ideas have to be put in place to counter these.

- The first challenge is the trajectory. Between the first and last moment when a certain point P receives a dose, it takes indeed a certain time. Accordingly, this time lapse adds uncertainties on the dose distribution. To decrease the time lapse, the idea is to optimize the trajectory.
- The second challenge results from the different energy levels. The energy switch time is 200 to 1000 microseconds which is relatively long compared with the total delivery time for FLASH therapy [39]. This shows that to attain the desired dose, it will be necessary to work with one layer of energy.
- The third challenge is the current (depending on the energy) coming out of the cyclotron. Indeed, we want it to be as high as possible. However, when passing through the system, there is a random loss of energy which requires a selection system to be put in place and therefore leads to a loss of protons. The efficiency can be less than 50%[25]. The transmission efficiency of the low energy protons beams becomes extremely low [39]. Therefore to achieve maximum efficiency, we take the energy directly from the cylcotron (at 226 MeV on IBA ProteusPLUS).

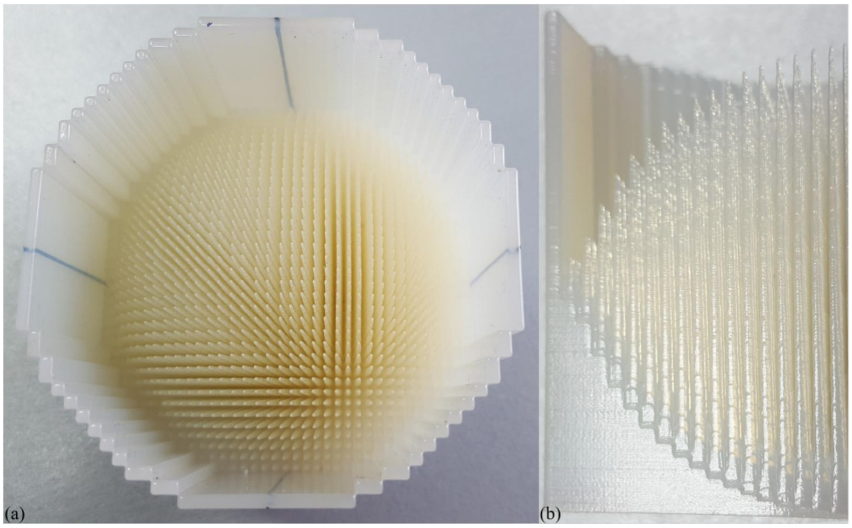

Figure 9: *Example of 3D spherical range modulator; top view (a) and a quarter of it, side view (b) [9].*

A specific 3D-printed range modulator (also called the hedgehog due to its specific shape) per patient is put between the patient and the nozzle (see Figure 9). This range modulator is a material with different thickness which is placed in the beam path and is a passive scatterer which will permits a 3D uniform dose distribution. The shape of the contour of the modulator gives the proximal shape of the tumor (see Figure 10). The distal shape of the target depends on the length of each individual spike [9].

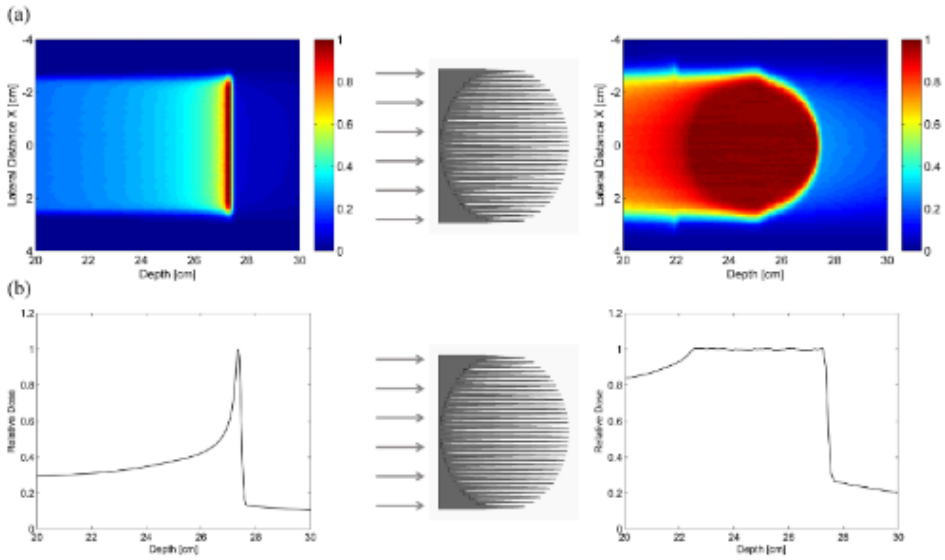

Figure 10: *Principle of the 3D range-modulator for a spherical tumor (d= 5 cm) placed at 25 cm depth in a water phantom. Monte Carlo simulated X-Z midplane profile (a) and center line depth dose distribution (b) [9].*

The discovery of the benefits of FLASH radiotherapy is recent and the understanding behind this phenomenon is still under research. It has been discovered that oxygenation plays an important role. A rapid high dose in normal cells consumes oxygen and prevents them from reoxygenating, thus helping to prevent ionization. However, since tumors contain a large number of vessels, the local consumption of oxygen caused by the FLASH beam has minor impact on tumor oxygenation. However, this does not explain everything. The immunological response and DNA damage is different with FLASH radio therapy and conventional radiotherapy [5]. The understanding behind these mechanisms will help to understand why FLASH radiotherapy is more beneficial.

3

Physics of proton

After explaining the basic concept of proton therapy, this section will look at the physical properties behind it. Different common terms like fluence, absorbed dose, Gray and pristine Bragg curve will be described. Then the behavior of the proton in matter will be broken down and explained. Finally, as the material used in this study is water, the concept of water equivalent thickness is central and therefore will be analyzed.

3.1 Fluence

Fluence describes the number of particles at a certain point in the beam.

$$\Phi = \frac{dN}{da} \qquad [\frac{protons}{cm^2}] \tag{3.1}$$

dN designates the number of particles passing through da and da is an infinitesimal element of area perpendicular to the beam.

3.2 Absorbed dose

The physical absorbed dose at a certain point is the energy deposited in matter per unit of mass. The unit of ionizing radiation dose is the Gray (Gy). It is defined as the absorption of one joule of radiation energy per kilogram in matter.

$$1 \quad Gy = 1 \quad \frac{J}{kg} \tag{3.2}$$

The fundamental formula [40] of absorbed dose (Equation 3.3) depends on the density of the material ρ , an infinitesimal volume of frontal area dA and a thickness dz exposed to dN monoenergetic protons.

$$D \equiv \frac{\text{energy}}{\text{mass}} = \frac{\frac{dE}{dz} \times dz \times dN}{\rho \times dA \times dz} = \left(\frac{dN}{dA}\right) \times \left(-\frac{1}{\rho}\frac{dT}{dz}\right) = \Phi \times \frac{S}{\rho} \tag{3.3}$$

$$\text{Absorbed} \quad \text{Dose} = \text{Fluence} \times \text{Mass} \quad \text{Stopping} \quad \text{Power}$$

If the material is a mixture of elements, the atoms act separately, and we can replace the mixture by a succession of thin layers of each constituent element. It leads to the Bragg additivity rule [13] :

$$\frac{S}{\rho} = \sum_i w_i \left(\frac{S}{\rho}\right)_i \tag{3.4}$$

where w_i is the fraction by weight of the ith element.

Now if the material is a compound, it is more complex. Their constituents are bound and do not act separately. However, the Bragg rule seems to hold quite well even then. [13]

3.3 Conversion of units

In this work the simulation results are expressed in Gy for the dose. However, the database for the energy loss are given in $\frac{MeV}{mm}$ and the fluence in $\frac{1}{mm^2}$. The conversion to Gy can be done using the following relations.

$$1MeV = 1.6022 \times 10^{-13} J \tag{3.5}$$

$$\rho_{water} \times 1mm^3 = 1\frac{kg}{m^3} \times 1mm^3 = 10^{-6} kg \tag{3.6}$$

$$\frac{MeV}{mm}\frac{1}{mm^2} = \frac{1.6022 \times 10^{-13} J}{10^{-6} kg} = Gy \tag{3.7}$$

The conversion from mm^3 to kg depend on the density of the matter. The above represents the conversion for water. However, if the material is different, so is the conversion.

3.4 Pristine Bragg curve

A pristine Bragg curve is a depth dose distribution in an absorber irradiated by a monoenergetic proton beam. A model proposed by Bortfeld [10] permits to calculate the Bragg curve for proton energies between 10 and 200 MeV:

$$D(z) = \phi_0 \frac{e^{-\zeta^2/4}\sigma^{1/p}\Gamma(1/p)}{\sqrt{2\pi}\rho p \alpha^{1/p}(1+\beta R_0)}\left[\frac{1}{\sigma}D_{-1/p}(-\zeta) + \left(\frac{\beta}{p} + \gamma\beta + \frac{\epsilon}{R_0}\right)D_{-1/p-1}(-\zeta)\right] \tag{3.8}$$

$D(z)$ is the depth dose, z the depth, ϕ_0 is the initial fluence and R_0 the range of the proton beam[6]. The standard deviation of the Gaussian distribution of the proton depth is represented by σ, $\zeta = (R_0 - z)/\sigma$, a is a material dependent constant and p is a constant that takes into account the dependence of the proton energy or velocity[7]. The mass density of the material is represented by ρ , ϵ is the fraction of low-energy proton fluence to total proton fluence, $\Gamma(x)$ is the gamma function and $D_y(x)$ is the parabolic cylinder function.

3.5 Behavior of protons in matter

Protons are charged particles. The transport of this type of particles is governed by three processes: stopping, Coulomb scattering and nuclear interaction. These processes come from three phenomena: Coulomb interactions with atomic electrons, Coulomb interactions with atomic nuclei and nuclear interaction with atomic nuclei. When leaving the nozzle, the behavior of the beam will be governed by these.

[6] For the definition of the range look at Section 3.5.2

[7] The values can be found by fitting with data of range or stopping power from measurements.

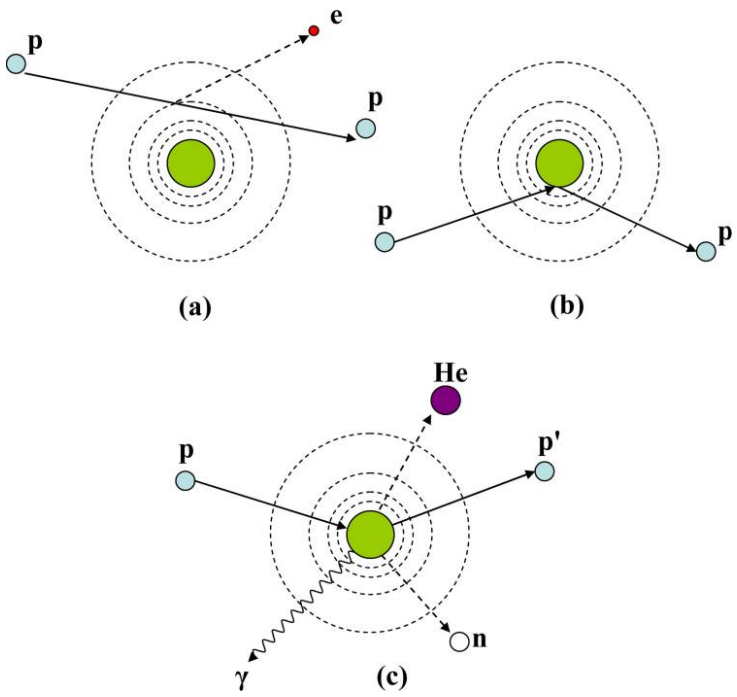

Figure 11: *Schematic illustration of proton interaction mechanisms: (a) energy loss via Coulombic interactions, (b) deflection of proton trajectory by repulsive Coulomb scattering with nucleus, (c) removal of primary proton and creation of secondary particles via non-elastic nuclear interaction. (p: proton, e: electron, n: neutron, He: Helium, : gamma rays) [10].*

3.5.1 Stopping

The stopping power is a quantity which describes the rate at which charged particles lose their energy. This is usually expressed in MeV/cm. Two types of stopping power can be found in literature: electronic and nuclear. Electronic stopping power refers to the slowing down of a projected ion due to the inelastic collisions between bound electrons in the medium and the ion moving through it. On the other hand, nuclear stopping power refers to the elastic collisions between the projected ion and nuclei in the sample [41]. The nuclear stopping power is non negligible only for heavy charged particles.

The loss of particle energy is mostly due to the so-called inelastic collisions (mainly with atomic electrons [8]). This collision is accompanied by a change in the internal state of the atom. It can go from a normal state to an excited state, which is called ionization of an atom [42]. It is this ionization that causes the loss of energy of the beam. Even if the energy transferred during a single collision does not affect the incident energy, the number of electrons in a material (and thus the number of collisions) is large enough to contribute to the energy loss.

For the notion of stopping, the Bethe-Bloch formula is central. It describes the average energy lost per depth in matter of a charged particle. Several corrections have been made to the initial formula for high energy particles and high atomic number targets (density and Shell corrections). However, as the energies and materials used for radiotherapy introduce only a minimal effect, these corrections have been neglected in the following analytical shape (the pertinent range for protons : 50-350 MeV) [43].

[8] Cross section $\sigma \cong 10^{-17} - 10^{-16} cm^2$.

$$-\frac{dE}{dx} = \frac{K\rho Z z^2}{2A\beta^2}(ln(\frac{2m_e c^2\beta^2\gamma^2 T_{max}}{I^2}) - \beta^2 - \frac{C}{Z}) \tag{3.9}$$

- $K = 4\pi N_A r_e^2 m_e c^2$ is a constant.
- N_A is the Avogadro number.
- m_e, r_e are the mass and classical radius of the electron respectively.
- ρ is the mass density of the material.
- Z is the effective atomic number of the absorber.
- A is the effective atomic mass of the absorber (ratio of atomic weight and total number of atom).
- z is the charge of the particle.
- β (= $\frac{v}{c}$, v is the velocity of the particle) and γ (= $\frac{1}{\sqrt{1-\beta**2}}$)are the relativistic parameters of the particle.
- I is the mean excitation potential[9] of the material. It depends on target materials and is found by fitting measured ranges or stopping powers and by interpolation if not available. It describes how easily a target can absorb kinetic energy from the projectile.
- C is the shell correction for low energy effects.
- T_{max} is the maximum kinetic energy that can be transferred to an electron/

$$T_{max} = \frac{2m_e c^2\beta^2\gamma^2}{1 + 2\gamma\frac{m_e}{M} + (\frac{m_e}{M})^2}$$

with M the mass of the particle.

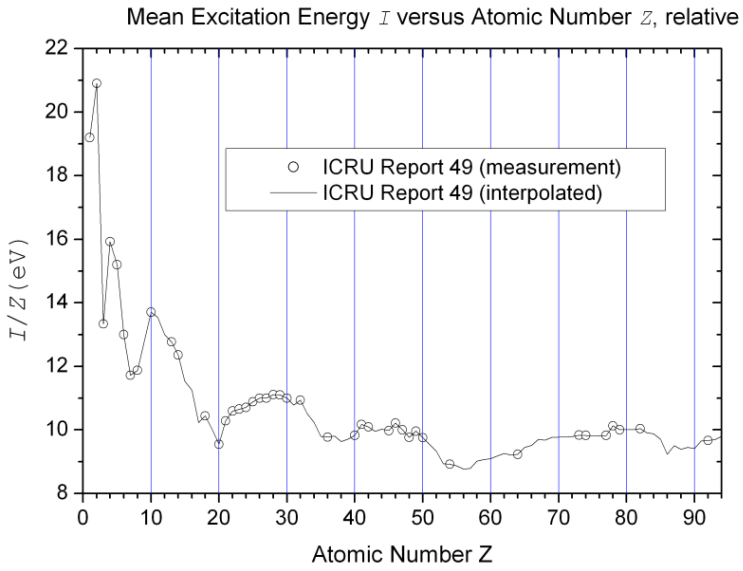

Figure 12: *Mean excitation energy normalized to the atomic number for elements as a function of atomic number [11].*

[9]The mean excitation potential is the amount of energy required to raise the energy level of an atom.

A fundamental limitation in the accuracy of proton range determination comes from the uncertainty in the estimated mean excitation energy. This uncertainty is in the order of 10-15% [44]. Even the determination of the I-value of liquid water is not a trivial task. There is no consensus in how to establish this value. One possible value depending on the atomic number Z can be seen in Figure 12.

The velocity of the particle, v, is computed depending on the energy of protons. An electron volt is an energy unit,1 eV = 1.602×1019 J. In this situation, it is used as a kinetic energy (K).

$$K = mc^2 \left(\frac{1}{\sqrt{1 - \frac{v^2}{c^2}}} - 1 \right) \tag{3.10}$$

The Formula 3.9 put forward that the energy loss depends on the inverse square of the particle velocity. This explains the shape of the Bragg curve and the peak just before the particle stops. It also shows that it depends on the mass density of the material. The range will change from one tissue to another.

3.5.2 Range

The range can be defined as the depth at which half of the protons has stopped. There exist two methods to compute the mean particle range: analytical or numerical. The numerical is simply by integrating over the energy loss [45, 10]:

$$R(E) = \int_0^E \frac{dE'}{dE'/dX} \tag{3.11}$$

where E is the ion's initial kinetic energy. This formula represents the continuously slowing down approximation.

The path of most proton (or other heavy particles) is nearly a straight line. However, this computation methodology neglects the lateral scattering because it relays on the assumption that the ions always travel in a straight line.

By convention, the range is defined as the depth of the distal 80% point of the Bragg peak. However, the range of a proton beam is not absolute. It is because the slowing down of matters does not occurs in a smooth and continuous manner and the energy loss due to ionization involves random energy transfers. Range straggling is the phenomenon in which protons with the same energies at the start and at the end do not have the same path length [46]. A consequence of this straggling is a smearing out of the penetration [40]. Additional range error can come from errors during the conversion of Hounsfield number into stopping powers. An uncertainty in the proton range must be added when making a model.

3.5.3 Scattering

The inelastic collisions cause the loss of energy of the particles. Another type of collision will take place and are called elastic collisions. This one keeps the kinetic energy but are the main cause for deflection. The scattering is the principle that a particle is deviated from its straight trajectory.

A proton passing near a nucleus will indeed be elastically scattered or deflected by a repulsive force coming from the positive charge of the atom [10]. On the other hand, when protons pass near an electron, their trajectories remain an almost straight line because the atomic mass of a proton is 1832 times greater than that of an electron. This scattering affects both the proton and the electron therapy, but the degree of scattering is significantly inferior with proton (see Figure 13). Indeed, the electron/electron collision induce a large-angle multiple scattering of the electron beam.

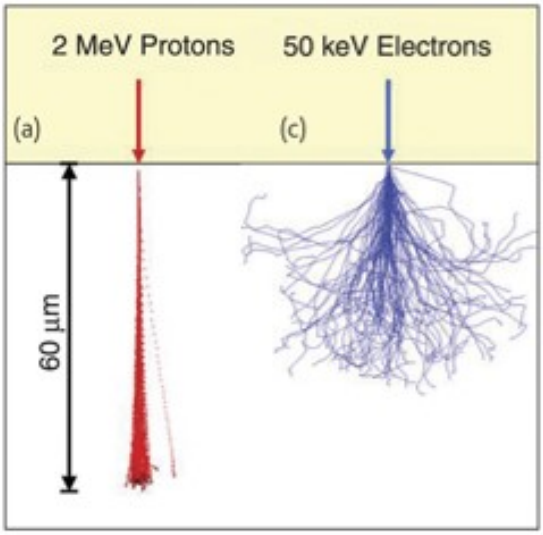

Figure 13: *Comparison between (a) protons and (c) electrons penetration in the matter [12].*

For single scattering, Rutherford scattering theory applies. However, in the case of proton therapy most of the materials passed through are sufficiently thick to consider that the number of scattering events is high enough to focus on the multiple Coulomb scattering. The multiple scattering permits to create uniform dose distribution. The statistical output of these many collisions is a multiple scattering angle which is nearly a Gaussian distribution with a certain standard deviation σ [30].

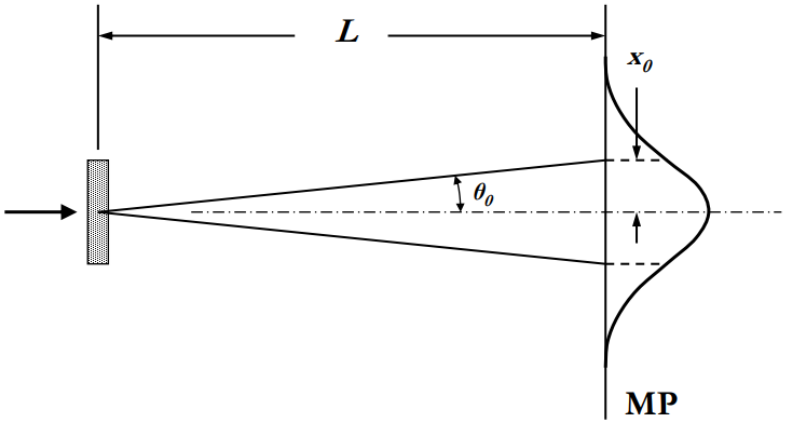

Figure 14: *Schematic representation of a multiple scattering in a thin slab [13].*

The procedure to find the value of the angular distribution, θ_0, is well represented by the theory of Molière (see Figure 14). Since the Molière theory is overly complex, the literature tried to develop a simpler formula. Highland has proposed a formula of the angle allowing to avoid the theory of Molière. It is often used to replace the Molière theory in the Gaussian approximation [47].

$$\theta_0 = \frac{14.1\ \text{MeV}}{pv} z\sqrt{\frac{L}{L_R}}\left(1+\frac{1}{9}log_{10}\left(\frac{L}{L_R}\right)\right) \qquad rad \tag{3.12}$$

Where p is the momentum and v is the speed. The only representation of the scattering material is L_R, the radiation length. However, this formula is exclusively for thin target. For a moderaly thick material, it is sufficient to replace pv with $p_1 v_1 p_2 v_2$ where 1 and 2 represent the incoming and outgoing protons. But for very thick targets, it is necessary to integrate over it [47].

$$\theta_0 = 14.1z(1+\frac{1}{9}\log_{10}(\frac{L}{L_R}))\times\left(\int_0^t\left(\frac{1}{pv}\right)^2\frac{dt'}{\rho X_0}\right)^{\frac{1}{2}} \qquad rad \tag{3.13}$$

3.5.4 Nuclear interaction

The last interaction mechanism is much less frequent and is a hard scattering. This phenomenon occurs because protons may interact with the atomic nucleus via non-elastic nuclear reactions in which the nucleus is irreversibly transformed [10]. To enter the nucleus, protons need to have sufficient energy to overcome the Coulomb barrier of the nucleus, which depend on its atomic number. The main effect of nuclear reactions in a therapeutic region of a proton field is a small decrease in absorbed dose due to the removal of primary protons. This decrease is compensated to a large extent by the liberation of secondary protons[10] and other ions. The probability for a proton to undergo a nuclear interaction increases as a function of the energy [11].

The reactions may be elastic or inelastic. Elastic reaction leaves the protons intact but loses a significant part of its energy and is deflected of few degrees. On the other hand, inelastic reaction can produce energetic protons, deuterons, tritons, 3^H, 4^H and other ions [30]. The secondary protons account for up to 10% of the absorbed dose in a high energy proton beam. They have a small but not negligible impact on the spatial dose distribution in a patient [10].

More specifically, water is composed of hydrogen and oxygen. The hard scattering on free hydrogen is elastic. The secondary proton created from the hydrogen emerges 90 degree apart [13] and the kinetic energy in the system is preserved and shared between the protons. The main effect of the nuclear is to reduce the number of primary protons.

3.6 Water-equivalent thickness(WET)

The body is composed of more than 70% of water and the human tissues is close to the properties of water. For this reason, the study of proton beams is mainly performed in water. To look at other materials, the water-

[10] The primaries are particles that escape the hard scatter and secondaries the others.
[11] Probability of 20 - 35% for protons of 200MeV - 250MeV.

equivalent thickness permits to translate any materials into a water thickness. To limit the additional range uncertainties the water-equivalent thickness must be the most accurate possible.

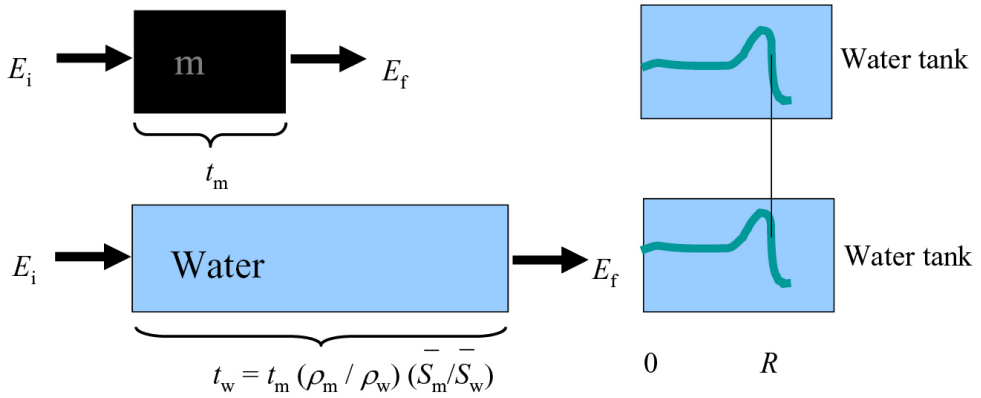

Figure 15: *Schematic illustration of the water equivalent thickness concept [10].*

The estimation of water equivalence thickness needs to take into account the interdependence between the radiation interaction cross section, the energy and the atomic composition.

$$WET = \frac{d_{80,water}}{d_{80,material}} \tag{3.14}$$

The WET depends on $d_{80,water}$, the range of the proton in water, and $d_{80,material}$, the range in the phantom material.

The equivalent thickness in water can be approximated by Equation 3.15 [10] which depend on t_m, the thickness of the material, and c_m, the depth scaling factor. This factor is equal to the ratio of the approximated range, $c_m = \frac{\rho_w R_w}{\rho_m R_m}$.

$$t_w = t_m \frac{\rho_m}{\rho_w} c_m \tag{3.15}$$

For thin target, the general equation for WET [48] gives:

$$t_w = t_m \frac{\rho_m \bar{S_m}}{\rho_w \bar{S_w}} \tag{3.16}$$

where $\bar{S}$ are the mean proton mass stopping power :

$$\bar{S} = \frac{\int_E S dE}{\int_E dE} \tag{3.17}$$

R. Bagheri's study [14] shows WET for different materials at different energies as shown in Figure 17. The WET values for these materials were found using the MCNPX[12] code and PSTAR program (NIST data). These results permit to estimate the equivalent thickness of water to produce the same Bragg peak (same intensity at the same depth) as with the material. For example, the equivalence for a 225 MeV proton beam that crosses 1 cm of PMMA plastic is a proton beam that crosses 1.16 cm of water. Both will deposit the most energy at the same depth.

[12] Monte-Carlo N-Particle transport.

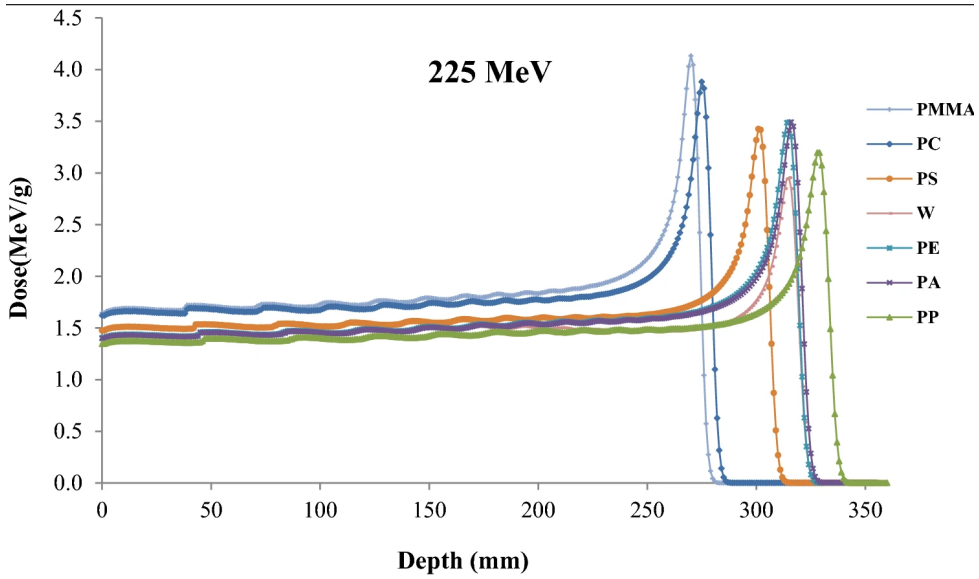

Figure 16: *Depth dose profiles of the studied materials for 225MeV proton energy as a function of depth [14]. The different materials are Polypropylene (PP), Polycarbonate (PC), Polystyrene (PS), water (W), Polyethylene (PE), Paraffin (PA) and Polypropylene (PP).*

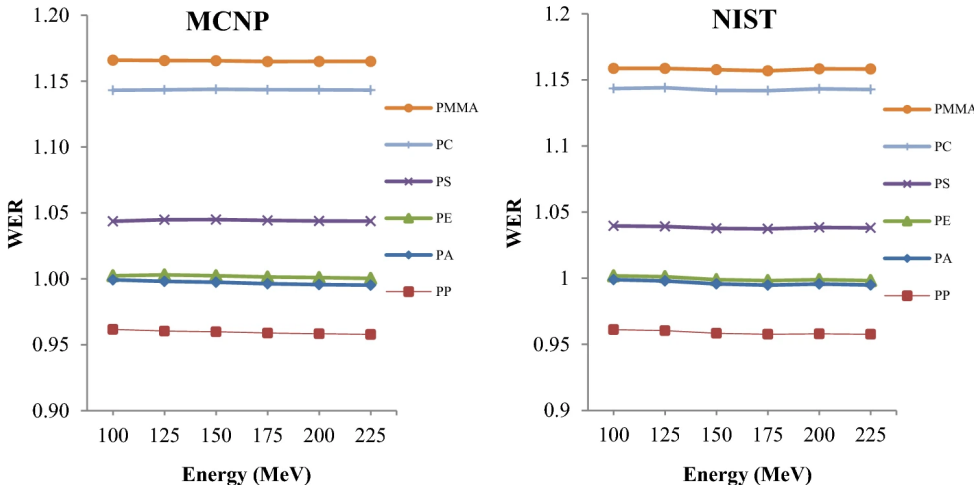

Figure 17: *WER values for different proton energies in the studied materials [14]. The results on the left was performed using the Monte Carlo simulation code (MCNPX) and the results on the right come from National Institute of Standards and Technology (NIST). The different materials are Polypropylene (PP), Polycarbonate (PC), Polystyrene (PS), water (W), Polyethylene (PE), Paraffin (PA) and Polypropylene (PP).*

4

Proton beam transport

So far we looked into the mechanism of radiotherapy and more precisely proton therapy with the physical principles behind it. In this chapter we will start from the physics of protons to describe the behavorial model of the proton beam transport.

The aim of this thesis is to study and model the passage of protons and their energy transfer in the hedgehog and in the medium placed after. The model that we seek to develop must allow us to:

- take into account any type of initial fluence (Uniform, Gaussian or arbitrary),
- isolate the contribution of each pixel of the elevation map representing a hedgehog in an acceptable computation time.

We will develop a mathematical model based on the elements of proton physics presented in the previous chapter. During the realization of the model, several assumptions were made:

- we consider only air and water,
- we work in an isotropic voxelized geometry,
- the hedgehog is voxelized.

The main element governing the simulation is the fluence which is governed by the Equation 4.1. It is simulated step by step. The fluence F at position (x, y, z) is dependent of a Gaussian filter function $G(x, y, E + \Delta E)$, a binary matrix M equal to one at the emplacement of the water and $\neg M$ the opposite, on the energy at depth z,E, and on the energy lost between $z-1$ and z,ΔE.

$$F(x, y, z, E) = (F(x, y, z-1, E + \Delta E)M(x, y, z)) * G(x, y, E + \Delta E) + F(x, y, z-1, E)\neg M(x, y, z) \tag{4.1}$$

The results of those simulations are obtained inside a rectangular grid. The size of the grid will depend on the initial energy. A number representing the fluence is saved in each of these voxels.

4.1 Transport of a mono energetic beam

In this first case the beam is mono energetic and all protons at depth z have the same energy.

The physical transport of a proton in matter is not a deterministic phenomenon, several protons sent from the same initial point will not go through the same path and will not necessarily end up in the same spot. Protons have a non-zero probability of moving to the right and to the left and not straight which results in extending the beam (see Section 3.5.3: Scattering). Since the original beam has an elliptical Gaussian distribution, convolving it with another Gaussian will have the desired effect [49]. Indeed, we will show that the

convolution of a Gaussian with another one is equal to a Gaussian with the sum of the σ. MCsquare's results of the lateral dose in Figure 18 support this idea. We observe that the initial Gaussian beam maintains a Gaussian fluence over the depths in a homogeneous phantom but with an evolving standard deviation. We will model this evolution mathematically.

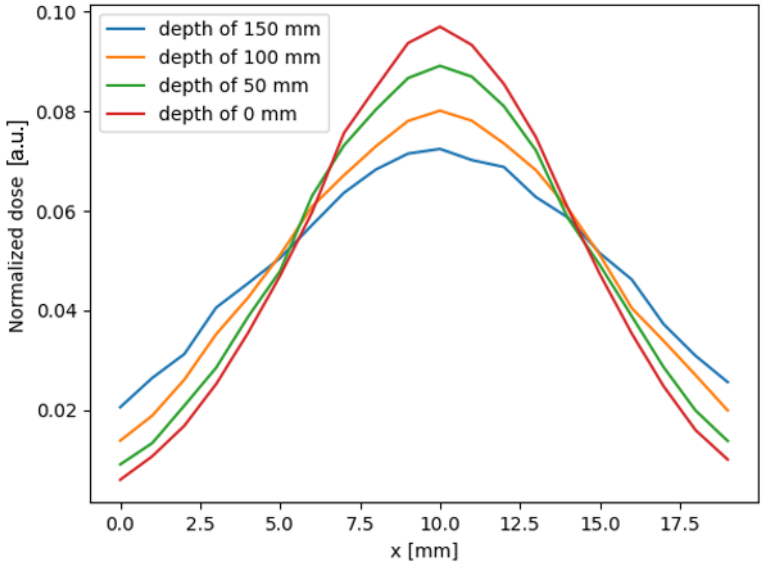

Figure 18: *Normalized dose at different depth found with MCsquare.*

$F(x,y)$ represents the shape of the initial beam and $G(x,y)$ a 2-dimensional Gaussian filter with a standard deviation of value σ_{fltr}. The variance of the Gaussian filter is determined according to the depth of water crossed. The standards deviations are supposed to be the same for x and y in the filter and the center of the nozzle is at (0,0).

$$F(x,y) := \frac{1}{2\pi\sigma_{x_0}\sigma_{y_0}} exp\left(-\frac{(x-x_0)^2}{2\sigma_{x_0}^2} - \frac{(y-y_0)^2}{2\sigma_{y_0}^2}\right) \tag{4.2}$$

$$G(x,y,z) := \frac{1}{2\pi\sigma_{fltr}^2} exp\left(-\frac{x^2+y^2}{2\sigma_{fltr}^2}\right) \tag{4.3}$$

The 2-D isotropic Gaussians are separable into x and y components. Thus the 2-D convolution can be performed by first convolving with a 1-D Gaussian in the x direction, and then convolving with another 1-D Gaussian in the y direction.

$$F_{z+1} = (F_z * G)(x,y) \tag{4.4}$$

$$= \int_{\tau_1=-\infty}^{\infty}\int_{\tau_2=-\infty}^{\infty} \frac{1}{2\pi\sigma_{x,z}\sigma_{y,z}} exp\left(-\frac{(x-\tau_1)^2}{2\sigma_{x,z}^2} - \frac{(y-\tau_2)^2}{2\sigma_{y,z}^2}\right) \frac{1}{2\pi\sigma_{fltr,z}^2} exp\left(-\frac{\tau_1^2+\tau_2^2}{2\sigma_{fltr,z}^2}\right) d\tau_1 d\tau_2 \tag{4.5}$$

The two integrals can be developed separately because there is no term depending on τ_1 and τ_2. We pose that $\sigma_{x,z+1} = \sqrt{\sigma_{x,z}^2 + \sigma_{fltr,z}^2}$.

$$F_{x,z+1} = \int_{-\infty}^{\infty} \frac{1}{2\pi\sigma_{x,z}\sigma_{fltr,z}} exp\left(-\frac{(x-\tau_1)^2}{2\sigma_{x,z}^2} - \frac{\tau_1^2}{2\sigma_{fltr,z}^2}\right) d\tau_1 \tag{4.6}$$

$$= \int_{-\infty}^{\infty} \frac{1}{2\pi\sigma_{x,z}\sigma_{fltr,z}} exp\left(-\frac{\sigma_{x,z}^2(x-\tau_1)^2 + \sigma_{fltr,z}^2\tau_1^2}{2\sigma_{x,z}^2\sigma_{fltr,z}^2}\right) d\tau_1 \tag{4.7}$$

$$= \int_{-\infty}^{\infty} \frac{1}{2\pi\sigma_{x,z}\sigma_{fltr,z}} exp\left(-\frac{\sigma_{x,z}^2x^2 - 2\sigma_{x,z}^2x\tau_1 + (\sigma_{x,z}^2 + \sigma_{fltr,z}^2)\tau_1^2}{2\sigma_{x,z}^2\sigma_{fltr,z}^2}\right) d\tau_1 \tag{4.8}$$

$$= ...$$

$$= \frac{1}{\sqrt{2\pi}\sigma_{x,z+1}} exp\left(-\frac{x^2}{2\sigma_{x,z+1}^2}\right) \int_{-\infty}^{\infty} \frac{1}{\sqrt{2\pi}\frac{\sigma_{x,z}\sigma_{fltr,z}}{\sigma_{x,z+1}}} exp\left(-\frac{(\tau_1 - \frac{\sigma_{x,z}^2x}{\sigma_{x,z+1}^2})^2}{2(\frac{\sigma_{x,z}\sigma_{fltr,z}}{\sigma_{x,z+1}})^2}\right) d\tau_1 \tag{4.9}$$

In the last equation, the integral is an integral of a normal density distribution on τ_1 which is evaluated to 1. The same reasoning can be performed for y and the multiplication of the two results confirms that the convolution of two 2-dimensional Gaussian creates another 2-dimensional Gaussian that is more spread out.

After N steps (N convolutions), the variance for x (and for y) of the Gaussian distribution is given by equation 4.10.

$$\sigma_{x,z=N}^2 = \sum_{i=0}^{N} \sigma_{x,z=i}^2 \tag{4.10}$$

The convolution translates well the idea that the more the beam passes through matter the more it expands.

4.2 Transport of a multi energetic beam

After explaining mathematically the mono energetic transport of the beam, we will focus on the multi energetic beam. This type of beam is the one we will work with for the FLASH proton therapy. When a beam encounters an obstacle, it will create different levels of energy and become multi energetic. As explained in Section 3.5, the interaction of protons with other particles will cause a multiple scattering which will stretch the beam. This phenomenon only occurs in the obstacle or in the water phantom since the multiple scattering is a phenomenon caused by interaction of proton with other particles. First we look at the mathematical effect of the obstacle on the beam. In a second step, we show how this type of beam is integrated in our model.

4.2.1 Mathematical effect of the obstacle

When the beam encounters an obstacle with a rectangular shape, only a certain part of the beam will undergo convolution. Mathematically, the function that will be convolved is

$$F_z^{'} = \begin{cases} F_z & \text{if } X_{start} \leq x \leq X_{end} \text{ and } Y_{start} \leq y \leq Y_{end} \\ 0 & \text{Otherwise} \end{cases} \tag{4.11}$$

where X_{start}, X_{end}, Y_{start} and Y_{end} represent the coordinates of the water tank vertices. Similarly to what we did above we compute the convolution in x and y separately. The effect of this new function on the

convolution can be seen on the last equation below.

$$F'_{x,z+1} = \int_{-\infty}^{\infty} F'_{x,z}(\tau_1) G_x(x-\tau_1) d\tau_1 \tag{4.12}$$

$$= \int_{x_{min}}^{x_{max}} F_{x,z}(\tau_1) G_x(x-\tau_1) d\tau_1 \tag{4.13}$$

$$= ...$$

$$= \frac{1}{\sqrt{2\pi}\sigma^2_{x,z+1}} exp(-\frac{x^2}{2\sigma^2_{x,z+1}}) \int_{x_{min}}^{x_{max}} \frac{1}{\sqrt{2\pi}\frac{\sigma_{x,z}\sigma_{fltr,z}}{\sigma_{x,z+1}}} exp\left(-\frac{(\tau_1 - \frac{\sigma^2_{x,z}x}{\sigma_{x,z+1}})^2}{2(\frac{\sigma_{x,z}\sigma_{fltr,z}}{\sigma_{x,z+1}})^2}\right) d\tau_1 \tag{4.14}$$

The last integration is not equal to 1 anymore. The fluence at the next step will depend on the size of the obstacle , on $\frac{\sigma^2_{x,z}x}{\sigma_{x,z+1}}$ and on the value of $\frac{\sigma_{x,z}\sigma_{fltr,z}}{\sigma_{x,z+1}}$. The last two relations represent indeed the mean and standard deviation, respectively. The value of the integral (the fluence between two points of the integral) can be found using Equations 4.15 and 4.17. Equation 4.15 gives the value of the integral between the points $\mu + n\sigma$ and $\mu - n\sigma$ and Equation 4.17 is the error function [15]. Figure 19 shows the value of the integral depending on the standard deviation.

$$F(\mu + n\sigma) - F(\mu - n\sigma) = \text{erf}\left(\frac{n}{\sqrt{2}}\right) \tag{4.15}$$

$$F(x) = \frac{1}{2}\left(1 + \text{erf}\left(\frac{x-\mu}{\sigma\sqrt{2}}\right)\right) \tag{4.16}$$

$$\text{erf}(x) = \frac{2}{\sqrt{\pi}} \int_0^x e^{-x^2} dt \tag{4.17}$$

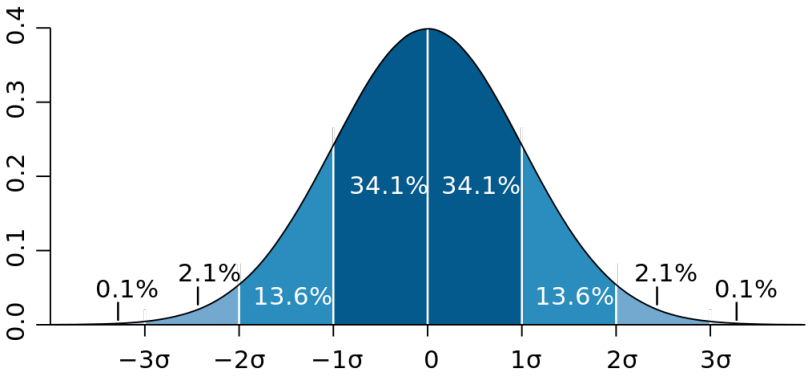

Figure 19: *Standard deviation diagram [15].*

Unfortunately, the last integral depends on x, so the multiple convolutions cannot be easily simplified. The 1-D fluence of the part that crossed N mm of the tetrahedron (which went through N convolutions) is given by

$$\mathcal{N}\left(0,\sum_{i=0}^{N}\sigma_i^2\right)\times\int_{x_{min}^N}^{x_{max}^N}\frac{1}{\sqrt{2\pi}\frac{\sigma_{x,N-1}\sigma_{fltr,N-1}}{\sigma_{x,N}}}exp\left(-\frac{(\tau_1-\frac{\sigma_{x,N-1}^2 x}{\sigma_{x,N}})^2}{2(\frac{\sigma_{x,N-1}\sigma_{fltr,N-1}}{\sigma_{x,N}})^2}\right)...$$
$$\times\int_{x_{min}^1}^{x_{max}^1}\frac{1}{\sqrt{2\pi}\frac{\sigma_{x,0}\sigma_{fltr,0}}{\sigma_{x,1}}}exp\left(-\frac{(\tau_1-\frac{\sigma_{x,0}^2 tau_2}{\sigma_{x,1}})^2}{2(\frac{\sigma_{x,0}\sigma_{fltr,0}}{\sigma_{x,1}})^2}\right)d\tau_1...d\tau_N \tag{4.18}$$

When the beam gets out of the tetrahedron, it has several layers of fluence of different energies. In the patient every layer changes at each step and has to be taken into account in the computation of the dose. The obstacle allows to spread the beam and create different levels of energy which will generate a spread-out Bragg peak and helps to create a uniform dose at the tumor.

However, we will see that with a high initial energy equal to 226 MeV, the scattering is lower at the beginning thus in the obstacle. A second simplified scenario could be to ignore the convolution in the obstacle and simplify the integrals. To further simplify, the final block of water is supposed to be large enough to have a unitary integral. Finally, the main effect of the obstacle is not to stretch the beam but to create a multi energetic fluence (see the left part of Figure 21).

4.2.2 Modelling the encounter of a beam and an obstacle

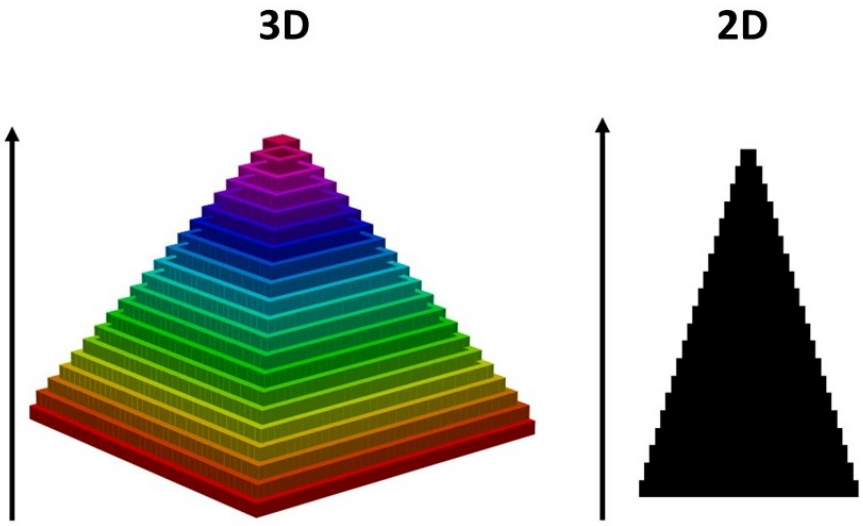

Figure 20: *3-D (on the left) and 2-D (on the right) representation of a pyramidal tower with a squared basis. The arrow represents the proton beam direction.*

The equations explained above shows that it is necessary to perform the fluence step by step to find the fluence at a certain point. The classical type of obstacle that will be studied in this thesis has a pyramidal shape with a squared basis (see Figure 20).

$$F(x,y,z,E) = (F(x,y,z-1,E+\Delta E)M(x,y,z)) * G(x,y,E+\Delta E) + F(x,y,z-1,E)\neg M(x,y,z) \tag{4.19}$$

Equation 4.19 is the relation used in our model. It exhibits that the fluence at a depth z depend on the fluence at depth $z-1$. The right part of Figure 21 shows the created level of energy. For example, at $z=3$, there are levels of energy and the fluence of protons with an energy E3 is found with the fluence of protons with energy E2 at $z=2$ which passes through the obstacle at $z=3$.

An additional element to consider is that the spread of the fluence will also depend on the energy. The scattering will indeed not be the same for protons at 100 MeV and the ones near 0 MeV. For that reason, G also depends on the energy. Protons at the same position z will spread differently depending on their energy.

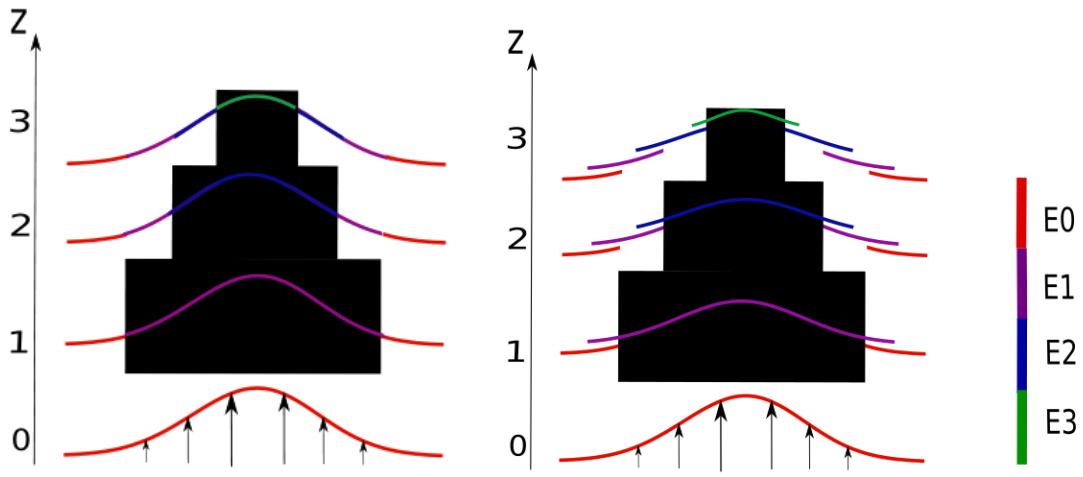

Figure 21: *Representation of the energy levels created by the pyramidal tower with convolution (on the right) and without (on the left). E0,E1,E2 and E3 are decreasing energies and the initial fluence is Gaussian.*

Now if we look at the evolution of the beam in the obstacle by posing the second scenario with the simplification, the iterative equation 4.19 in the obstacle becomes:

$$F(x,y,z,E) = (F(x,y,z-1,E+\Delta E)M(x,y,z)) + F(x,y,z-1,E)\neg M(x,y,z) \tag{4.20}$$

while the fluence after the obstacle remains governed by Equation 4.19.

Once the fluence is known, the total absorbed dose can be computed and is equal to the sum of the absorbed dose for all energies.

$$Dose(x,y,z) = \sum_{i=E0}^{E} F(x,y,z,i) \cdot Energy\_loss(i) \cdot K \qquad [Gy]$$

K is the conversion constant from $[MeV/mm^2]$ to $[Gy]$.

5

Material and methods

We have so far laid all the foundations necessary to understand and realize our model. In this chapter we will introduce the physical components simulated and the characteristic and choice made. Then, the Monte Carlo method and ,more precisely, MCsquare is introduced because it will be used for the validation of our model results.

5.1 Geometry of the environment

All simulations are performed in a globally similar environment. First of all, the space is divided into spots. The distance between each spot is 1 mm. The configuration of the environment is always similar to Figure 22 with different distance $D1$, $D2$ and $D3$ depending on the mean initial energy, the depth and volume of the target. The depth in water presented in the figures begins at the beginning of C.

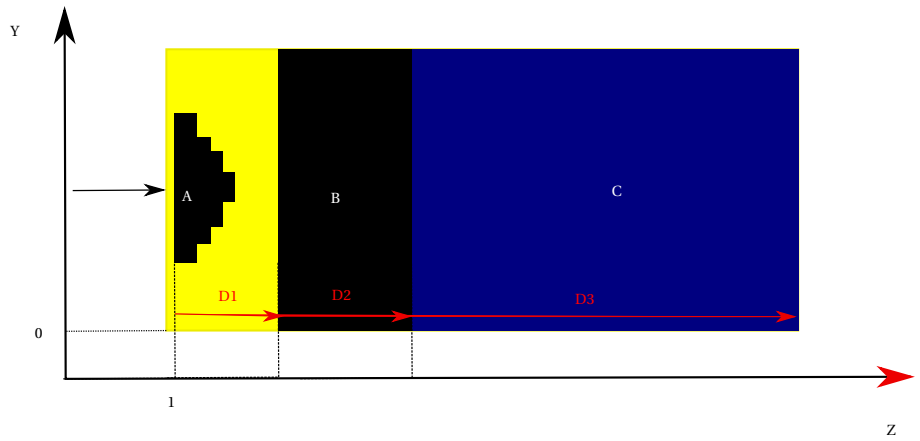

Figure 22: *Schematic representation of the simulated geometry. A is the range modulator, B, the range shifter and C, the water phantom. D1,D2 and D3 are transmitted in mm.*

The only present material is water. If any other material is used, it will be expressed as a water equivalent length. The space between the different compartment is air and we assume that it acts like the void. It is presented in yellow in Figure 22.

These assumptions decrease the accuracy but increase the computation time. Every choice made is to find a balance between accuracy and computation time.

5.2 Beam characteristics

At the exit of the cyclotron, the protons beam is mono energetic and has an elliptical shape around a central axis [50]. For the purpose of our study, we have assumed that the beam is a circular Gaussian. The direction of

the beam is along the z-axis. The beam characteristic at the entrance are the spot size, angular spread, mean energy, and energy spread [51].

The spot size and angular spread are each described by a single Gaussian standard deviation. A smaller standard deviation is desirable since it allows a sharper penumbra and a greater control over the dose distributions. For the highest energy (220 to 250 MeV) it ranges from 3 to 5mm. [52] The Gaussian distribution beam used for the purpose of this study has a standard deviation of $3mm$.

The mean energy and the energy spread are the energy parameters. The energy spread is also described by a Gaussian standard deviation. The mean energy can vary between 100 and 226 MeV. For FLASH therapy only the highest mean energy of the cyclotron will be used for analysis.

5.2.1 Multiple scattering angles

As explained before, we model the lateral scattering by a convolution sequence $(F(z) * G(z, \sigma_{filter}))$. The σ_{filter} is determined by MCsquare.

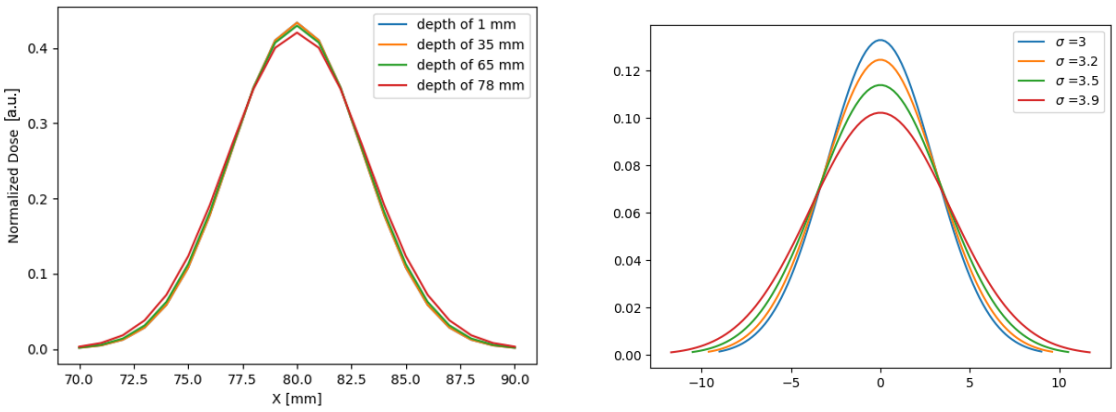

Figure 23: *Normalized dose at different depth found with MCsquare (on the left) and Gaussian distribution with different variance (on the right).*

In order to find the values of these σ, we look at the Normal formed in each z for a certain y (or x, because we are working in a symmetric beam). Then we compare with a list of Gaussian curves with known standards deviation to find the σ at each z. We take the standard deviation of the generic Gaussian which fits best the dose using the mean squared error measure. Then the relation found in Section 4 helps us to find the value that will be used in the convolutions:

$$\sigma_{filter,z} = \sqrt{\sigma_{z-1}^2 - \sigma_z^2} \tag{5.1}$$

Since we know the standard deviation of the initial fluence, we can find all the other σ values. The Gaussian values depend here on the depth because we are in the scenario of a mono energy beam. However, once we are in a multi energy beam, it is important to note that the scattering will be energy dependent. A proton close to zero energy will indeed have a different probability to scatter than a proton of full energy.

Finally, these scattering angles for each initial energy are saved in a file and ready to be used when necessary.

5.2.2 Range straggling

Due to range straggling not all protons of the same energy have the same range. The effect of this straggling is a more spread Bragg peak experimentally than simulated.

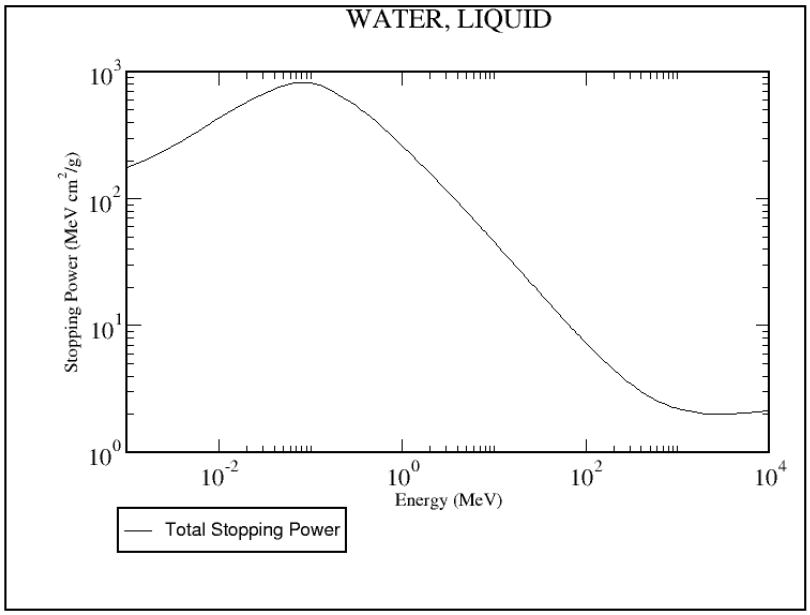

Figure 24: *Total Stopping Power from PSTAR[16].*

As explained above, when the proton beam moves, it loses energy. The energy loss could be found in databases like PSTAR (see Figure 24). In these databases, the stopping power for the high energies is found using the Bethe's formula with shell, Barkas and Bloch corrections and the density effect correction. For the low energies they calculated the stopping power from fitting formulas that represent experimental data [16]. Nevertheless, the energies for proton therapy is between 70 and 250 MeV[52].

Theoretically, the energy loss at each z is calculated only in function of the remaining energy.

$$\text{Energy}_{z+1} = \text{Energy}_z - \text{Energy\_loss}(\text{Energy}_z) \tag{5.2}$$

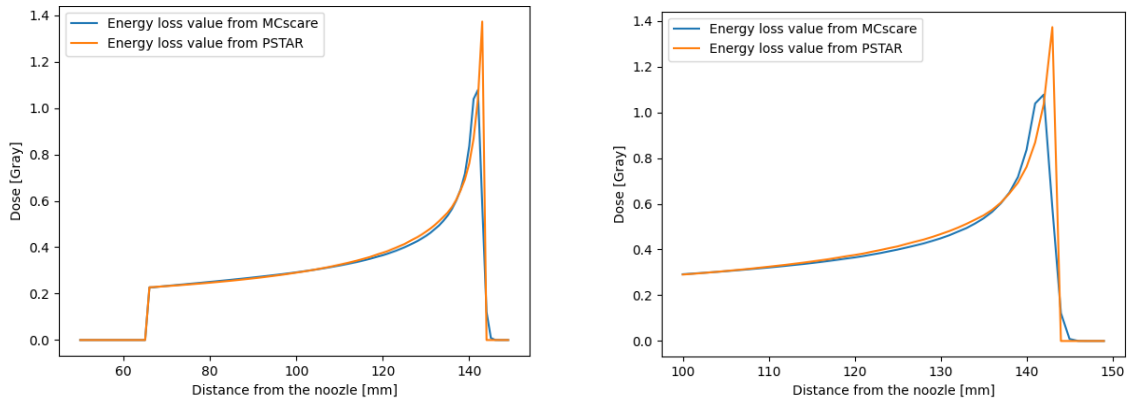

Figure 25: *Bragg peak of 100 MeV beam with Gaussian fluence distribution performed with our model using energy loss values from MCsquare and PSTAR. A zoom on the Bragg peak can be seen on the left.*

However, in reality the Bragg peak is less sharp. It can be explained by the trajectory of the protons which are not always straight (see Figure 26). This results in a shorter beam range for some protons than the theoretical one. Indeed, the data from PSTAR do not take into account the straggling and all the protons stop at exactly the same depth. Another reason is that in practice the beam is never totally mono energetic. Finally, to get closer to reality the energy loss used in the model is calculated from MCsquare (see Figure 25).

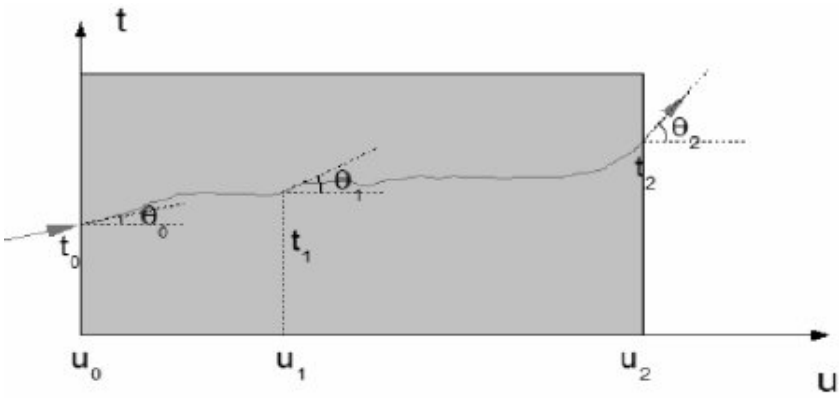

Figure 26: *Geometry of the path of a proton through an object in the t - u -plane [17].*

5.3 Range shifter

The range shifter is a passive beam modifier (often a slice of plastic) [21]. It is placed as close as possible to the patient to minimize the scattering. The proton beam pencil is broadened by the range shifter and the broadened is reduce by moving close to the patient. To spare the tissues as much as possible, the penumbra must be as sharp as possible [45].

Generally, it is used because the proton beam have a minimum energy and the range could be too high [53]. Especially since in FLASH therapy, the energy must be as high as possible. The range shifter permits to play easily with the range without adding a waiting time like with an active beam modifier.

The depth (see D2 in Figure 22) depends on the location of the target and on the shape of the range modulator.

5.4 Range modulator

The beam at the exit of the nozzle has a Gaussian shape. The width of which is only of few millimeters. To match a certain target volume, it has to be spread out in 3D. The shape and volume of most tumors are different and more spread than the one of an unmodified beam.

The range modulator is also a passive scattering. To reach the performances of the FLASH proton therapy it is indeed necessary to use only passive scattering. The shape and other characteristics of this 3-D range modulator will determine the shape of the spread-out Bragg peak. It is modelled with water, but it can be transformed into a 3D printing plastic material with a water-equivalent width. The range modulator is the only element that will modify the beam to produce a multi energetic beam and the desired uniform dose shape.

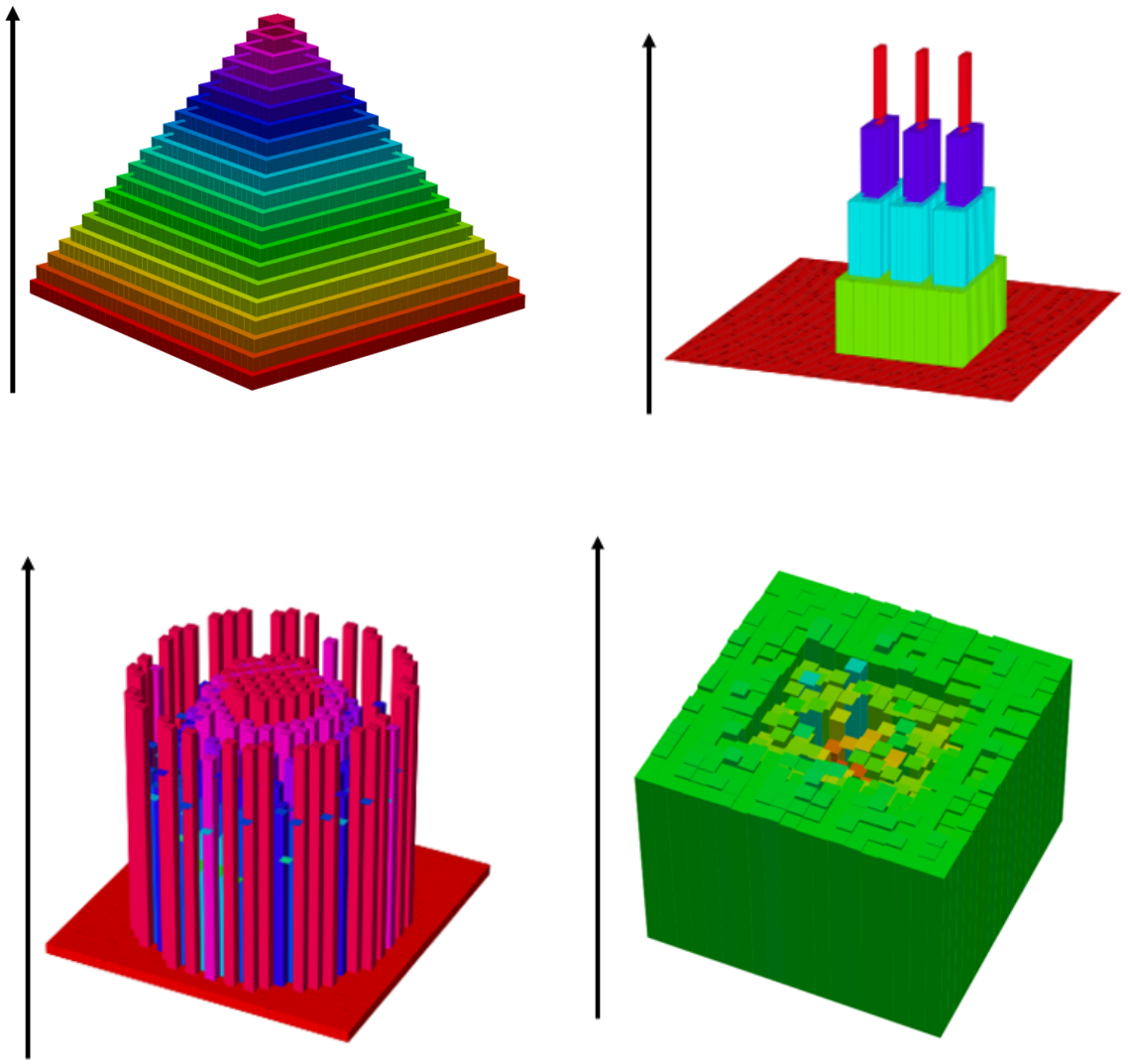

Figure 27: *Examples of possible range modulator.*

In this paper the modulator is represented as a binary matrix since it is only made of water. If other types of material were added it would be necessary to put another number representing it and specify in what type of

material we are.

Different types of range modulator will be used and compared (see Figure 27). The goal is to end up with a device that will give a dose conform to the tumor. With the precision of 1 mm the types of range modulator are limited.

A study of Simeonov [9] has already looked at 3D range-modulators. They studied the effect of a spherical 3D range-modulator with spikes of different heights next to each others to add degree of freedom (see Figure 28). Figure 10 shows that the shape of the modulator corresponds to the proximal contour of the tumor and the distal shape depends on the specific amount of homogeneous material of each spike [9].

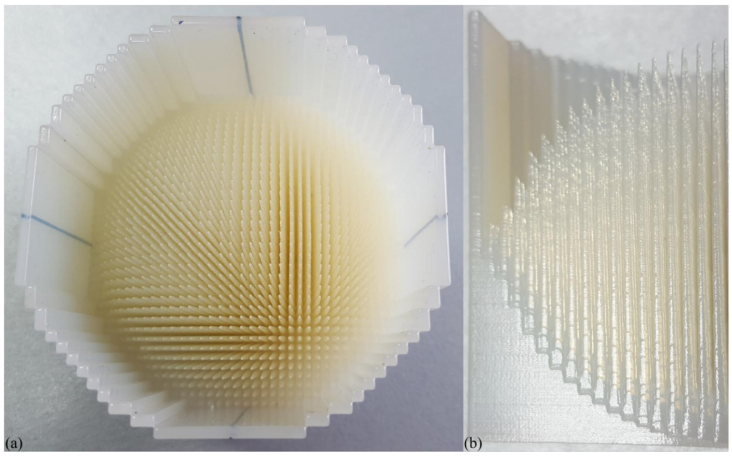

Figure 28: *Example of 3D spherical range modulator; top view and a quarter of it, side view [9].*

5.5 Convolution

The convolution has a central part in our suggested model since it mirrors the multiple Coulomb scattering. The function $scipy.ndimage.gaussian\_filter$ in Python has been used. It is a multidimensional Gaussian filter (see Figure 29).

The parameters of this function are the input, the standard deviation for the Gaussian kernel, the mode and the truncate.

The mode parameter determines how the input array is extended when the filter overlaps a border. The chosen mode is $constant$. The input is extended by filling the values beyond the edge with the same constant, 0 in our case.

$$[1 \quad 2 \quad 3] \longrightarrow [0 \quad 1 \quad 2 \quad 3 \quad 0]$$

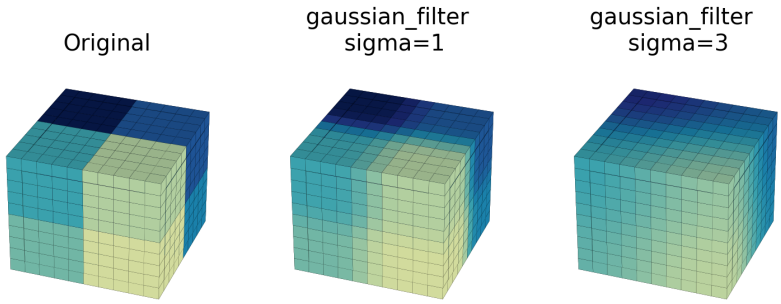

Figure 29: *Gaussian filter applied on test data with different value of sigma [18].*

The truncate parameter gives the number of standard deviations after which we truncate the filter. The parameter is set at 6, giving a kernel size of $2 \times \sigma \times 6$. The truncate at 6 permits to take into account the whole Gaussian bell.

5.6 MCsquare

Now that we have presented the different parts used in the model, we present the main tool for the validation of our results.

There exist two methods to model protons beam: analytical algorithm or algorithm based on Monte Carlo techniques. The Monte Carlo technique is a stochastic method, meaning that the set of parameters values and initial conditions will lead to a combination of different outputs [45].

Protons may undergo one million interactions per cm in a medium giving an extremely complex transport kinematics [54]. The use of random sampling help to solve the proton transport. The principle is to voxelize everything and save the material type to calculate the correct energy loss and cross sections.

Then the trajectory is simulated step by step with random length. It represents the length between two hard interactions [13]. The step length is sampled at the beginning of each step based on the cross section of the hard events. Since the interaction probability can vary along the length, a fictitious interaction is added to keep the total cross section constant. The interaction probability can vary from voxel to voxel depending on the material and density. If the particle passes through more than one voxel, this can add errors. There are two methods to counter this problem [8]. The first, the most accurate, is to stop at each step and use these fictitious interaction mechanisms. The second one, called fast, consists in no longer stopping at each step but at each new voxel, the length of the step is scaled by the local density and the mass stopping power ratio. The energy lost during the step is then noted in a random voxel along the path. However, this fast method may affect the simulation results.

The energy loss during the huge number of electromagnetic interactions are simulated in a condensed way. Only hard interactions are sampled individually. The energy loss is performed at each step and is calculated

[13] The hard interactions are the nuclear interaction, the hard ionization and the fictitious interaction.

using database of stopping power like PSTAR. The hard ionization contribution is subtracted from the total stopping power, leading to a restricted stopping power [8].

For the simulation of the range straggling and the Bragg peak width, they add a Gaussian with a standard deviation of value δE to the mean loss. The angular deflection resulting from the multiple Coulomb interactions is also sampled for each step from a Gaussian distribution.

For the nuclear interaction events, various secondaries will be produced. The elastic proton-nucleus collisions are sampled directly from the ICRU 63 database [8]. Prompt gamma is produced but not transported and neutrons are neglected. All the others charged particles are explicitly simulated. For each element constituting the material, the elastic and inelastic nuclear cross section are summed to obtain the interaction probability. These probabilities are used to sample the target nucleus during the hard interaction.

Finally, all these inidividual cross section are summed to obtain the total hard interaction from which the step length is sampled and the type of hard interaction is randomly sampled depending on the cross section of each process.

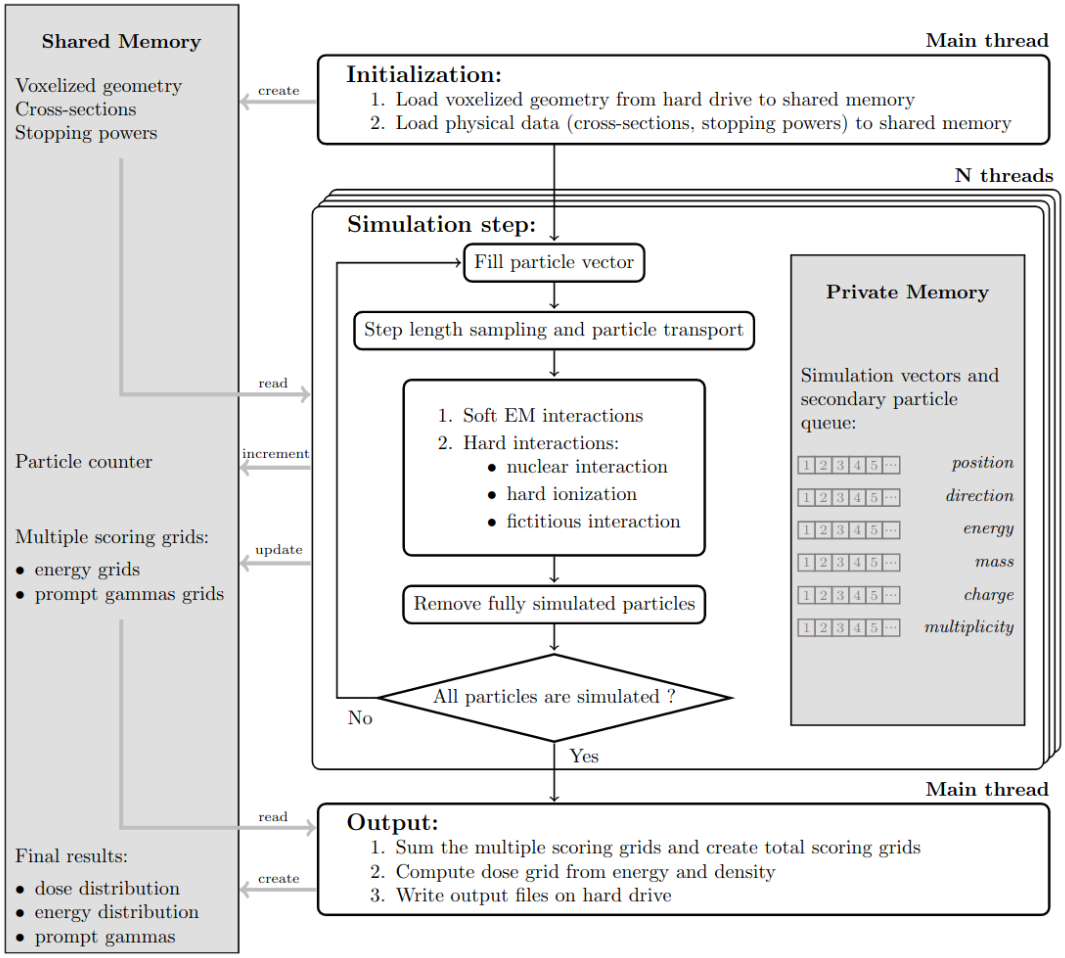

Figure 30: *Flowchart representing the main steps of the algorithm implemented in MCsquare [8].*

Monte Carlo algorithms are known to be the most accurate but take more time. The stochastic noise of the method is reduced by simulating the interaction of a large number of protons which makes the simulation

slow. For this reason K.Souris [8] implemented the fast Monte Carlo code.

MCsquare is an implementation of a fast Monte Carlo. The computation time is reduced by simplifying the physical model and optimizing the algorithmic implementation. One of the techniques is to use the multi-core processors. Since all the particle simulated are statistically independent, we can compute them in parallel and then divide the computation time. The more cores available, the faster we will find results.

The results given by MCsquare are validated and were compared with results of Giant4 Monte Carlo toolkit. This tool can therefore be used to define the expected values. More precisely, we will use a Python application named OpenTPS which is based on the MCsquare Monte Carlo dose engine.

5.7 Color plots and relative difference

The analysis of the results is mostly made in $Python$ by showing a color plot of the dose and creating contour plots of the difference between MCsquare values and ours in several scenarios.

The difference can be expressed in absolute or relative terms. The relative difference with MCsquare or with the reference case can be expressed with the following relation:

$$\text{Relative difference}(\%) = \frac{\text{Absolute difference}}{\text{True value}}$$

6

Validation

Before going on to study the results, it is important to validate our model. In order to achieve this, we will compare different results using on one side MCsquare and on the other side the model explained above.

We will proceed in 3 steps from the simplest to the more complex case. First, a homogeneous water phantom is employed to study the simplest case. Second, the impact of heterogeneity on the dose is studied by simulating the proton beam in a non-homogeneous phantom. Last, a comparison of the spread-out Bragg peak with a more complex range modulator is examined.

6.1 Homogeneous water phantom

The first test involves a mono energetic (100 and 226 MeV) proton pencil simulated in a 100x100x150 and a 100x100x450 homogeneous water phantom. The resulting physical quantities are scored in a grid of 1 mm^3 cubic voxels.

For each energy, two scenarios were considered. The first scenario consists in a beam with an initial Gaussian fluence distribution with a standard deviation of 3 mm in x and y directions centered at position $(80,80)$(as shown in Figure 31). The second scenario consists in a beam with an initial Uniform fluence distribution positioned in $[77:83] \times [77:83]$. All of them were made with 10^{11} protons, taking less than 0.5 seconds.

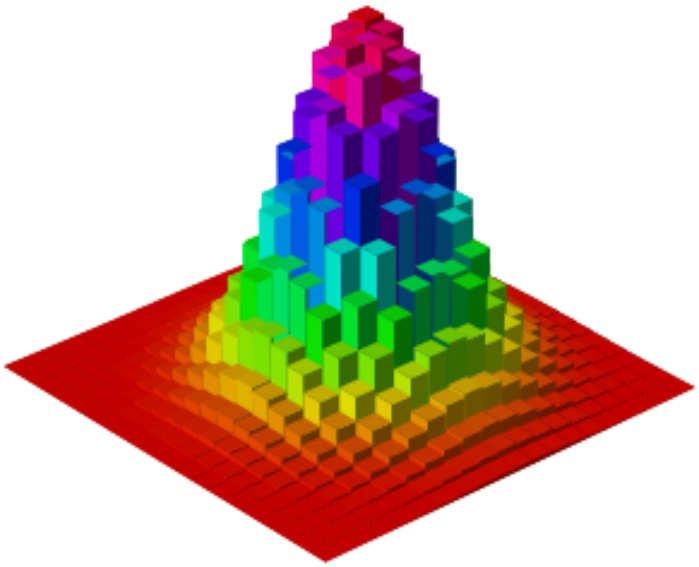

Figure 31: *Initial fluence of a mono energetic radially symmetric Gaussian beam. The height of the 3D representation reflects the fluence, the higher the height, the higher the fluence.*

The first step is to observe a monoenergetic proton beam of medium energy (100 MeV) in a water phantom.

We look at the dose distribution, the Bragg peak and compare this simple case with the similar case proposed by MCsquare. We start by looking at the results with a lower energy because it is faster and allows us to adjust the code more quickly.

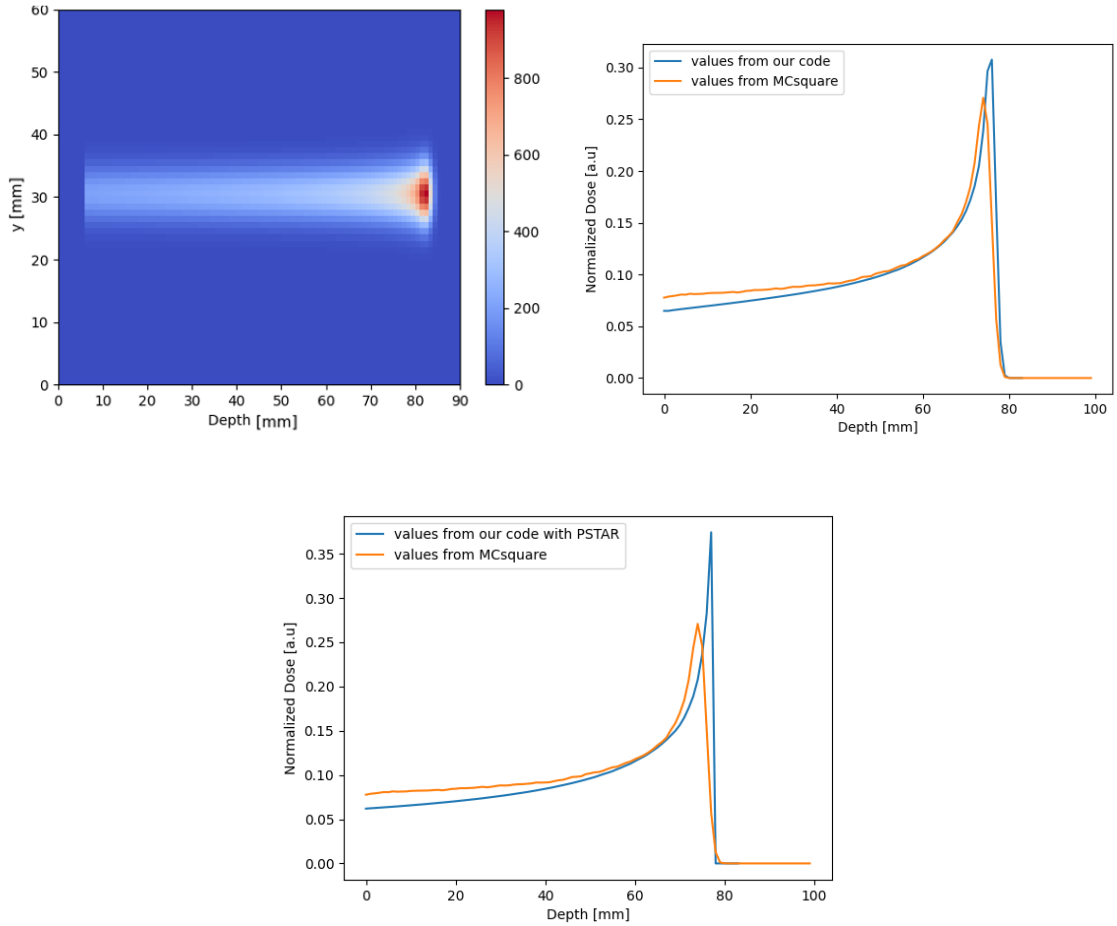

Figure 32: *Longitudinal dose profile (on the left) and curve (on the right) of a 100 MeV proton beam in water with* 10^{11} *protons and a standard deviation of 3 mm, using energy loss from MCsquare. A comparison between the values of MCsquare and our model using the energy loss from PSTAR is visible below.*

The model for a 100 MeV proton beam in Figure 32 shows a difference in the Bragg peak between our model and MCsquare but we see that using the energy loss calculated from MCsquare instead of PSTAR decreases the error gap.

Now that we have adjusted the code, we will take a deeper look at the results at the highest energy (226 MeV for IBA ProteusPLUS). For this, we will not only look at a 2D representation of the dose distribution but also at the 3D one.

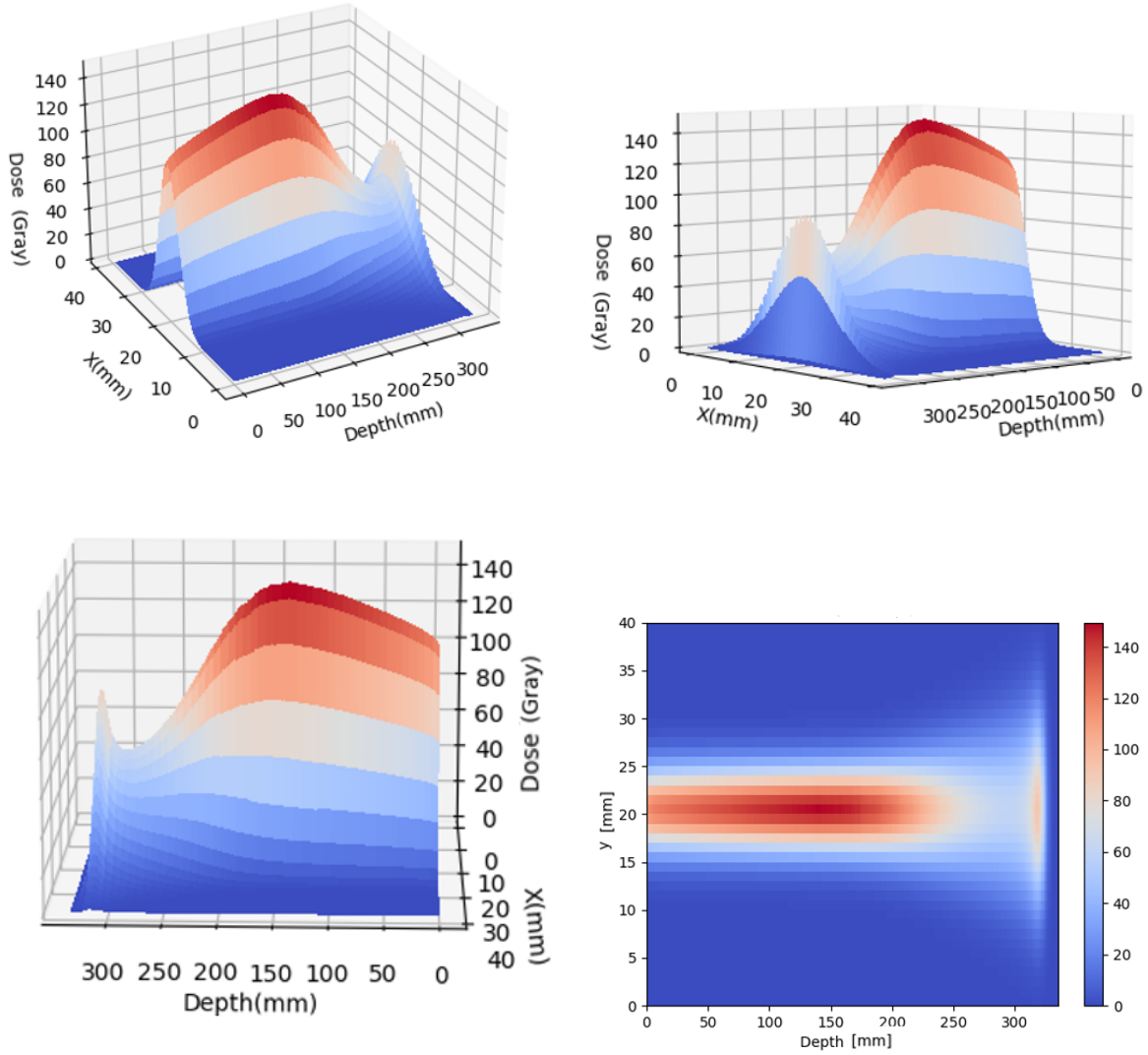

Figure 33: *2-D and 3-D representation of the dose distribution of a beam with a Gaussian fluence distribution with a total of* 10^{11} *protons, a standard deviation of* 3 *mm and an initial energy of 226 MeV. The center of the nozzle is on position (20,20,0). The red represents the highest dose and the blue the lowest.*

Figure 33 shows a 3D and 2D representation of a higher mono energetic Bragg peak (226 MeV) in water phantom found with our model. A first striking feature is the shape of the dose curve before the Bragg peak. Indeed, the maximum dose is not at the peak but before. This phenomenon is explained by the fact that we are not in the case of a single proton. The general shape of the Bragg peak gives the energy loss of a single proton. However, in the case at hand, by drawing a profile at the center of the 3D distribution, we multiply the Bragg peak by a number of protons that decreases in z as the fluence expands laterally. This multiplication explains the particular shape for the 226 MeV beam. At the center in the entrance, the number of particles is indeed high but they loose less energy. At the Bragg Peak, the particles are losing more energy but are more spread.

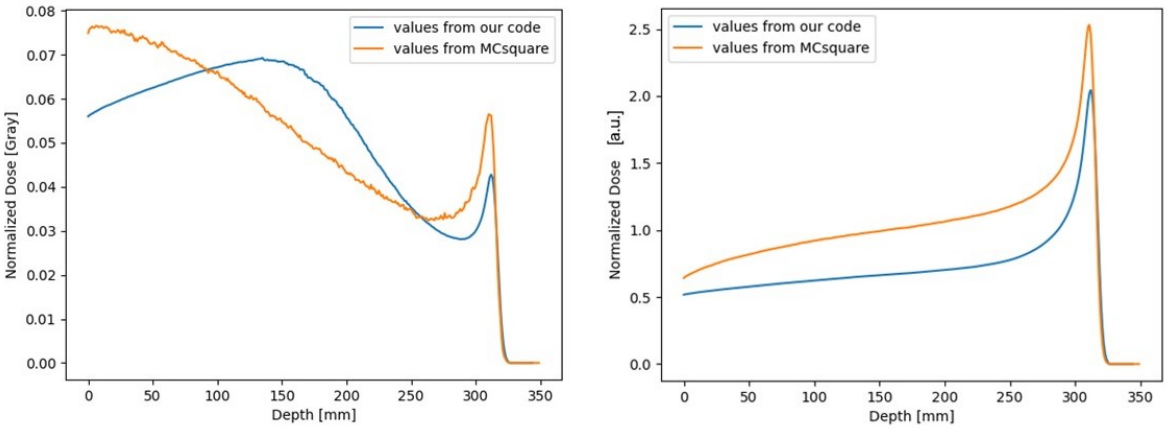

Figure 34: *Longitudinal dose curve (on the left) of a 226 MeV proton beam in water with* 10^{11} *protons and its integral dose distribution (on the right).*

After explaining the cause of the curve shape, we want to compare the results with MCsquare. For this, we focus on the longitudinal central dose curve and the integral dose distribution. The left part of Figure 34 shows that even if a similar phenomenon is present with MCsquare, a difference in behavior before the peak is present. Now, to fall back on the typical Bragg peak curve, we perform the integral dose distribution as shown in the right part. This is calculated by summing all the values in (x,y) for each z.

It allows indeed to fall back on a similar Bragg peak as for one proton. Nevertheless one glaring difference is still visible. This is probably due to the MU-proton relation which would be calculated differently by MCsquare than what we thought. Working with the same unity would solve the problem as discussed later.

After looking individually at two mono energetic beams of different initial energies, the comparison of these two beams shows us that in addition to having a lower range, a lower energy causes a narrower Bragg peak (see Figure 32 and 34). Moreover, in both cases, the spread caused by the multiple scattering has mostly an impact at the end of the Bragg peak. Nevertheless, the impact is higher with a higher energy.

So far, we have been interested in Gaussian initial fluence beams. However, our model allows us to look at other types of beams. Here, we will analyse the effect of an initial Uniform distribution beam of 226 MeV. A 3D and 2D representation of the dose distribution can be seen in Figure 35.

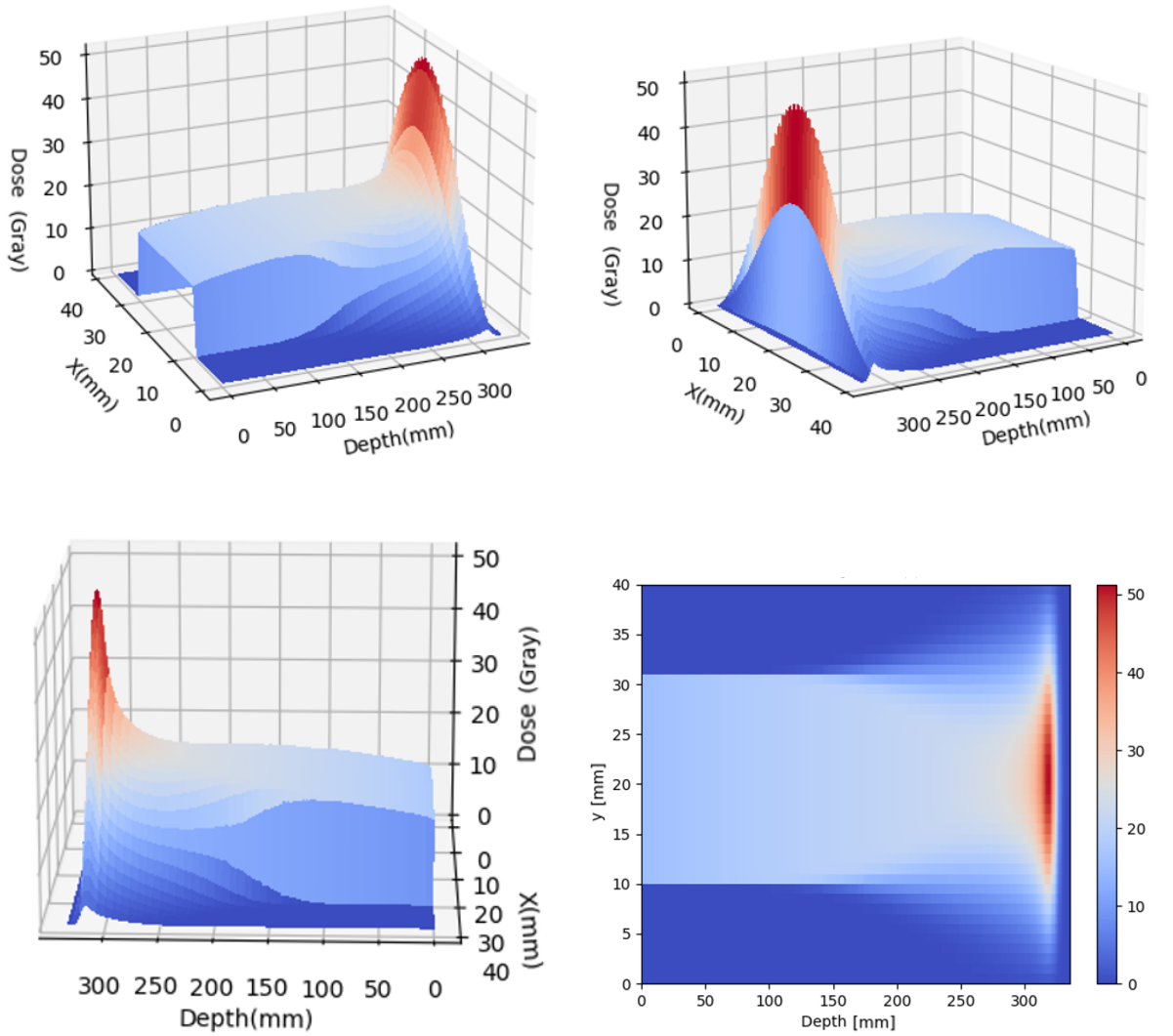

Figure 35: *2-D and 3-D representation of dose distribution of a beam with a uniform fluence distribution with a total of* 10^{11} *protons uniformly dispersed in the squared area in position* $[10:31] \times [10:31]$, $\sigma_x = \sigma_y = 3mm$ *and an initial energy of 226 MeV.The red represents the highest dose and the blue the lowest.*

The dose distribution in the Uniform case differs. For the Uniform initial distribution, the dose is mostly deposited at the Bragg peak unlike the Gaussian distribution (see Figure 33 and Figure 35). However, similar to the Gaussian case, scattering is mainly present at the end of the beam. We note that the fluence is initially Uniform but is transformed on its way and becomes Gaussian. This behavior may be explained by scattering and causes a clustering of fluence in the center of the beam.

After studying the dose profiles and comparing the Gaussian cases with MCsquare, we will now look at the lateral scattering. These are performed under the same conditions as the 226 and 100 MeV beams above. We want to look at the lateral dose at different depth to analyse the evolution of the beam depending on the initial energy and initial fluence distribution.

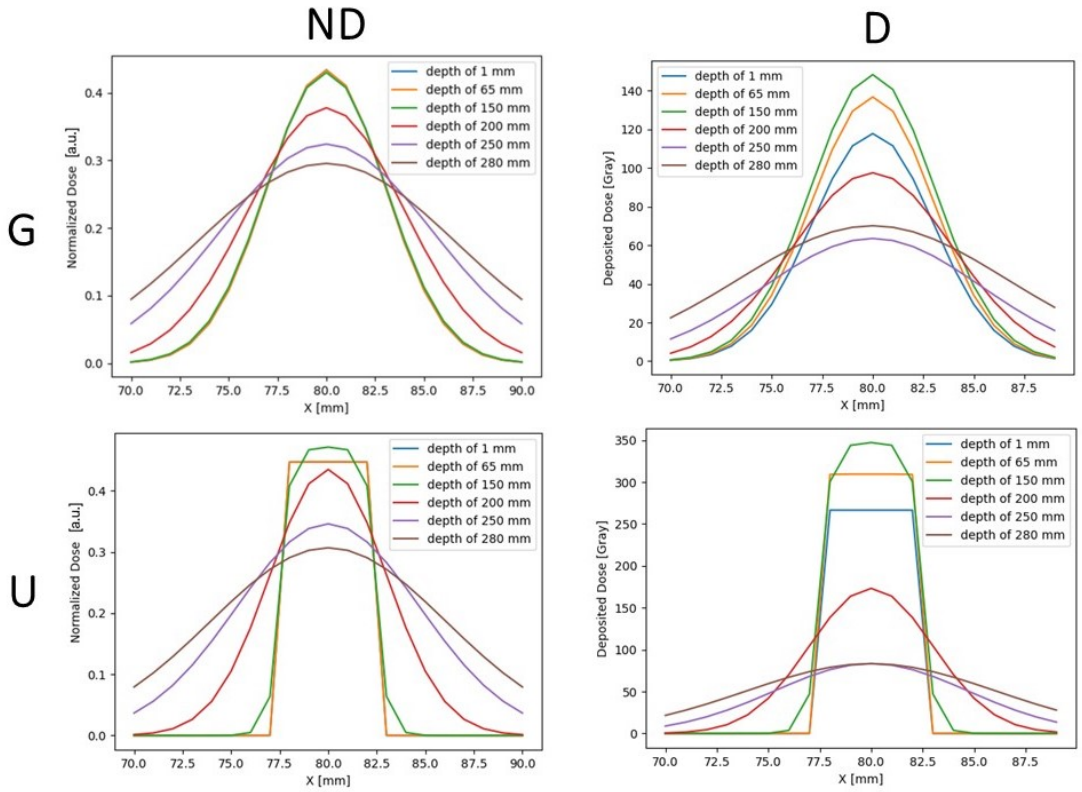

Figure 36: *Representation of the lateral spreading of the dose (D) and normalized dose (ND) of a 226 MeV beam with Gaussian distribution (G) and a uniform distribution (U).*

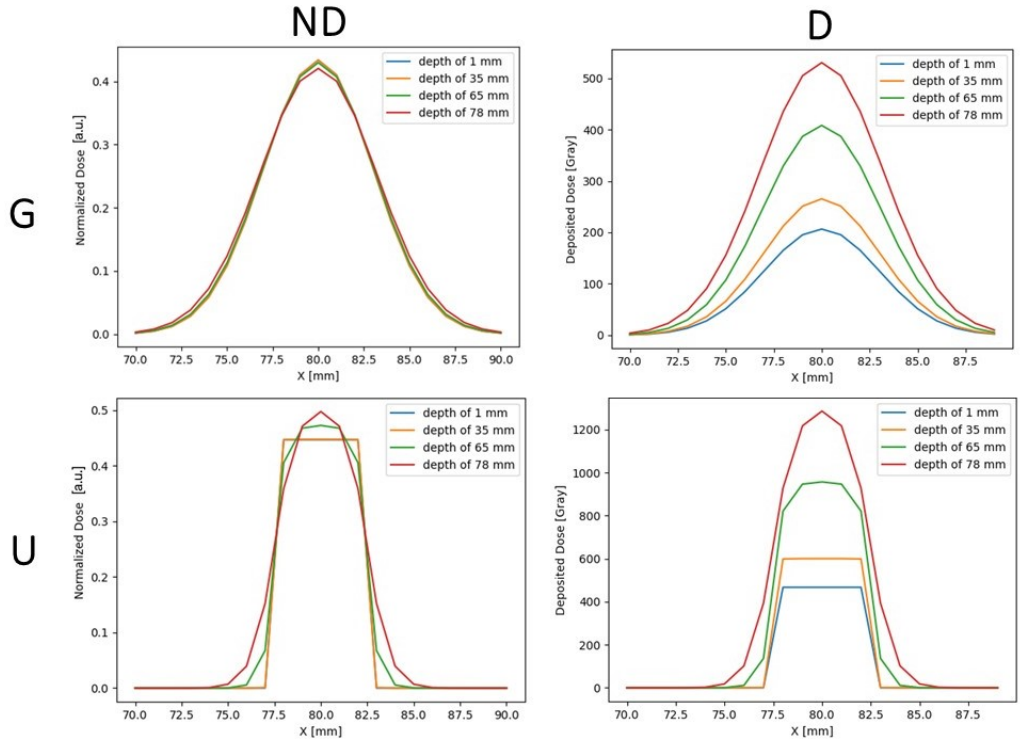

Figure 37: *Representation of the lateral spreading of the dose (D) and normalized dose (ND) of 100 MeV beam with Uniform distribution (G) and a uniform distribution (U).*

The figures show that the lateral scattering increases with the depth in water but not linearly. The normal-

ized dose (ND) shows the lateral spreading of the dose in water. It confirms that the scattering is mostly present at the end of the beam. The comparison between Figure 36 and Figure 37 shows that the bigger the initial energy, the bigger the lateral spread. Moreover, the lateral dose profiles with an initial Uniform fluence become closer and closer to a Gaussian as depths increase.

6.2 Heterogeneous geometries

Having studied the simplest case (i.e. homogeneous water phantom), we want to look at the slightly more complex situation which represents heterogeneous geometries. When a proton beam passes through a complex heterogeneity, the consequent variations in lateral dispersion can lead to substantial dose heterogeneity. An inadequate management of the lateral dispersion is one of the important weaknesses of the semi-empirical methods of dose computation used in the current treatment planning systems [52].

As this study works only with water, materials of different density are represented by their water equivalence. So, a more dense material will be represented by a higher water length compared to a less dense material. We will see that it is not really equivalent. However, there are still similarities.

6.2.1 The bone lung scenario

We look at the dose calculation accuracy in a known heterogeneous shape. The proton pencil beam is simulated in a 100x100x150 or 100x100x450 mm^3 grid containing a water shape represented in Figure 38 mimicking a cortical bone and lung slab (two different materials) forming an interface along the beam.

It is known that bone is much dense and causes more scattering than lung. Even if our model do not deal with two materials of different densities, the configuration of the shape is still interesting to study. In the same idea than with bone, in the thicker water volume represented in blue in Figure 38, there will be a more important accumulation of scattering. This scattering also allows the proton to escape from the material and this more and more as we go through it. This shows us that the two cases are not so far apart.

However, the direction of proton through the range modulator will have an impact on the comparison with the real bone lung scenario. In our case (look at Figure 38), the protons that escape from the thicker material won't be attenuated until they arrived at the water phantom. To represent more precisely the case of different materials, it would have been necessary to cross the shape in the other direction, allowing protons escaping from the thicker material to pass through the shorter volume of water. However, the comparisons with MCsquare in this section are done using the same shape formed only of water and therefore allows us to validate our model.

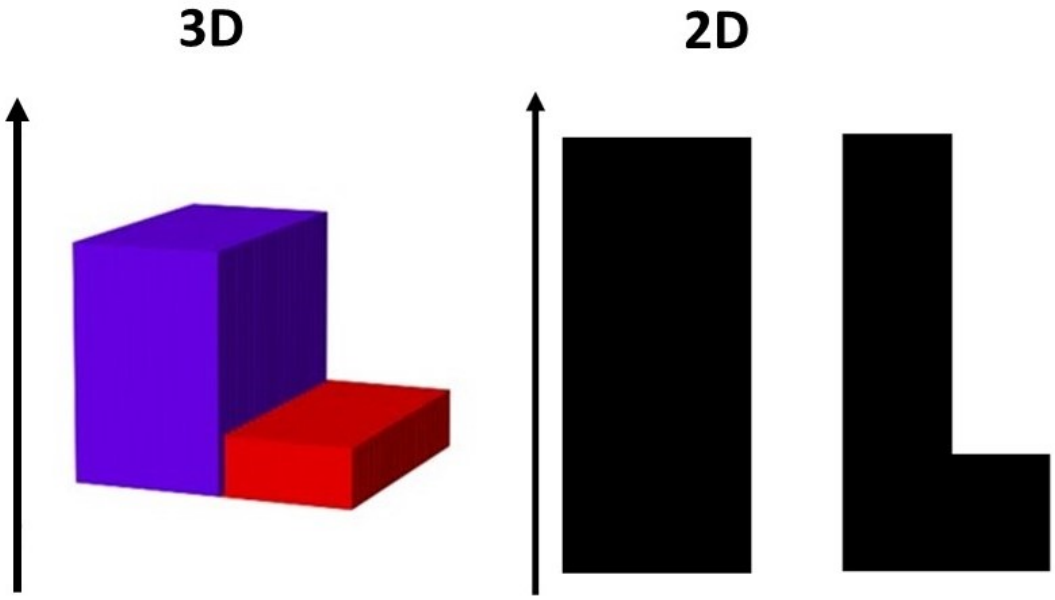

Figure 38: *3D and 2D representation of the range modulator used in the bone lung scenario. The blue part has a height of 40 mm representing the bone part and the red part has a height of 10mm representing the lung part.*

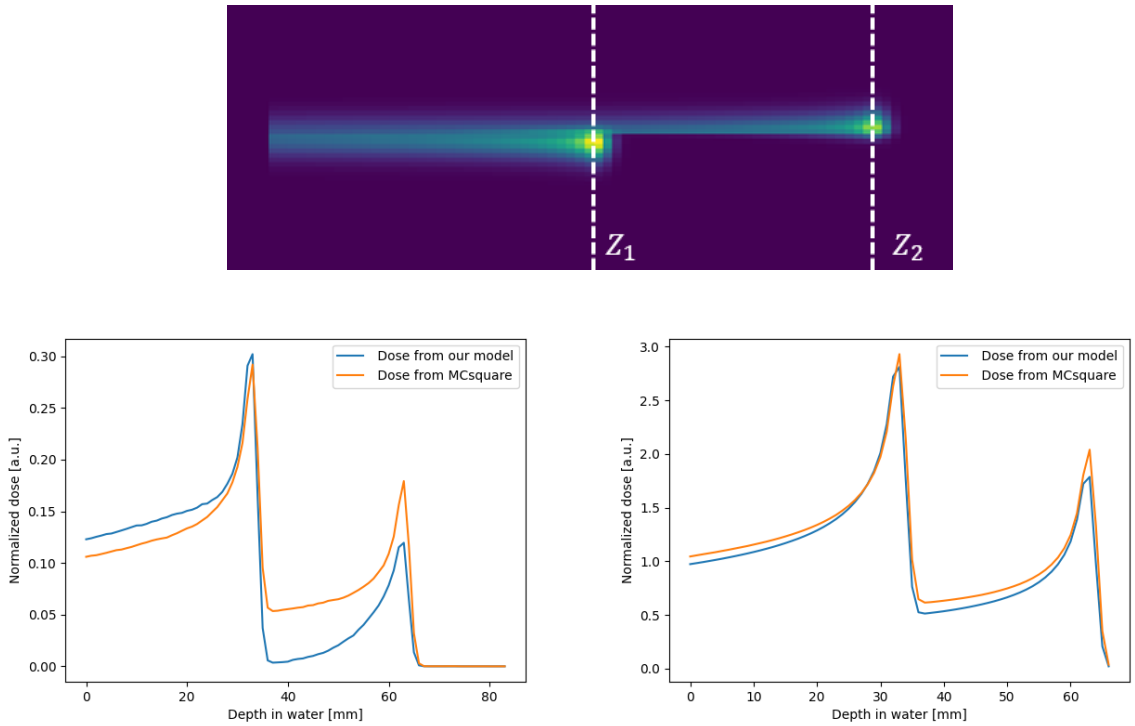

Figure 39: *Dose deposited by a 100 MeV proton pencil beam passing through the shape in Figure 38 (above). Comparison of the Longitudinal depth-dose curve (on the left) and integrated depth-dose curve (on the right) of the 100 MeV proton pencil beam with Mcsquare. The beam representation above begin in the range shifter and below in the water phantom : $Z_1 = 35\ mm$ and $Z_2 = 65\ mm$.*

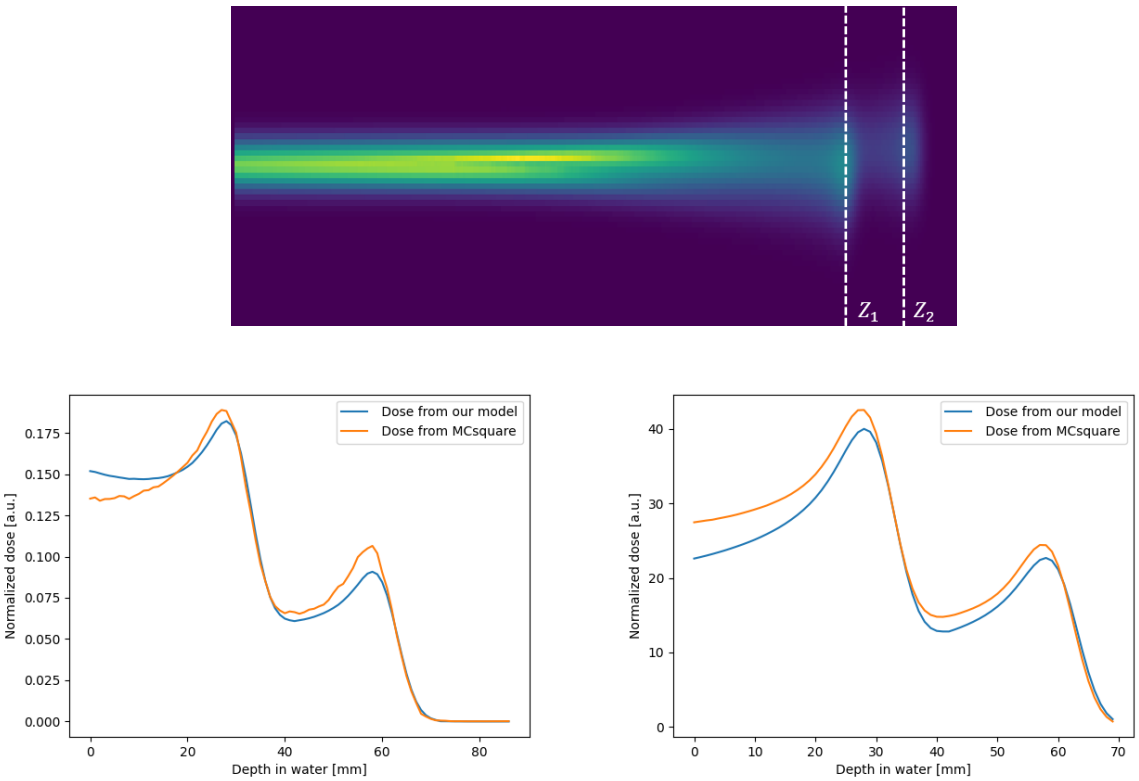

Figure 40: *Dose deposited by a 226 MeV proton pencil beam passing through the shape in Figure 38 (above). Comparison of the Longitudinal depth-dose curve (on the left) and integrated depth-dose curve (on the right) of the 226 MeV proton pencil beam with Mcsquare. The beam representation above begin in the range shifter and below in the water phantom :* $Z_1 = 278\ mm$ *and* $Z_2 = 308\ mm$.

We look at the prediction of the model with an energy of 100 MeV and 226 MeV (see Figure 39 and Figure 40). A first observation is that our simulation underestimates the dose at the first peak and even more at the second one. The error is even bigger when working with low energy (see left part of Figure 39). However, as we study the case of FLASH proton therapy, the high energy error is more interesting to study because the FLASH therapy beam is sent with the highest energy possible. We see that despite small differences before and at the peaks , the results remain strongly aligned.

When we look more precisely at the difference in the 226 MeV beam, two methods are possible: absolute or relative error. Figure 41 shows with contours the positions of the highest absolute errors which are before the peak and at the second Bragg peak. However, this is mostly because the values are the highest at these areas. The absolute method is not the most appropriate indicator of the error. For the relative error, the biggest difference is after the peak. This is due to errors in the computation of the range straggling and the angles of multiple scattering which is more important at the end of the beam. As explained above, the path of the proton is indeed not always straight. To model this phenomenon the energy spread has been calculated from MCsquare and not PSTAR. This method allows us to approach the results of reality but a difference at the end of the beam remains visible.

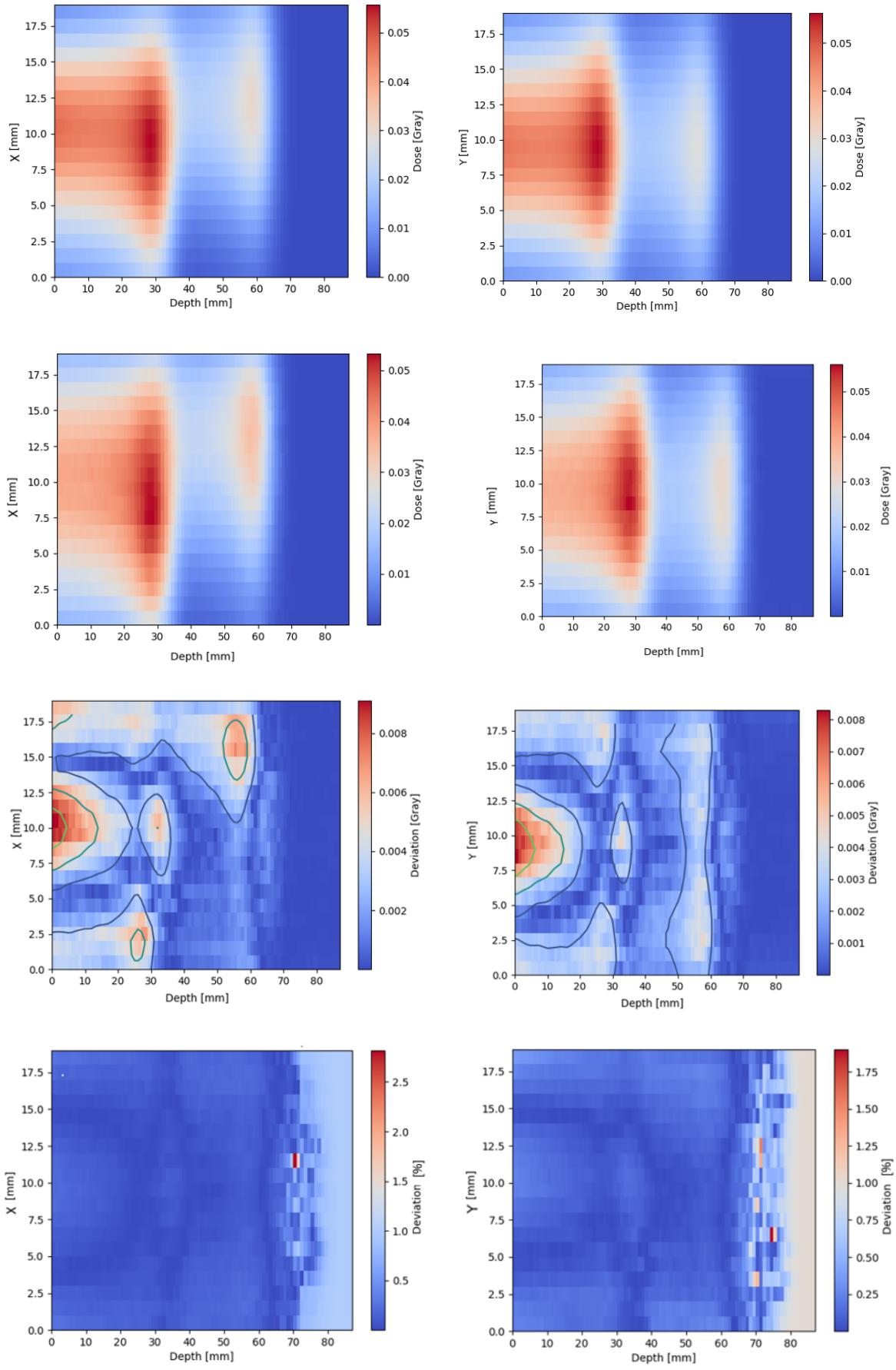

Figure 41: *2D representation of the longitudinal normalized dose in the X plan (on the left) and in the Y plan (on the right). The results of our model are shown in the first two dose images, the two following are results from MCsquare and the last figures show the absolute and relative difference between our model and MCsquare.*

Simplification in the 3D range modulator

As explained above, the scattering is particularly important at the end of the curve. To simplify the process, we could ignore the scattering in the 3D range modulator and compare the simplified results with MCsquare. Figure 42 shows that the relative difference is similar in the simplified case.

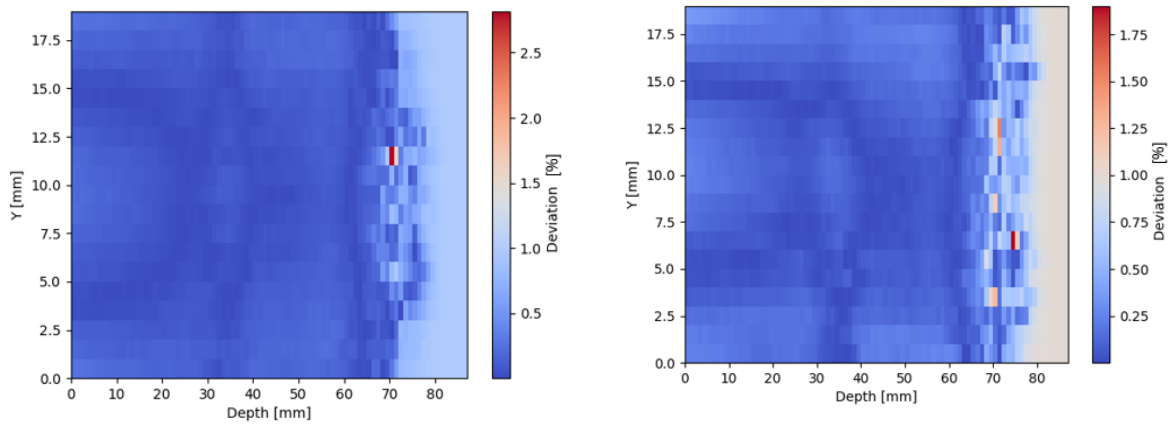

Figure 42: *2-D representation of the relative difference between MCsquare and our simplified model.*

6.2.2 The bone in water scenario

In this part, we want to look at another configuration of heterogeneous shape translated into water using the water equivalent length. The shape is designed to approximate the effect of a denser material in water (e.g. a bone in water). However, in our case, we do not have one volume submerged in another. The beam first passes through the water column representing the denser material before reaching the water phantom (see the left part of Figure 43).

For this case we change the shape of the initial fluence from Gaussian to Uniform. The goal is to analyze the created dose profile and to compare it with a similar situation using other methods including another analytical algorithm. The 226 Mev proton beam is simulated in a 100x100x450 mm^3 grid. The bone is expressed with water equivalence by a water column at the centre of the object (see the blue part of the object in Figure 43). In the water column, there will be a more important accumulation of scattering and the protons leaving the column will eventually cross the volume of water. In the same way, protons passing through a bone in water will undergo more scattering and protons escaping the bone will pass through the water. This shows that the two situations are not that far apart.

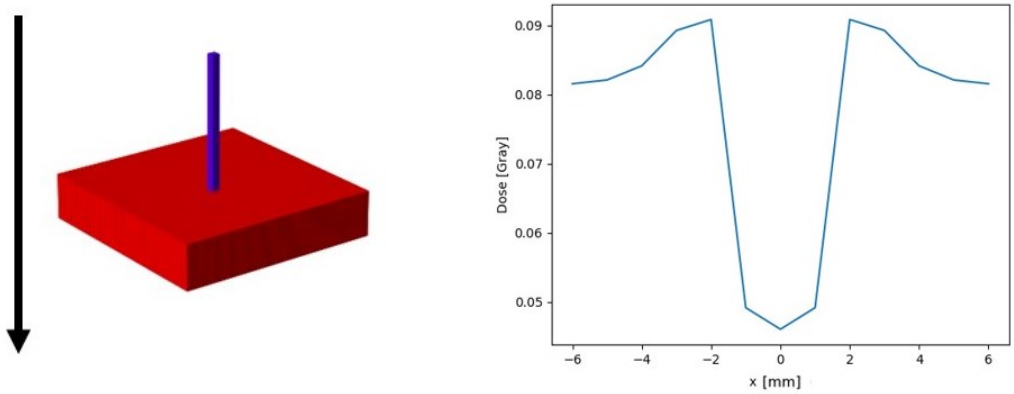

Figure 43: *3D representation of a heterogeneous range modulator (on the left) and dose profile using this modulator with a uniform beam (on the right). The water column, blue part, represent the water equivalent length of a bone and the red part represents an homogeneous water phantom.*

The particular dose curve shown on the right of Figure 43 is explained by two elements. First, when the protons cross the water column, some of them do not move in a straight line and will be deflected outside the water column, so the number of protons around this point is larger. Then, the protons that have passed through the entire water column will lose all their energy earlier. Moreover, the protons having crossed a part of the column will have their Bragg peak before the protons further away from the column. All these elements explain the dose curve in Figure 43.

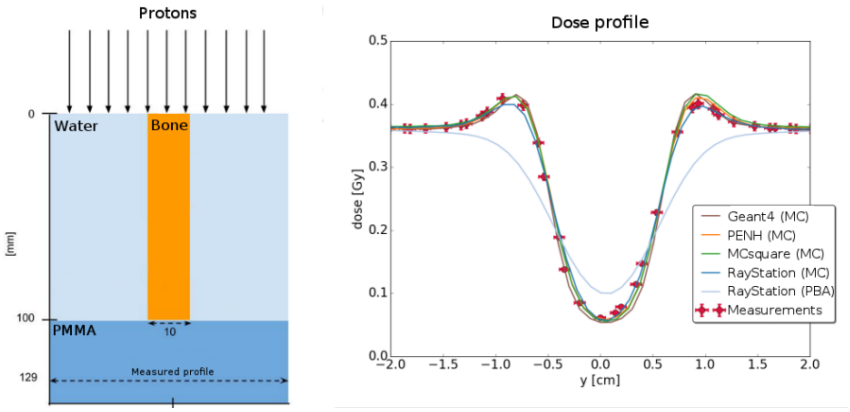

Figure 44: *Comparison of analytical pencil beam algorithm (PBA) and Monte Carlo dose calculation results in a heterogeneous phantom. The dose profiles are compared at 129 mm depthand averaged over 4 mm for Geant4.9.5 (brown line), PENH (orange line), MCsquare (green line), RayStation MC (blue line), RayStation PBA (shadowed blue line) and experimental data (red circles points) [8].*

To be able to compare our results with those presented in the research of K. Souris, it is important to look at the right place. The results presented in Figure 44 represent the situation of a bone submerged in water. The results are comparable only at the bottom of the volume and not at the beginning. In our case, at the beginning of the volume the beam will have already crossed a column of water, while in K.Souris's research the bone is not yet crossed. However, the dose at the bottom of the volume should have a similar profile. The profile shown in Figure 44 is at a depth of 129 mm and our profile is 145 mm deep. Both depths are supposed to be deep enough to be comparable.

As expected our dose profile seems consistent with the results in Figure 44. The PBA in Figure 44 represents the analytical pencil beam algorithm and MC, the Monte Carlo dose calculation. Our simulation is also analytical but seems to show a behavior closer to the MCsquare results than the one proposed in the analytical model in Figure 44.

6.3 Test spread out Bragg peak

The ultimate goal of this model would be to use it to find a 3D range modulator to deposit a uniform dose at the desired location. This type of shape is often more complex than those analyzed so far. The goal of this part is to look at the results using a range modulator that gives a spread out Bragg peak and compare it with MCsquare.

We work here with a beam of 100 MeV. The program used to find the 3D range modulator allowing a SOBP, does not work correcly for low energies. For this reason, we change the value of the standard deviation of the initial Gaussian beam to 4mm instead of 3mm. Using a wider Gaussian beam gives indeed better results. The shape used to create the most uniform dose possible at 100 MeV is shown in Figure 45.

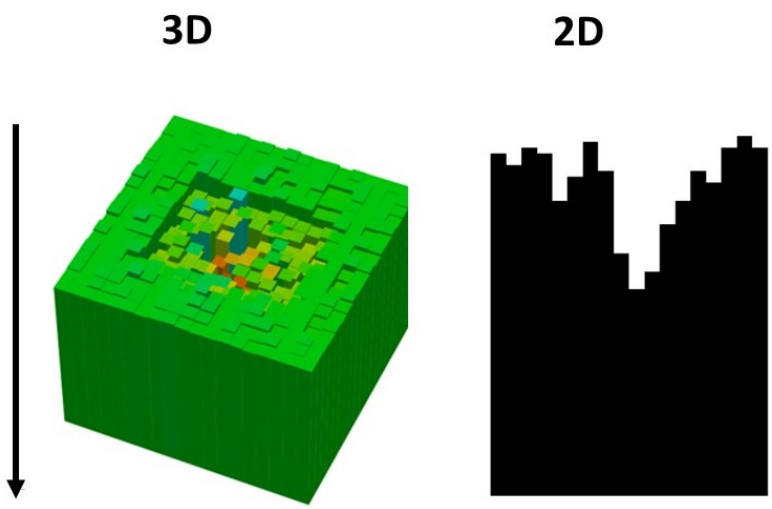

Figure 45: *3-D (on the left) and 2-D (on the right) representation of a range modulator used for Figure 46.*

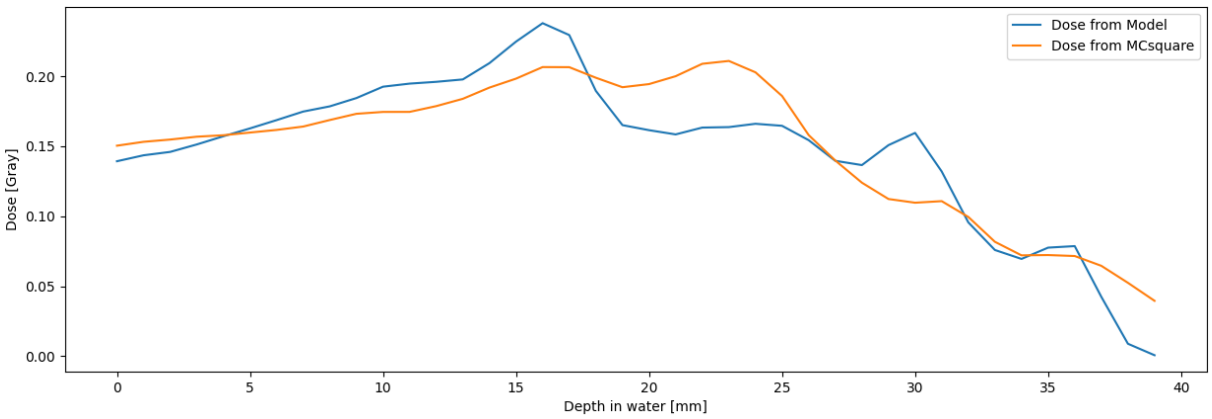

Figure 46: *Comparison of the spread Bragg peak curve with MCsquare given by a Gaussian distribution beam of 100 MeV and a standard deviation of 4mm.*

The created design allows the deposited dose profile to be strongly degraded without achieving this SOBP which is impossible with a resolution of 1x1 mm. Both curves have the same global behavior. The peaks are more or less at the same depth. However, a significant difference is visible, especially at the level of the second peak.

The use of the more complex form confirms that, while our model does not give results accurate enough to be used in clinical tests, it still gives a first general idea of the behavior.

6.4 OpenTPS

For the comparison of the simple cases, an additional code following the steps described in this thesis has been implemented in OpenTPS. The implementation directly in OpenTPS allows us to align perfectly between Monte Carlo and analytical simulations because all calculations are done in the same tool. The exact alignment before could indeed not be guaranteed.

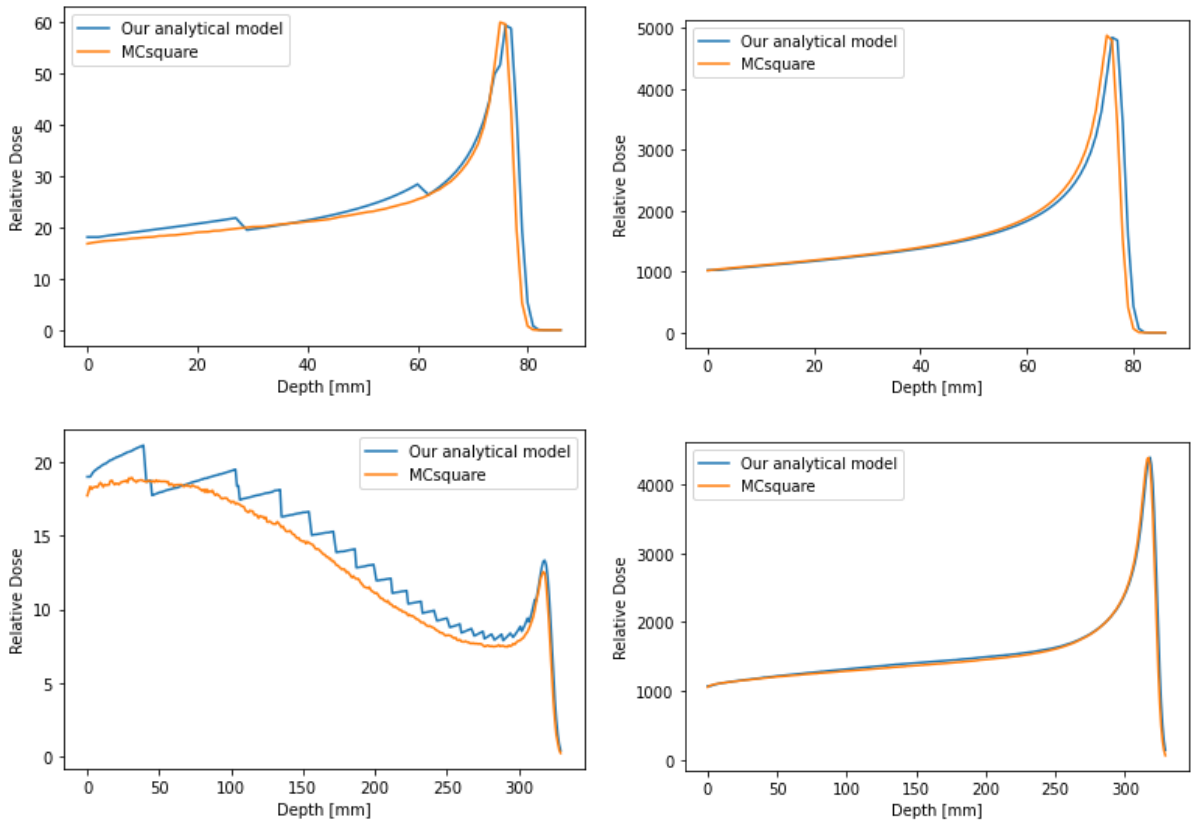

Figure 47: *Dose deposited by a 100 MeV (above) and a 226 MeV (below) proton pencil beam (on the left) and their integrated dose distribution (on the right).*

Concerning the simulation of a homogeneous beam, the implementation directly in OpenTPS allows us to find a behavior more similar to MCsquare compared to the dose before the Bragg peak but also an IDD now identical (see Figure 47). This is especially noticeable with the 226 MeV beam and confirms us in the idea that the difference in the IDD was mainly due to a MU-proton conversion problem.

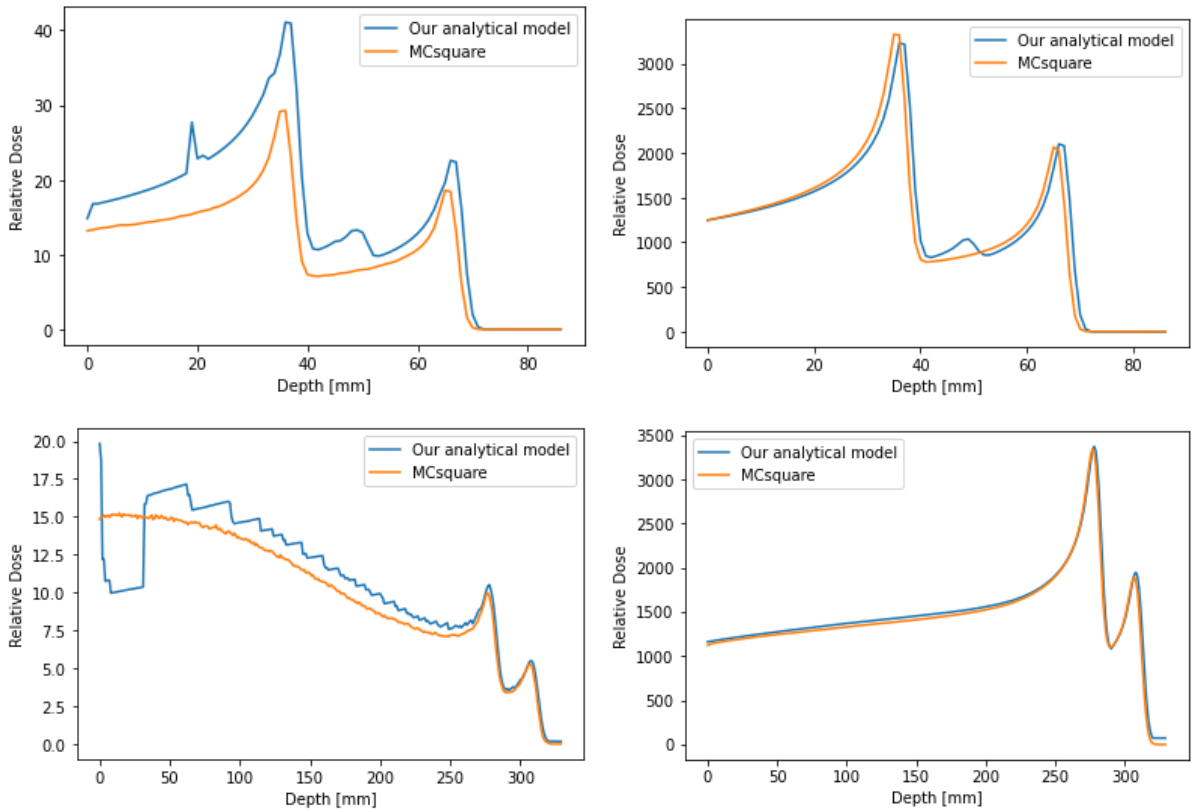

Figure 48: *Dose deposited by a 100 MeV (above) and a 226 MeV (below) proton pencil beam (on the left) that has gone through the shape in Figure 38 and their integrated dose distribution (on the right).*

In the heterogeneous medium, the dose centered with 100 MeV is not very good contrary to the one with 226 MeV (see Figure 48) but once again FLASH therapy focuses on high energies. The most interesting place in our case is at the level of the peaks and these are aligned. In this case also the IDD are very similar or even identical.

7

Study of the impact of the geometrical characteristics of the 3D range modulator on the dose distribution

The validation of our model allows us to use it to study the impact of different elements of the simulations. The objective of this chapter is to understand the impact of the 3D range modulator on the deposited energy distribution. Different shapes are compared by their dose distribution, maximum dose, etc. All these changes were made in relation to a standard geometry and the results of deposited energy were compared to those.

During, the study of results we can meet two types of simulation. Simulations of type 1 have been made with a beam of 226 MeV or 100 MeV with a symmetrical Gaussian distribution with a standard deviation equals to 3 mm. Simulations of type 2 have been made using a beam with a Uniform distribution. The proton beam was set at $X, Y, Z = (50, 50, 0)$ and the given range modulator is centered at $(50, 50)$.

The generic geometry assembly can be seen in Figure 22. All compartments are made of water and the material that surrounds the complete structure is represented as the void.

7.1 Simple pyramidal shape VS Multiple pyramidal shape

Here we will study the impact of a geometrical reorganization of the 3D range modulator while preserving the fluence vs. elevation histogram. That is, for each spike of the range modulator, we have a table showing the cumulative fluence. We sum the cumulative fluence of spikes that have the same elevation between them. When creating an equivalence, we take care that this sum is the same as in the reference case for all elevations. This means that for each elevation, we want the same number of protons incident in the reference case and the equivalences. In other words, the integral depth dose profiles (IDD) should be the same for all configurations. On the other hand, we expect to have differences in the spatial (3D) dose distribution. For the same reference shape, it is possible to define several equivalent shapes.

To preserve the IDD, the simulations performed in this chapter are of type 2. The resolution of 1 mm indeed does not allow to realize shapes accurate enough to preserve the fluence vs. elevation histogram for a Gaussian beam.

Several comparisons are made in this chapter. First, a round multi-spike shape inspired by the shape from the study of P.Penchev [13]. Then, the simpler cases of one and three tetrahedra are compared.

7.1.1 Round Shape vs. pyramidal shape

The first comparison is between a round shape (reference) and the equivalent simple pyramidal shape. The equivalents must preserve the fluence vs elevation histogram. The method used to find the equivalence is to, in

a first step, look at the cumulative fluence at each spike of same height in the round hedgehog, and in a second step, create a tetrahedron so that the cumulative fluence for each elevation is the same in both shapes. However, finding the equivalent shape is not trivial and may take some time because we are looking for equivalence by trial and error. As we know that the scattering is small at the beginning, we start with the pyramid having the same number of spikes of each elevation as the reference shape. Then we look at the cumulative fluence of each elevation starting with the highest and add or remove spikes until we find the same cumulative fluence as in the referent case. It is enough to repeat this step for all the elevations. The round reference shape and an equivalence found using this method are shown in Figure 49.

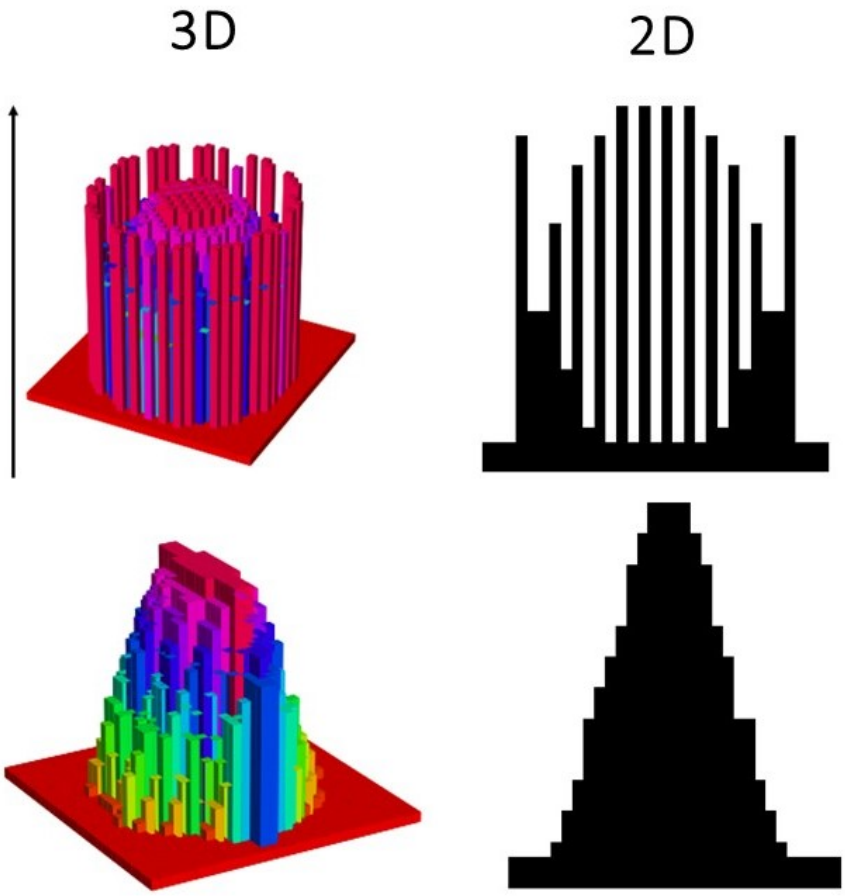

Figure 49: *3-D (on the left) and 2-D (on the right) representation of the round shape tower (above) and its first pyramidal equivalent shape (below). The shapes have a height of 25 mm and the base length is 21 mm (D1=55 mm and D2=85 mm).*

Figure 50 shows the dose distribution of the two shapes. Even if the IDD is identical in both cases (see Figure 51), the 3D dose distribution differs. The difference is especially present after the peak. The dose of the round shape after the peak remains high in the center in contrast to the pyramidal case. The distribution in the XY plan at a depth of 275mm confirms that the dose is mostly at the center in the referent case and on the sides in the Y axis for the first equivalence. However, when we look at the maximum dose, these occur more or less at the same depth.

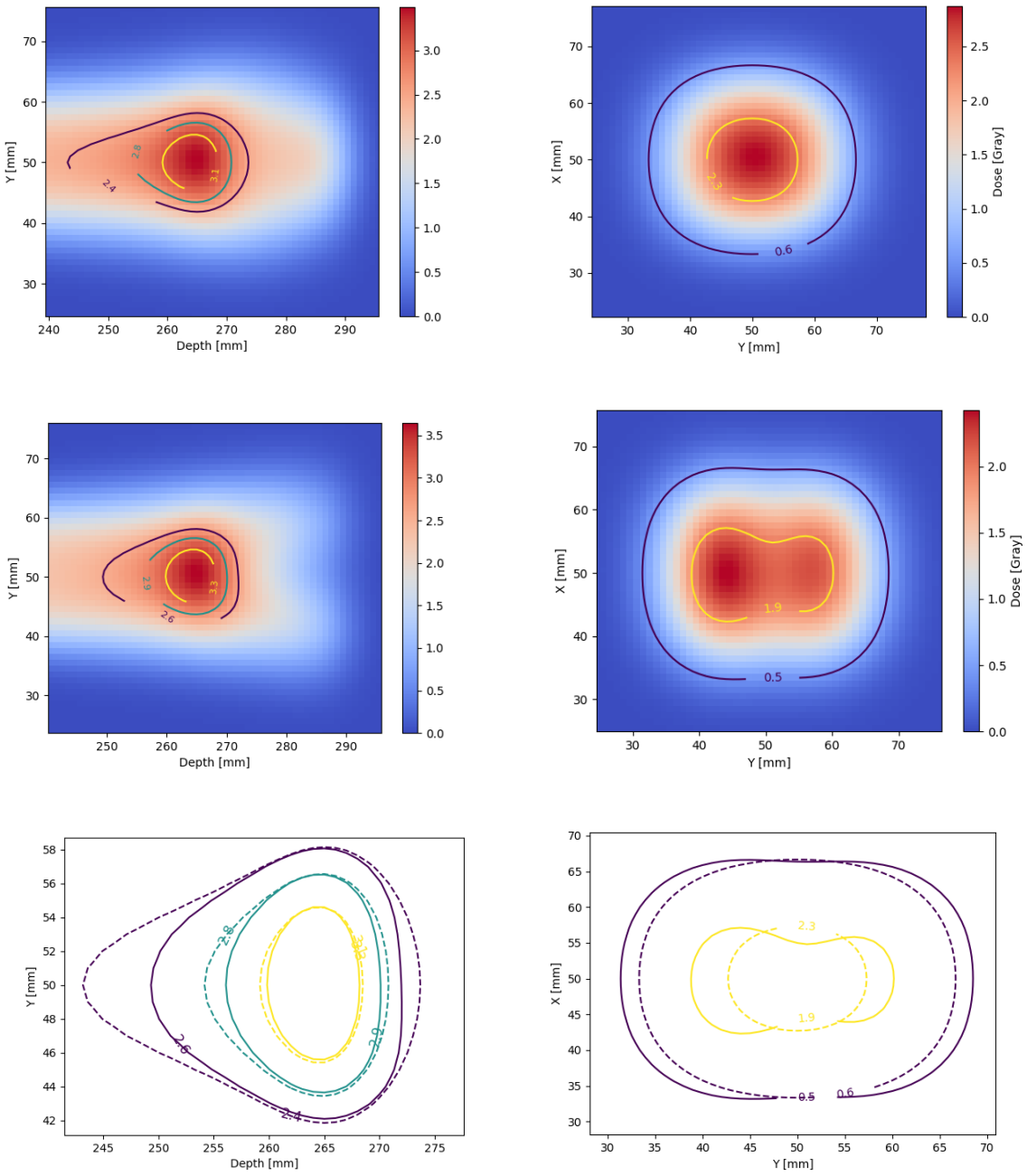

Figure 50: *The right part represents the transversal dose at 275 mm and the left part represents the longitudinal dose profile at the center. The upper part represents the dose profile of the round shape, the centered part the first equivalence and the bottom part is the comparison of the isolines dose (dashed= round and line= equivalence). All the curves are normalized in each case to 1 at the mean dose.*

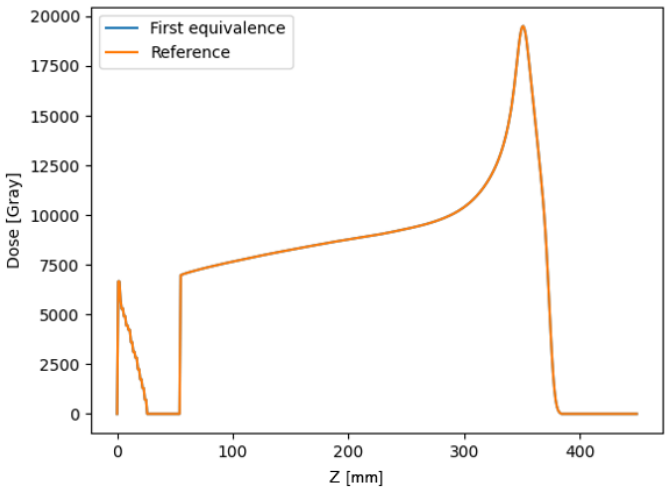

Figure 51: *IDD of the round shape (Reference) and an equivalent pyramidal shape.*

In a second step, we look at the effect of a time-saving simplification during the equivalence search. As explained above, scattering has especially an impact at the end of the beam and could be ignored. With this simplification, the equivalent pyramidal shapes become simple to determine. We just have to take the pyramid with the same number of spikes of each elevation as the reference case. Since the range modulator is a matrix containing the heights of the spikes in each (x,y), the equivalence is simply found by rearranging this matrix without changing the values. The first equivalence has been made to have similar total volume and similar surface at each X's cut (see Figure 52). It is not a complete pyramidal shape. The second equivalence is a complete pyramidal shape but does not have the same surface at each X's cut anymore (see Figure 54).

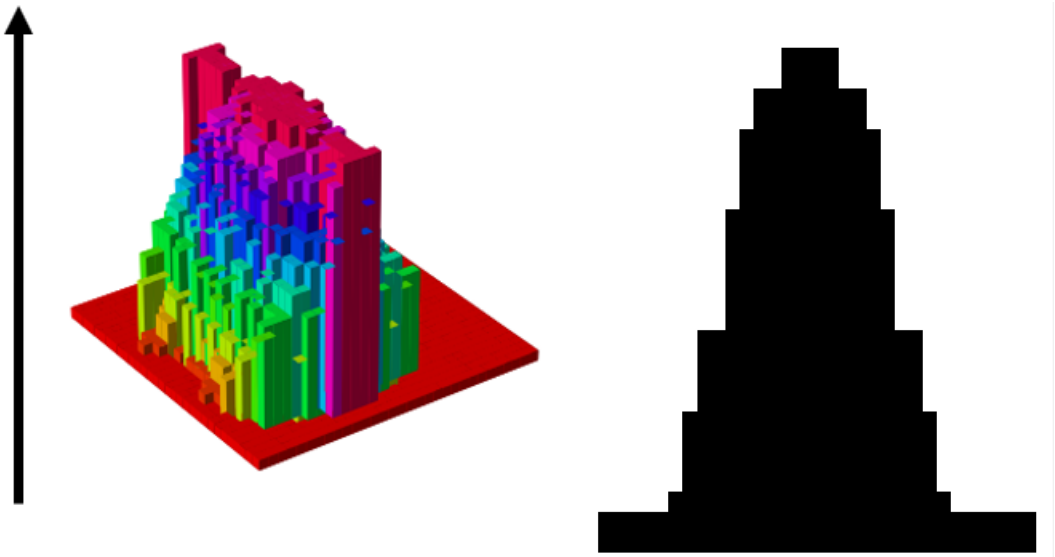

Figure 52: *3-D (on the left) and 2-D (on the right) representation of the first pyramidal equivalent shape with the simplification.*

Figure 53 shows the dose profile produced for the reference and the first equivalence using the simplification. The results obtained with the simplification are quite similar to those without. The same behavior is

visible on these different results. The distal part of the reference range modulator, which is the height of each spike, seems to influence the proximal part of the dose and the proximal part of the modulator (i.e. the base of the hedgehog) to influence the distal shape of the target.

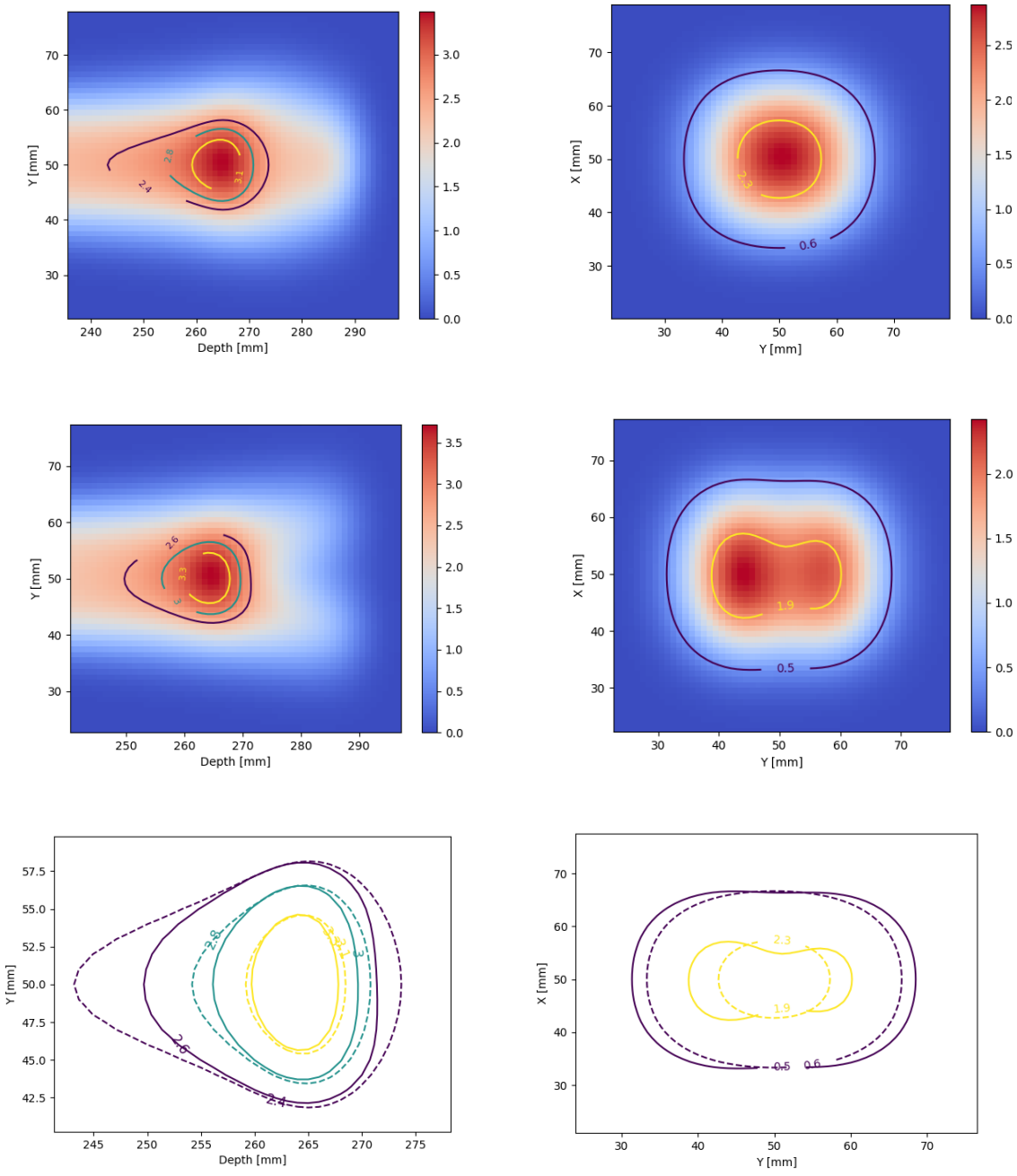

Figure 53: *The right part represents the transversal dose at 275 mm and the left part represents the longitudinal dose profile. The upper part represents the dose profile of the round shape, the centered part the first equivalence and the bottom part is the comparison of the isolines dose (dashed= round and line= equivalence). All the curves are normalized in each case to 1 at the mean dose and are found with the simplification.*

The pyramid shape allows to define the proximal part of the target shape. However, this type of configuration gives less freedom for the distal part. On the other hand, this kind of design is more easily produced than the reference.

These first results point to the fact that the change in shape style has an impact on the 3D distribution.

The shape in Figure 54 is also a pyramidal equivalent to the reference but different from the first equivalence. The idea is to look at the differences between two close shapes. The results of Figure 55 show that the isoline contour dose are similar for the two pyramidal equivalences but not exactly the same. More precisely, the isoline of 70% dose is deeper with the first equivalence than with the second. This means that even two similar shapes produce significant differences and every millimetre of the modulator has an impact.

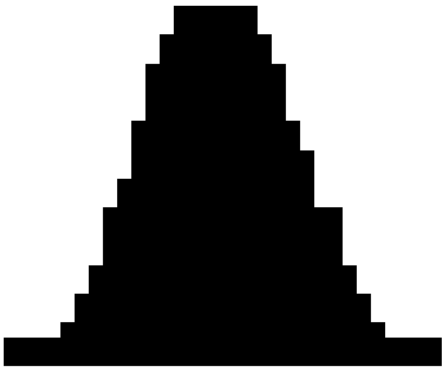

Figure 54: *2-D centered cut of the second pyramidal equivalent shape with simplification.*

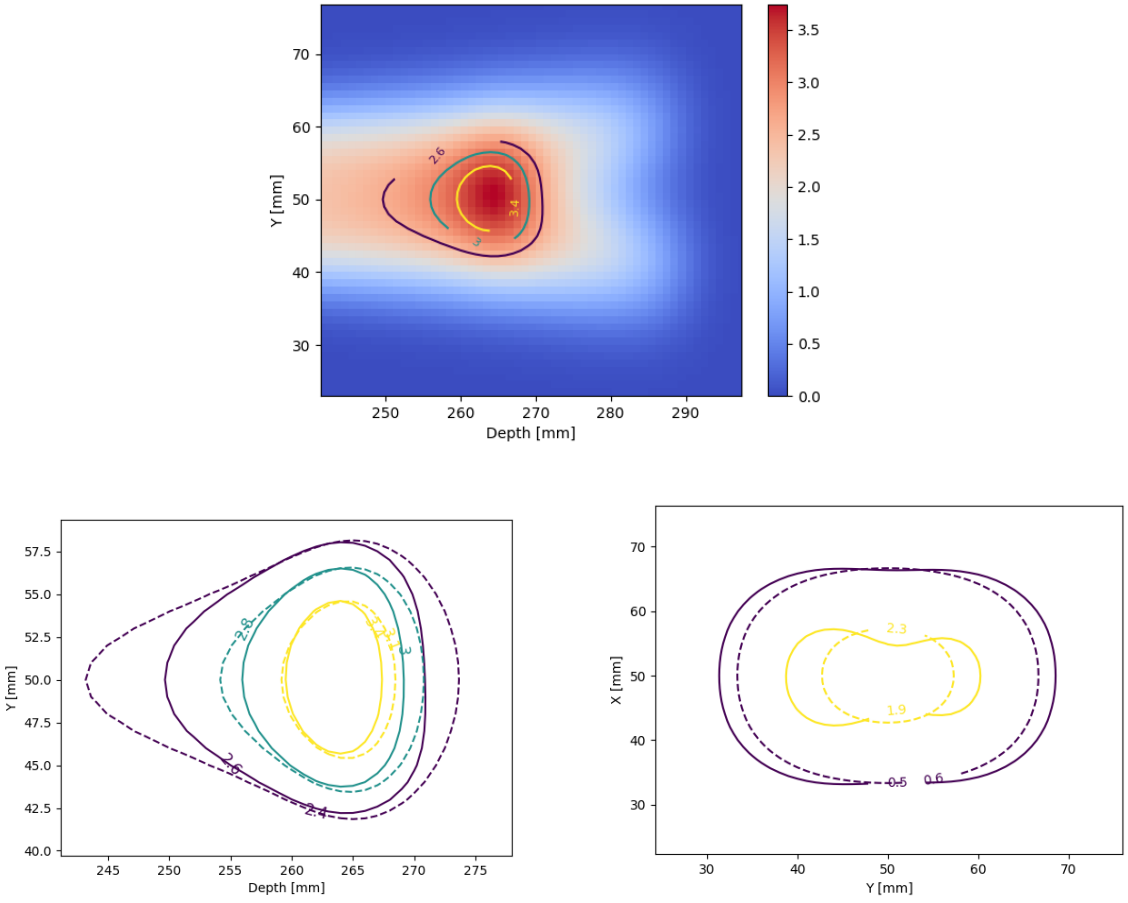

Figure 55: *Longitudinal relative dose profile (the upper part) and comparison of the contour plots of the dose (dashed= round and line= equivalence).*

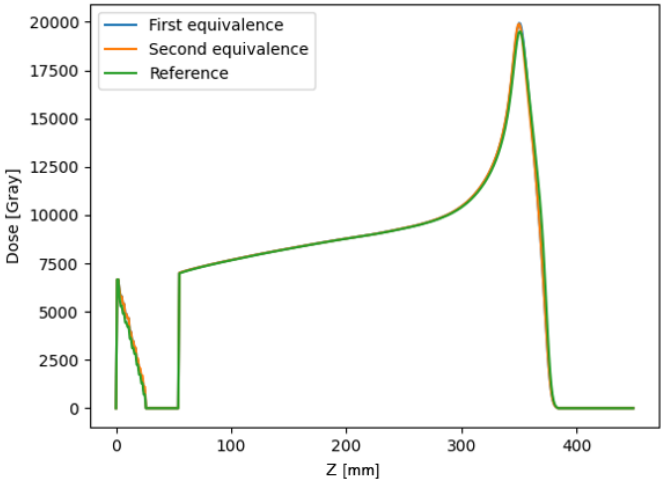

Figure 56: *IDDs of the 3 configurations with simplification.*

The integral dose profiles of the three shapes are shown in Figure 56. The IDD confirms that the fluence vs. elevation histogram is indeed identical in the different shapes. Moreover, the IDD curve is extremely similar with or without the simplification. The results found for the IDDs and the dose distribution of each shape corroborate that even if the histogram is identical, the geometric reorganization will change the spatial distribution of the dose.

In Table 3 the mean dose, the maximum dose, and the volume where at least 80% of the maximum dose is deposited (Volume $d80$) are presented and compared with the reference case. We observe that the reference shape has the smallest maximum dose but the highest mean dose and the more the shape is close to a perfect pyramidal shape the more the maximum dose increase. In contrast, the volume d80 has an opposite effect. These values suggest that a multiple pyramidal shape permits to give a higher mean dose but on a more spread area. This shows that the dose arrangement is not the only element that changes with the 3D range modulator.

In Figure 53 and Figure 55, it appears that even if the height of the obstacles are the same in each case, R70 is higher in the reference case than in the equivalences. This is easily explained by the type of shape. The reference shape has both high and low heights in the center. A part of the protons passing through these low heights have a straight trajectory and allow to define this distal shape.

	Maximum dose (Gy)	Mean dose (Gy)	Volume d80 (mm^3)
Multiple pyramidal shape (reference)	38.4	11.0	1396
Equivalence 1	40.6	10.92	1203
Difference relative to reference (%)	+5.73	- 0.73	- 13.8
Equivalence 2	40.8	10.88	1203
Difference relative to reference (%)	+6.25	-1.09	-13.8

Table 3: *Comparison between the first multiple pyramidal shape and the equivalences of the maximum dose (Gy), mean dose (mm) and the volume with a dose greater or equal to* 80% *of the maximum dose (Volume d80)*

7.1.2 1 pyramid vs. 3 pyramids

The second comparison studies the difference between three pyramids of same height placed side by side and one pyramid (see Figure 57) using the same property of comparison explain above. The height is 50 mm (D1= 55 and D2= 85 mm). The shape of the obstacle at the center in the xz plan is the same in both cases.

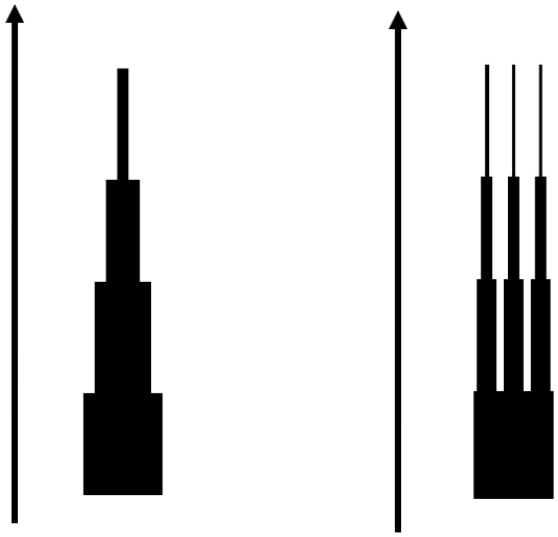

Figure 57: *2-D representation of the shape modulator for the reference case (on the right) and the single pyramidal shape equivalent (on the left)*

We see in Figure 58 and in Table 4 that the dose profile, the maximum dose and the range are similar in both cases. The main difference is in the volume of d80. This result is similar to what we observed for the first comparison in Section 7.1.1. The simple pyramid has the highest maximum dose and a lower d80 volume and the range is higher for the reference. More precisely, the IDD shows that three peaks are present in both cases (see Figure 59). However, the third peak is more concentrated and higher with the reference shape.

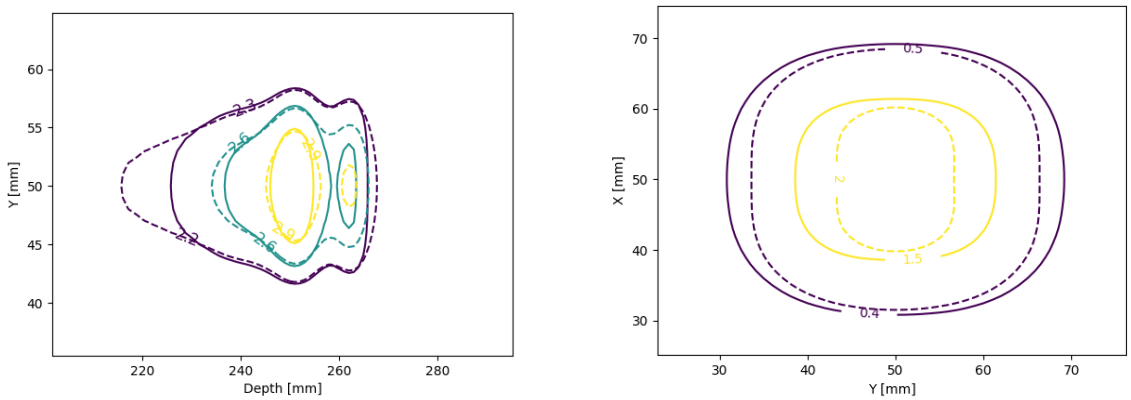

Figure 58: *Comparison on the dose profile in the YZ plan (on the left) and the XY plan (on the right) (dashed= round and line= equivalence).*

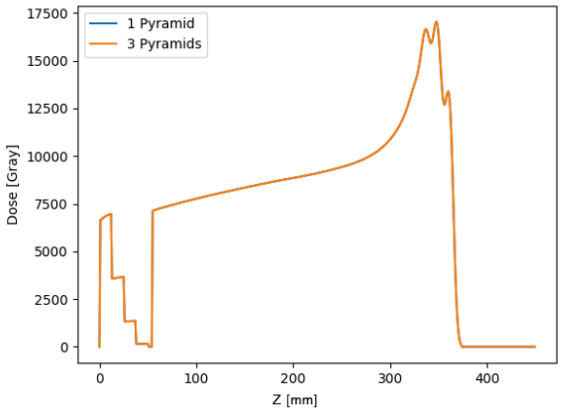

Figure 59: *IDD of the 3 Pyramids and the unique pyramid equivalence.*

	Maximum dose (Gy)	R80 (mm)	Volume d80 (mm^3)
Multiple pyramidal shape (reference)	33.71	266	2682
Unique pyramidal shape	33.92	264	1910
Difference relative to the reference (%)	+0.62	-0.75	-29

Table 4: *Comparison between the second multiple pyramidal shape and the equivalent pyramidal shape of the maximum dose (Gy), R80 (mm) and the volume with a dose greater or equal to* 80% *of the maximum dose (Volume d80)*

A last shape is analyzed. Three pyramids placed side by side with the central pyramid higher. The height of the object is 50 mm and the length of the base is 21 mm.

The Table 5 shows that putting pyramids of different heights reverse the effect of which obstacle gives the maximum dose, and which gives a higher d80 volume.

	Maximum dose (Gy)	R80 (mm)	Volume d80 (mm^3)
Multiple pyramidal shape (reference)	39.03	269	1799
Unique pyramidal shape	38.26	269	1892
Difference relative to the reference (%)	-1.97	+0	+3.5

Table 5: *Comparison between the third multiple pyramidal shape and the equivalent of pyramidal shape of the maximum dose (Gy), R80 (mm) and the volume with a dose greater or equal to* 80% *of the maximum dose (Volume d80)*

7.2 Effect of one pixel of the initial fluence

The simulations performed in this part aim to decompose and vizualise the effect of each part of the initial fluence in a known deposited dose. Then we will look at the impact of a one pixel initial fluence passing through a certain shape. The first simulation comes from Section 6.3 and all the others are of type 1.

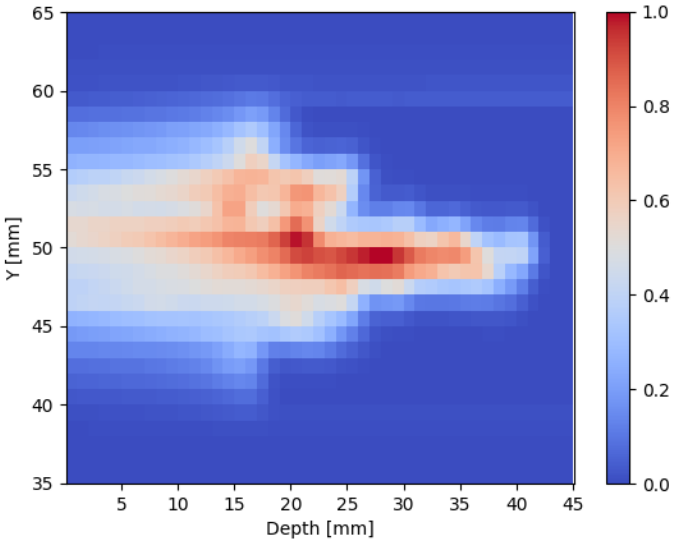

Figure 60: *Relative dose of 100 MeV beam with a Gaussian distribution.*

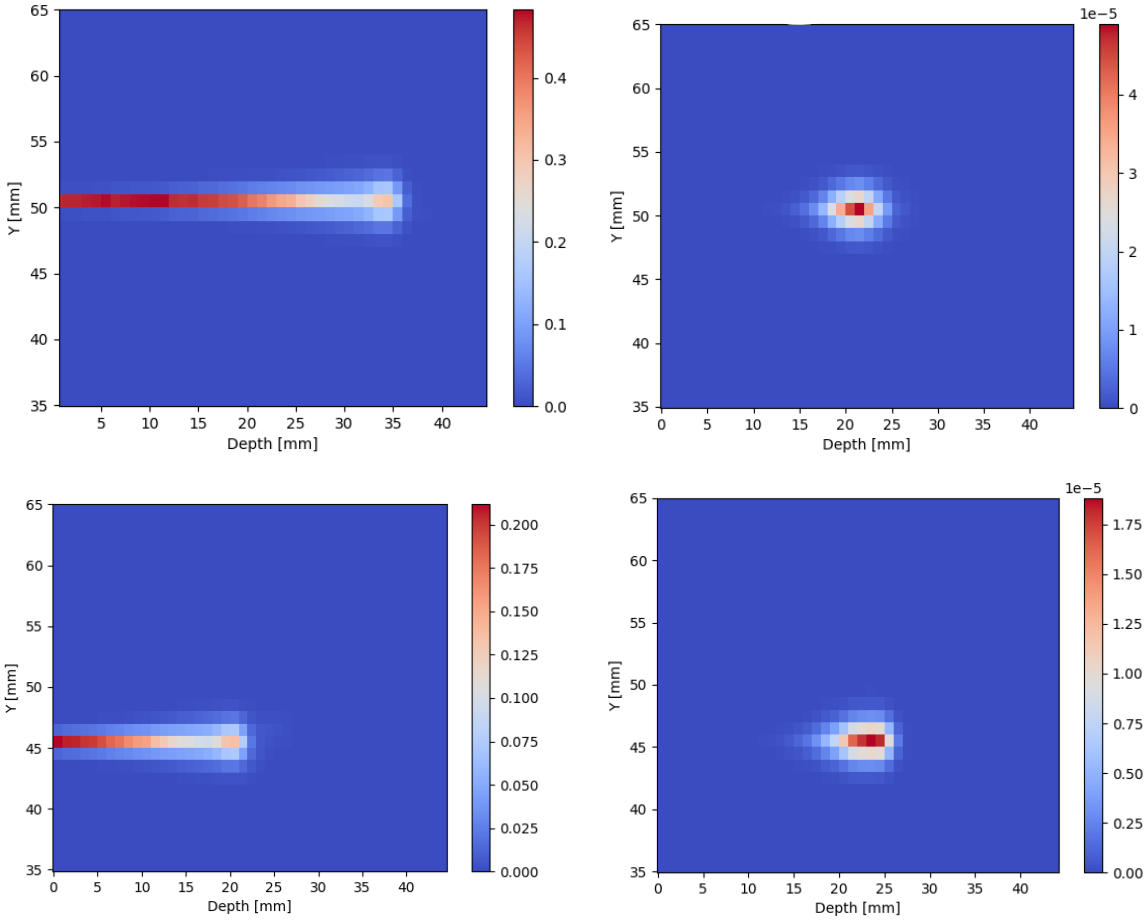

Figure 61: *Participation on the total dose (x=50 mm) of the protons respectively in point* [50,50], [45,50], [50,45] *and* [45,45].

Figure 60 shows the dose normalized to 1 at maximum dose found with the shape used in Section 6.3 and Figure 61 shows the participation of each part of the initial beam.

The same process can be done with a 3-D range modulator given in Figure 62. Figure 63 shows the dose

distribution and Figure 64 gives the participation of four point of the initial fluence on this dose. We notice that a distant point will have an impact especially at the end of its beam, while a close point contributes more at the beginning of the beam. This is explained by the scattering that will extend the impact of the beam in function of the depth. Moreover, the participation of a distant point alone does not have much influence on the dose to the center especially with a smaller energy where scattering is lower. The higher dose at the Bragg peak is not due to a single point of the initial fluence but rather the sum of all the points.

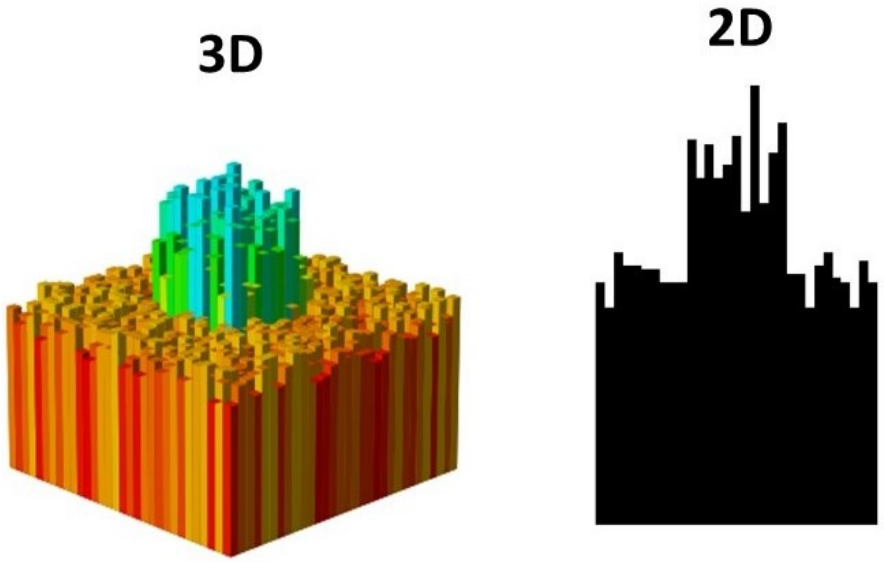

Figure 62: *3-D (on the left) and 2-D (on the right) representation of a 3-D range modulator of height 100 mm.*

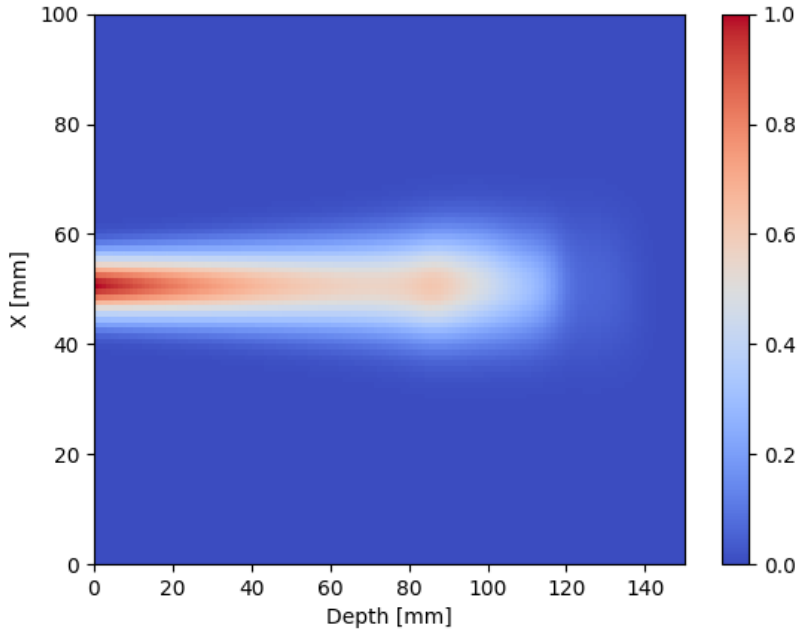

Figure 63: *Relative dose of 226 MeV beam with a Gaussian distribution with a standard deviation of 3 mm.*

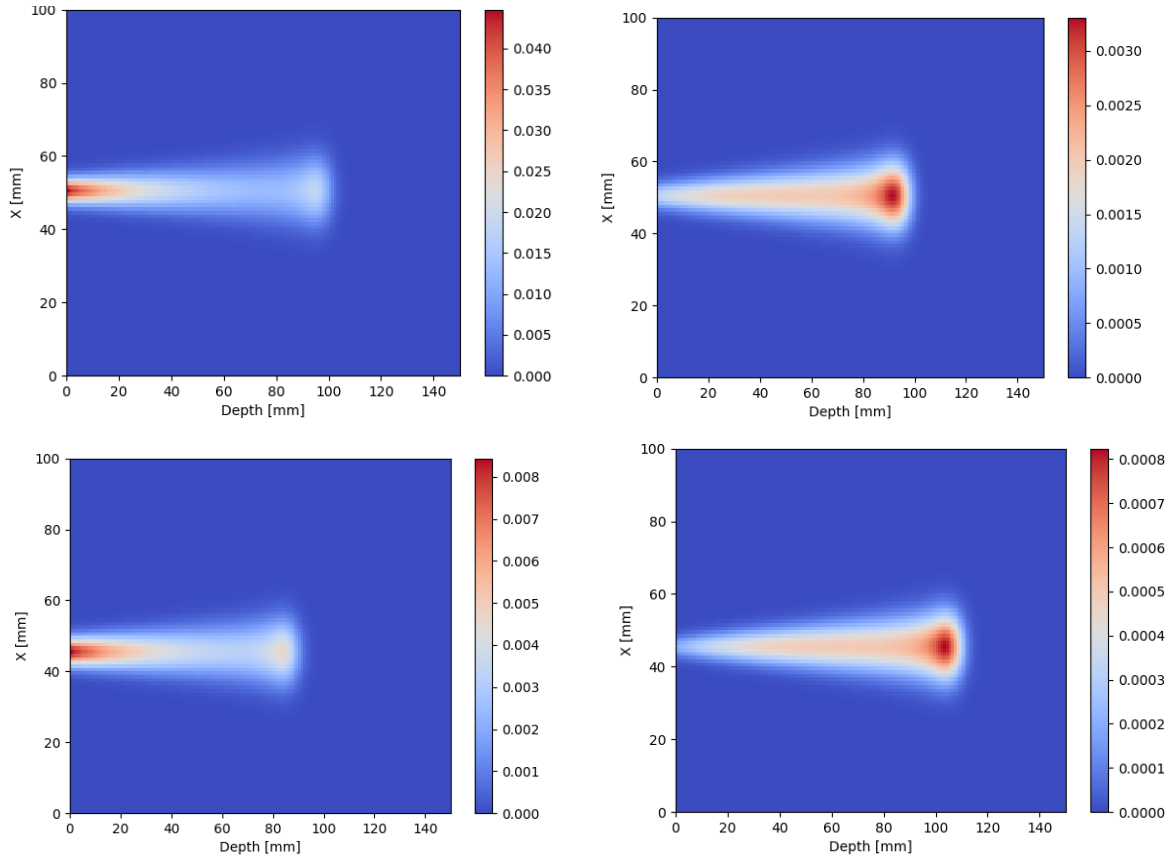

Figure 64: *Contribution on the total dose of the protons respectively in point* [50,50], [45,50], [50,45] *and* [45,45].

The second part look at the effect of a certain shape on the dose profile with a single point initial fluence. The dose is given in Gy/proton. If 10^{11} protons are thrown in one point, we simply multiply the dose by 10^{11} to find the deposited dose caused by these protons. Table 6 shows the maximum energy. It is positioned at the beginning of the water phantom because, since we are looking at the energy deposited by one point of the initial fluence, there is almost no dose summation created by scattering. Even if the energy loss is lower at the beginning, the total dose will be higher at the phantom entrance than at the Bragg Peak. The maximum energy appears when the obstacle is the smallest. Since the Bragg Peak with a beam of 226 MeV is positioned a little bit after 350 mm in the grid, the maximum energy after 350 mm gives the maximum value of the Bragg peak. The $Y80\%$ is the value of Y-axis where the deposited energy is 80% of the maximum energy in the transversal plot. We look at the Y 80% at a depth of 320 mm. The different shapes give the same $Y80\%$ and the maximum dose at the Bragg peak are more or less similar.

	Dmax (Gy)	Dmax after z=350 mm(Gy)	Y80% (mm)
Shape 1	$1.0674 * 10^{-8}$	$1.142 * 10^{-9}$	46-54
Shape 2	$1.0664 * 10^{-8}$	$1.140 * 10^{-9}$	46-54
Shape 3	$1.0669 * 10^{-8}$	$1.143 * 10^{-9}$	46-54
Shape 4	$1.0672 * 10^{-8}$	$1.142 * 10^{-9}$	46-54

Table 6: *Summary of the maximum dose (Dmax), The maximum dose deposited after 350 mm and Y 80%. Shape 1 is a single peak of* $1mm^2$ *with a height of 50 mm. The shapes 2,3 and 4 have the same central peak from shape 1 surrounded by a square with a length of* $21mm$ *and a height of respectively* 60,50 *and* 40 mm.

Now, we modify one element from the 3D range modulator of Shape 4 to observe the effect on the dose depending on the distance of the modification (see Table 7). It appears that with more than 3mm the change becomes negligible.

Distance	Dmax (Gy)	Dmax after z=350 (Gy)	Y80% (mm)
1 mm	1.067210^{-8}	$1.1423 * 10^{-9}$	46-54
Difference relative to the reference (%)			
2 mm	$1.0673 * 10^{-8}$	$1.1423 * 10^{-9}$	46-54
Difference relative to the reference (%)			
3 mm	$1.0673 * 10^{-8}$	$1.143 * 10^{-9}$	46-54
Difference relative to the reference (%)			

Table 7: *Comparison with Shape 4 of Dmax, Dmax after depth of 350 mm and Y80% by adding a height of 5 to one point at a distance of 1,2 and 3 mm from the center.*

Now in order to see if the effects except the range are different with other heights, we look at effects created by similar shapes as in the first scenario but with smaller heights (see Table 8). As expected, the maximum energy changes and becomes larger when the range modulator is small. However, the maximum energy after 350 mm and Y80%, remains similar.

	Dmax (Gy)	Dmax after z=350 (Gy)	Y80% (mm)
shape 5	$1.254 * 10^{-8}$	$1.14 * 10^{-9}$	46-54
shape 6	$1.2532 * 10^{-8}$	$1.143 * 10^{-9}$	46-54
shape 7	$1.2536 * 10^{-8}$	$1.14 * 10^{-9}$	46-54
shape 8	$1.2543 * 10^{-8}$	$1.142 * 10^{-9}$	46-54

Table 8: *Summary of the maximum dose (Dmax), the maximum dose after 350 mm and Y 80%. Shape 5 is a single peak of* $1mm^2$ *with a height of 45 mm. The shapes 6,7 and 8 are same peak from shape 5 surrounded by a square with a length of* $21mm$ *and a height of respectively* $65,55$ *and* $45 \quad mm$.

These elements allow us to have a first idea of the impact that each part of the beam on different hegdehog can have on the final dose distribution.

8

Discussion and conclusion

FLASH proton therapy allows better preservation of healthy tissue and is therefore a highly promising treatment against cancer. However, the use of FLASH requires the creation of a custom-made range modulator depending on the patient and his tumor. Existing tools are either too slow or too inaccurate. This study aims to create an analytical tool to model the path of a beam with any initial fluence (Gaussian, uniform or arbitrary) and to be able to isolate the effect of each part of the initial fluence on the dose distribution.

The developed model is not intended to be used in an optimization but rather to give a first indication of the impact of the hedgehog. The results of Section 6 show that the simulations are consistent after a comparison with MCsquare but the difference is too important to be used in a clinical setting. Such a difference is also observed when an homogeneous case is used. In the case of the 226 MeV beam the behavior before the peak differs from MCsquare. However, as the lung-bone simulation shows, the results proposed by our model are consistent with the expected results. More precisely, the comparison in the bone lung scenario in Figure 23 shows a relative error up to 2.6% after the peak in the simplified case or not. In more complex cases in Section 6.3, we note that the differences can go up to 25% which is too large for a clinical study, but the peak locations remain more or less similar as well as the overall behavior which allows us to give a first approximation of the expected result.

However, the goal of this simulation was never to find such an accuracy. Indeed, the model developed in this study permits to obtain in an acceptable time a vizualization of the individual impact of each element constituting a hedgehog and as such better understand the advantages and disadvantages of each possible configuration. It is possible to quickly vizualize and analyze the modification of the 3D range modulator or the initial beam.

This is corroborated in our Section 7. In this section we wanted to study the impact of the geometric characteristics of a 3D range modulator on the dose distribution. In a first step, we compared the dose generated by single and multiple pyramidal shapes with the same fluence characteristics (Section 7.1). In a second step, we vizualized more precisely the effect of a point of the initial fluence and the impact of range modulator (Section 7.2).

The results of Section 7.1 show that the geometrical arrangement of the peaks must be considered. Depending on whether a circular or pyramidal structure was used, differences in the dose distribution were observed. For example, a difference of up to 6.25% was observed between the maximum dose of the round shape and of its pyramidal equivalents. However, their integral dose being the same in all configurations, it allows us to analyze the impact on the 3D spatial distribution and not only to look at the Bragg peak. It has indeed been observed that the difference is mainly after such peak.

We also noted on Table 4 that even several similar shapes give different results. However, the purpose of this simulation is to find a shape close to the one needed and to reject the ones which are not appropriate. However, the differences between the two similar shapes are small compared to the accuracy of our method, so it does not necessarily mean that one shape is better than the other. This tool is more useful to analyze the type of shape to use. A pyramid or a round shape will not have the same behavior.

Section 7.2 allows us to vizualize more precisely the effect of each element of the hedgehog. This helps us to understand how each part of the range modulator and the beam participates more precisely in the realization of a spread-out Bragg peak. The results of Section 7.2 show us that, for a 1x1 mm part of the beam, a hedgehog with a 7x7 mm base is sufficient to analyze its effect. Indeed, due to the small scattering at the beginning of the beam looking further away has only a very small effect which is negligible. This leads to the idea of storing these hedgehog parts and creating a dictionary. The principle would be to store a maximum of dose profiles and their specific spike. Then, starting from a desired target dose, decompose it and create from the dictionary a custom 3D range modulator.

Another perspective brought by this algorithm can be illustrated by Figure 65. To illustrate this point, let's assume that we have a hedgehog that allows us to have a SOBP. However, a single hedgehog does not allow to have a laterally uniform dose. Therefore, we will use more than one hedgehog with several beamlets. In this case we used two beamlets for the illustration (see Figure 65). Depending on the distance between the beamlets we get a more or less uniform dose laterally. But the scattering is more important towards the end of the SOBP, the dose uniformity is not as good in all z. The proposed method allows to quickly evaluate this and to correct it by adding additional hedgehog and beamlets to bring back the dose where it is needed. All this could be part of an optimization method that goes beyond the objectives defined for this work.

However, one key factor has not been studied so far. This is the impact of the spatial resolution (the pixel spacing of the hedgehog elevation map). In this master thesis, we only considered an isotropic resolution of 1x1x1 mm. This resolution was initially chosen for a validation with MCsquare which works with a voxelized geometry. Nevertheless, it is also possible to use our algorithm with different spatial resolutions. This can be interesting for example for Section 6.3 where the 1mm precision did not allow to create a hedgehog allowing to simulate a SOBP. However, greater accuracy means bigger memory and slower execution time. Nevertheless, it is still possible to optimize the code and memory for this. The interesting elements to keep in the memory are not at the beginning of the beam but at the end. Moreover, we know that the distribution at each depth depends only on the one before and not the rest.

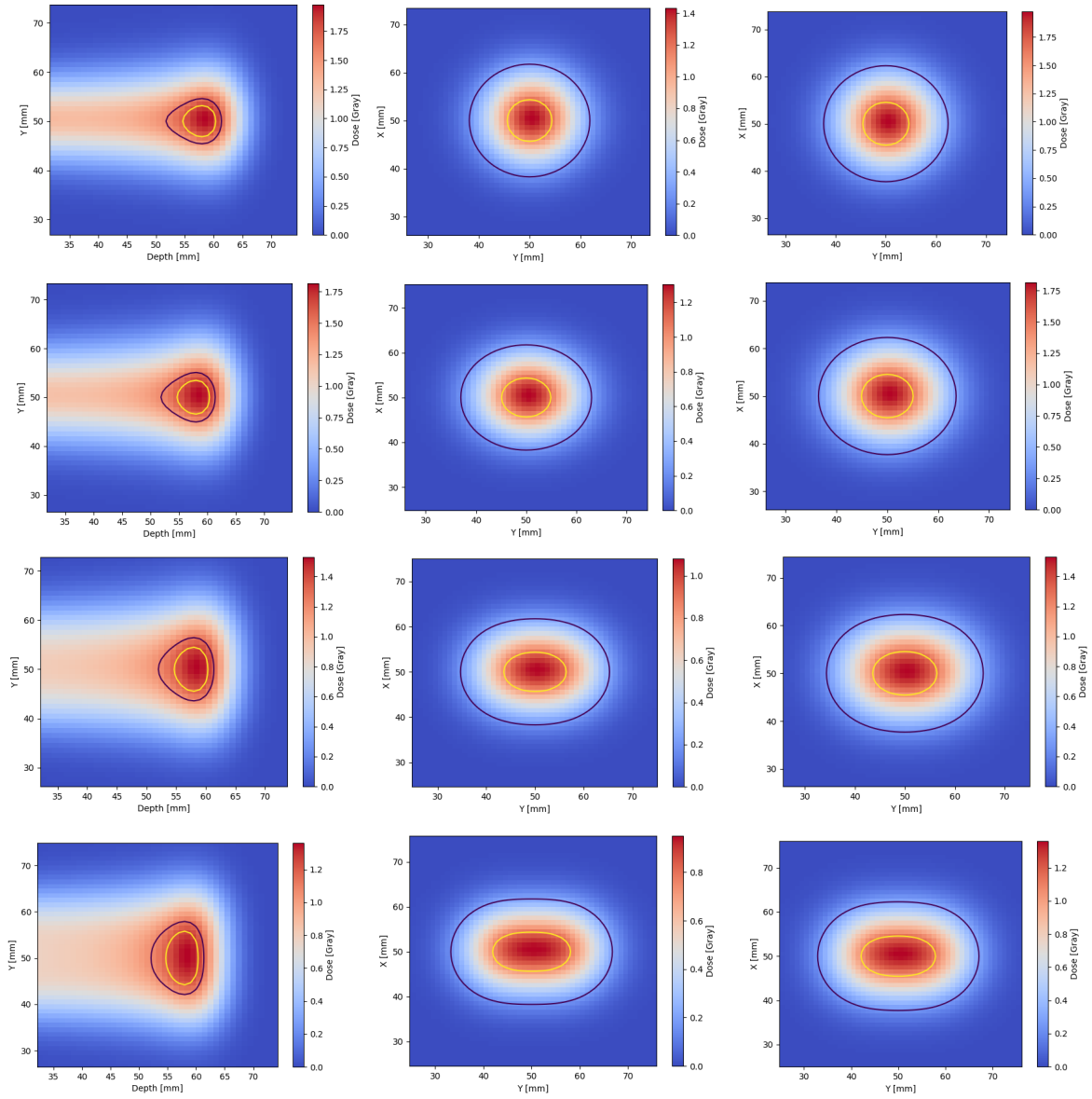

Figure 65: *Dose profile of 2 Gaussian distribution without any obstacle and transversal dose at depth 268 and 278mm. The distances between the beam are respectively 2,6,10 and 12 mm.*

It is noteworthy that even if the model is not accurate enough to be used in the precise optimization of a range modulator, its analytical nature, which makes it faster than Monte Carlo methods, could make it useful in determining an initial guess for a more accurate optimization algorithm. In other words, we believe that this model could be potentially developed to be use as a quicker tool which would eliminate many possibilities by finding a shape more or less close to the required custom shape.

Another perspective for this model is the possibility to determine the position of the spots in proton beam scanning to cover the whole target volume. The model is not accurate enough to predict the dose correctly but it can be useful in a pre-optimisation to get a first guess of where to place the spots.

Further research on this subject could lead to a level of accuracy which could allow an advancement in the research on the use of FLASH proton therapy.

References

[1] Avid Khamenehfar. *Reversal of Multidrug Resistance Fluorescently Measured in Single Cancer Cells Captured in the Microfluidic Chip*. PhD thesis, 08 2015.

[2] Ben Milborne, Abul Arafat, Rob Layfield, Alexander Thompson, and Ifty Ahmed. The use of biomaterials in internal radiation therapy. *Recent Progress in Materials*, 2:1–34, 05 2020.

[3] Gillian Barnett, Catharine West, Alison Dunning, Rebecca Elliott, Charlotte Coles, Paul Pharoah, and Neil Burnet. Normal tissue reactions to radiotherapy: Towards tailoring treatment dose by genotype. *Nature reviews. Cancer*, 9:134–42, 02 2009.

[4] Bora Tas. *Advanced Radiation Treatment Planning of Prostate Cancer*. 09 2018.

[5] Hui Liu and Joe Chang. Proton therapy in clinical practice. *Chinese journal of cancer*, 30:315–26, 05 2011.

[6] Alfred R Smith. Proton therapy. *Physics in Medicine and Biology*, 51(13):R491–R504, jun 2006.

[7] Glennda Chui. The power of proton therapy. https://www.symmetrymagazine.org/article/december-2008/the-power-of-proton-therapy, 2008.

[8] Kevin Souris. *Accurate assessment of proton therapy treatments: fast Monte Carlo dose engine and extensive robustness tests*. PhD thesis, Université Catholique de Louvain, 2017.

[9] Yuri Simeonov, Uli Weber, Petar Penchev, Toke Ringbæk, Christoph Schuy, Stephan Brons, Rita Engenhart-Cabillic, Jens Bliedtner, and Klemens Zink. 3d range-modulator for scanned particle therapy: Development, monte carlo simulations and experimental evaluation. *Physics in Medicine and Biology*, 62, 07 2017.

[10] Wayne Newhauser and Rui Zhang. The physics of proton therapy. *Physics in medicine and biology*, 60:R155–R209, 03 2015.

[11] John Lee, Guillaume Janssens, and Edmond Sterpin. Engineering issues in proton therapy, 2022.

[12] Frank Watt, Mark Breese, Andrew Bettiol, and Jeroen van Kan. Proton beam writing. mater today. *Materials Today*, 10:20–29, 06 2007.

[13] Harald Paganetti. Range uncertainties in proton therapy and the role of monte carlo simulations. *Physics in medicine and biology*, 57:R99–117, 05 2012.

[14] Reza Bagheri, Alireza Khorrami, Bakhtiar Azadbakht, Mahmoud Akbari, and Seyed Shirmardi. Determination of water equivalent ratio for some dosimetric materials in proton therapy using mncpx simulation tool. *Nuclear Science and Techniques*, 30, 02 2019.

[15] Normal distribution. https://en.wikipedia.org/wiki/Normal_distribution.

[16] pstar. https://www.physics.nist.gov/PhysRefData/Star/Text/programs.html.

[17] Kent Wong, Bela Erdelyi, Reinhard Schulte, Vladimir Bashkirov, George Coutrakon, Hartmut Sadrozinski, Scott Penfold, and Anatoly Rosenfeld. The effect of tissue inhomogeneities on the accuracy of proton path reconstruction for proton computed tomography. *AIP Conference Proceedings*, 1099, 03 2009.

[18] Multidimensional image processsing (scipy.ndimage), author=, year=, howpublished =https://scipy.github.io/devdocs/tutorial/ndimage.html.

[19] Priyatharshini Venkatakrishnan, Govardhan Kumar, and Bhavana Sampadarao. Study of the various cutaneous adverse reactions to radiotherapy. *International Journal of Research in Dermatology*, 7:250, 02 2021.

[20] Heike Thomas and Beate Timmermann. Paediatric proton therapy. *The British Journal of Radiology*, 93:20190601, 09 2019.

[21] Haibo Lin, Chengyu Shi, Sheng Huang, Jiajian Shen, M. Kang, Qing Chen, Huifang Zhai, James Mcdonough, Zelig Tochner, Curtiland Deville, Charles Simone, and Stefan Both. Applications of various range shifters for proton pencil beam scanning radiotherapy. *Radiation Oncology*, 16, 08 2021.

[22] Guangming Zhou. Mechanisms underlying flash radiotherapy, a novel way to enlarge the differential responses to ionizing radiation between normal and tumor tissues. *Radiation Medicine and Protection*, 1, 03 2020.

[23] Jonathan Hughes and Jason Parsons. Flash radiotherapy: Current knowledge and future insights using proton-beam therapy. *International journal of molecular sciences*, 21, 09 2020.

[24] Marie-Catherine Vozenin, Pauline Fornel, Kristoffer Petersson, Vincent Favaudon, Maud Jaccard, Jean-François Germond, B. Petit, Marco Burki, Gisèle Ferrand, David Patin, Hanan Bouchaab, Esatmahmut Ozsahin, François Bochud, Claude Bailat, Patrick Devauchelle, and Jean Bourhis. The advantage of flash radiotherapy confirmed in mini-pig and cat-cancer patients. *Clinical Cancer Research*, 25:clincanres.3375.2017, 06 2018.

[25] Simon Jolly, Hywel Owen, Marco Schippers, and Carsten Welsch. Technical challenges for flash proton therapy. *Physica Medica*, 78:71–82, 09 2020.

[26] Frank Verhaegen, Roel-Germ Wanders, Cecile Wolfs, and Danielle Eekers. Considerations for shoot-through flash proton therapy. *Physics in Medicine Biology*, 66, 02 2021.

[27] Cancer. https://www.who.int/news-room/fact-sheets/detail/cancer#:~:text=Cancer%20is%20a%20leading%20cause,and%20rectum%20and%20prostate%20cancers., 2022.

[28] Manuel Arruebo, Nuria Vilaboa, Saez Berta, Julio Lambea, Alejandro Tres, Mónica Valladares, and Africa González-Fernández. Assessment of the evolution of cancer treatment therapies. *Cancers*, 3:3279–330, 12 2011.

[29] Jéssica Mestre Correia. *Dosimetrical studies for error acceptance in FLASH proton therapy*. PhD thesis, Instituto politéchnico de Lisboa, 2022.

[30] Michael Goitein and Dan Jones. *Radiation Oncology: A Physicist's-Eye View*, volume 61. 12 2008.

[31] Donald J.and Ehsan Samei. How to understand and communicate radiation risk. https://www.imagewisely.org/Imaging-Modalities/Computed-Tomography/How-to-Understand-and-Communicate-Radiation-Risk, 2017.

[32] Harald Paganetti. *Proton Therapy Physics*. 12 2011.

[33] How to build a proton therapy center? https://www.iba-worldwide.com/sites/protontherapy/files/media_document/iba_pt_brochure_proteusplus_business_model_en.pdf.

[34] Module 3: Equipment for proton therapy delivery. https://www.oncolink.org/print/pdf/5983?print_5983.pdf.

[35] Valérie De Smet. *Neutron measurements in a proton therapy facility and comparison with Monte Carlo shielding simulations*. PhD thesis, 09 2016.

[36] B. Marchand, Damien Prieels, B. Bauvir, Chemin Cyclotron, Rodolphe Sepulchre, and M. Gérard. Iba proton pencil beam scanning: An innovative solution for cancer treatment. *Proc. 7th EPAC (Vienna)*, 01 2000.

[37] Andrew Wroe, A Ghebremedhin, I Gordon, Reinhard Schulte, and J Slater. Water equivalent thickness analysis of immobilization devices for clinical implementation in proton therapy. *Technology in cancer research treatment*, 13, 08 2013.

[38] Erik Tryggestad, Wei Liu, Mark Pepin, Christopher Hallemeier, and Terence Sio. Managing treatment-related uncertainties in proton beam radiotherapy for gastrointestinal cancers. *Journal of Gastrointestinal Oncology*, 11:212–224, 02 2020.

[39] M. Kang, Shouyi Wei, Jehee Choi, Haibo Lin, and Charles Simone. A universal range shifter and range compensator can enable proton pencil beam scanning single-energy bragg peak flash-rt treatment using current commercially available proton systems. *International Journal of Radiation Oncology*Biology*Physics*, 113, 01 2022.

[40] Bernard Gottschalk. Radiotherapy proton interactions in matter. 03 2018.

[41] Marie Backman et al. Effects of nuclear and electronic stopping power on ion irradiation of silicon-based compounds. 2012.

[42] L.D. LANDAU and E.M. LIFSHITZ. Chapter xviii - inelastic collisions. In L.D. LANDAU and E.M. LIFSHITZ, editors, *Quantum Mechanics (Third Edition)*, pages 591–646. Pergamon, third edition edition, 1977.

[43] David Grimes, Daniel Warren, and Mike Partridge. An approximate analytical solution of the bethe equation for charged particles in the radiotherapeutic energy range. *Scientific Reports*, 7, 12 2017.

[44] Abigail Besemer, Harald Paganetti, and Bryan Bednarz. The clinical impact of uncertainties in the mean excitation energy of human tissues during proton therapy. *Physics in medicine and biology*, 58:887–902, 01 2013.

[45] Jessica Mestre Correia. Dosimetrical studies for error acceptance in flash proton therapy. Master's thesis, Instituto politémico de lisboa, 1 2022.

[46] Eric Shinohara MD. Module 2: The physics of proton therapy. https://www.oncolink.org/healthcare-professionals/oncolink-university/proton-therapy-professional-education/oncolink-proton-education-modules/module-2-the-physics-of-proton-therapy, 2016.

[47] Multiple scattering. https://gray.mgh.harvard.edu/attachments/article/337/Techniques%20of%20Proton%20Radiotherapy%20(06)%20Multiple%20Scattering.pdf.

[48] Rui Zhang and Wayne Newhauser. Calculation of water equivalent thickness of materials of arbitrary density, elemental composition and thickness in proton beam irradiation. *Physics in medicine and biology*, 54:1383–95, 03 2009.

[49] Linda Hong, Michael Goitein, Marta Bucciolini, Robert Comiskey, Bernard Gottschalk, Skip Rosenthal, Chris Serago, and Marcia Urie. *A pencil beam algorithm for proton dose calculations*, volume 41. IOP Publishing, aug 1996.

[50] Martin Soukup, Matthias Fippel, and Markus Alber. A pencil beam algorithm for intensity modulated proton therapy derived from monte carlo simulations. *Physics in medicine and biology*, 50:5089–104, 12 2005.

[51] Erik Almhagen. Development and validation of a scanned proton beam model for dose distribution verification using monte carlo. 2015.

[52] Radhe Mohan and David Grosshans. Proton therapy – present and future. *Advanced Drug Delivery Reviews*, 109, 12 2016.

[53] Jiajian Shen, Wei Liu, Aman Anand, Joshua Stoker, Xiaoning Ding, Mirek Fatyga, Michael Herman, and Martin Bues. Impact of range shifter material on proton pencil beam spot characteristics. *Medical physics*, 42:1335, 03 2015.

[54] Bryan Bednarz. Monte carlo methods in proton therapy. https://www.ptcog.ch/archive/conference_p&t&v/PTCOG49/presentationsEW/18-2-3_MC.pdf.

A

Appendix A: Code

```
"""
Created on Mon Oct 18 09:55:16 2021

@author: Elisa Devresse
"""
from matplotlib.pyplot import gray
import numpy as np
import matplotlib.pylab as plt
from PIL import Image, ImageDraw
from scipy import ndimage
from scipy import interpolate
import scipy.io
import matplotlib.cm as cm
from scipy.ndimage import gaussian_filter

#Function which reads the stopping power file
def read_stopping_power(fileName) :
    with open(fileName) as f :
        stopping_power_Kinetic_energy = np.array(list(list(float(w) for w in i.split())
    for i in f))
        Kinetic_energy = stopping_power_Kinetic_energy[:,0]
        stopping_power_water = stopping_power_Kinetic_energy[:,1]*density_water/10 # MeV/
    mm
    return [Kinetic_energy,stopping_power_water]

# Gives the fluence distribution of the spot in the spot plane in the spot coordonate
    system(x,y)
def F(x,y,sigma_z,x0,y0):
    return(2*np.pi*sigma_z*sigma_z)**(-1)*np.exp(-(x-x0)**2/(2*sigma_z**2)-(y-y0)**2/(2*
    sigma_z**2))

#Gives the 2D Gaussian on each slice z
def mesh_2D(sigma_z,len_x,len_y,x0,y0):
    mesh2D=np.zeros((len_x,len_y))
    for i in range(len_x):
        for j in range(len_y):
            mesh2D[i][j]=F(i,j,sigma_z[i][j],x0,y0)
    return mesh2D


#interpolation to have continuous lost energy
def interpolation(x,y,value):
    f=interpolate.interp1d(x,y, fill_value="extrapolate")
    return f(value)
```

```
41
42
43
44 #Main function which compute the dose
45 #the length_matrix and length_matrix_z can be change depending on the initial energy E0
46 # The file for the stopping power and scattering must be added and depend also on the
       initial energy
47 # the initial fluence distribution can be chosen between: "Gaussian", "Continue","point"
       and other types can be easily added.
48 def dose(length_matrix,length_matrix_z,E0,file_stopping_power,file_scattering_sigmas,
       is_in_tetra,fluence_type):
49
50   #Position of the range modulator
51   center_tetrahedron_x=50
52   center_tetrahedron_y=50
53   height_tetrahedron=50
54   start_tetrahedron_z=1
55
56
57   #Placement of the water cube or the dose must be uniform
58   start_water_x=10
59   end_water_x=90
60   start_water_y=10
61   end_water_y=90
62   start_water_z=55
63   end_water_z=450
64
65
66   #Position of the nozzle
67   noozle_x=50
68   nozzle_y=50
69
70
71   mass_stopping_power_air =0 # We consider that the air is like the void
72
73
74   #in_water=true use water bac otherwise use the range modulator.
75   # Beware the tray is bigger than the beam.
76   in_water=False
77
78   #Definition of matrices to compute the fluence and dose
79   fluence_3D=np.zeros((length_matrix,length_matrix,length_matrix_z))
80   Dose=np.zeros((length_matrix,length_matrix,length_matrix_z))
81   fluence_per_energy_3D=np.zeros((length_matrix,length_matrix,end_water_z-start_water_z
       +1,height_tetrahedron+1))
82   Kinetic_energy,stopping_power_water=read_stopping_power(file_stopping_power)
83   new_sigma_z=np.ones((length_matrix,length_matrix))*3
84   in_water_since_energy_level=np.arange(0,height_tetrahedron+1,1)
85
86
87   ########We initialize the initial fluence#########
```

```
88
89  if fluence_type=="Gaussian":
90      fluence_3D[:,:,0]=mesh_2D(new_sigma_z,length_matrix,length_matrix,noozle_x,nozzle_y
      )*0.4*10**9
91
92
93  ##If we want to look at only one pixel of fluence
94  elif fluence_type== "One point":
95      fluence_3D[:,:,0]=np.zeros((length_matrix,length_matrix))
96      fluence_3D[50,50,0]=mesh_2D(new_sigma_z,length_matrix,length_matrix,noozle_x,
      nozzle_y)[50,48]*0.4*10**9
97
98  #If we wanted a fluence continue
99  elif fluence_type== "Continue":
100     fluence_3D[:,:,0]=np.zeros((length_matrix,length_matrix))
101     fluence_3D[40:61,40:61,0]=np.ones((21,21))*10**11/(21*21)
102
103 #Energy in the different levels
104 E=np.zeros(length_matrix_z)
105 E[0]=E0
106
107
108 #keep in mind the new normal due to the obstacles because not the same energy
109 new_fluence_3D=np.zeros((length_matrix,length_matrix,length_matrix_z))
110 not_in_block=np.ones((length_matrix,length_matrix,length_matrix_z))
111 Energy_loss= np.zeros(length_matrix_z)
112 new_fluence_3D[:,:,0]=fluence_3D[:,:,0]
113
114
115 #use in the water phantom
116 E_bis=np.ones((length_matrix_z,length_matrix_z))*E0
117 Energy_loss_bis=np.zeros(length_matrix_z)
118
119
120
121
122 #We go through the "room" step by step
123 for z in range(1,length_matrix_z):
124
125      # If we are no longer in the tetrahedron
126      if in_water==True:
127    #If we are in the final bac of water
128    if z>=start_water_z and z<=end_water_z:
129
130       #we computer the not_in_block matrix which is a binary matrix
131       for x in range(length_matrix):
132           for y in range(length_matrix):
133               if start_water_y<=y<=end_water_y and start_water_x<=x<=end_water_x:
134                   in_blockb=1
135               else:
136                   in_blockb=0
```

```
137                 not_in_block[x,y,z]=(in_blockb-1)*(-1)
138 
139 
140         #here you have to convolve all the normals created by the pyramid
141         for a in range(0,height_tetrahedron+1):
142 
143             #we look if we are at the begining of the bac because we have to create the
    level of energy
144             # We take the part that is in the tetrahedron in a but not in a+1
145             if z==start_water_z:
146 
147                 #We look if the sigma of this level of energy is greater than 0 for the
    convolution
148                 if float(file_scattering_sigmas[in_water_since_energy_level[a]])>0:
149 
150                 #Check for initial energy because at this moment in_water_since=0
151                     if a==0:
152                         in_water_since_energy_level[a]=0
153                         #we look at the part of the beam that did not cross the
    tetrahedron at all
154                     fluence_per_energy_3D[:,:,z-start_water_z,a]= ndimage.gaussian_filter
    (fluence_per_energy_2D[:,:,a]*(not_in_block[:,:,start_tetrahedron_z+a])*(-
    not_in_block[:,:,z]+np.ones((length_matrix,length_matrix))),float(
    file_scattering_sigmas[in_water_since_energy_level[a]]),mode='constant',truncate=6)
155 
156                 #if the sigma is equal to 0 we don't do convolution we just take the part
     of the beam that goes through the bin
157                 else:
158                     fluence_per_energy_3D[:,:,z-start_water_z,a]=fluence_per_energy_2D
    [:,:,a]*((not_in_block[:,:,a+start_tetrahedron_z])*(-not_in_block[:,:,z]+np.ones((
    length_matrix,length_matrix))))
159 
160             #For the rest of the bac we just look at each level of energy at z-1
161             else:
162                 if float(file_scattering_sigmas[in_water_since_energy_level[a]])>0:
163                     fluence_per_energy_3D[:,:,z-start_water_z,a]= ndimage.gaussian_filter
    (fluence_per_energy_3D[:,:,z-start_water_z-1,a]*(-not_in_block[:,:,z]+np.ones((
    length_matrix,length_matrix))),float(file_scattering_sigmas[
    in_water_since_energy_level[a]]),mode='constant',truncate=6)
164                 else :
165                     fluence_per_energy_3D[:,:,z-start_water_z,a]=fluence_per_energy_3D
    [:,:,z-start_water_z-1,a]*(-not_in_block[:,:,z]+np.ones((length_matrix,length_matrix)
    ))
166 
167             #each level of energy increase of one
168             in_water_since_energy_level[a]+=1
169 
170 
171         #we sum all the protons on a square to get the total fluence on that square
172         if float(file_scattering_sigmas[in_water_since])>0:
173             for x in range(length_matrix):
```

```
174                 for y in range(length_matrix):
175                     fluence_3D[x,y,z]=fluence_3D[x,y,z-1]*not_in_block[x,y,z]+ sum(
    fluence_per_energy_3D[x,y,z-start_water_z,:])
176
177
178         else:
179             fluence_3D[:,:,z]=fluence_3D[:,:,z-1]
180
181         in_water_since+=1
182         in_water_since_bis+=1
183
184         E_bis[start_water_z-1,start_tetrahedron_z:start_tetrahedron_z+height_tetrahedron
    +1]=E[start_tetrahedron_z-1:start_tetrahedron_z+height_tetrahedron]
185
186         #on regarde la perte d' nergie  a chaque niveau
187         for a in range(start_tetrahedron_z,start_tetrahedron_z+height_tetrahedron+1):
188
189             Energy_loss_bis[a]=interpolation(Kinetic_energy,stopping_power_water,E_bis[z
    -1,a])
190             E_bis[z,a]=E_bis[z-1,a]-Energy_loss_bis[a]
191
192             if E_bis[z,a]<=0:
193
194                 E_bis[z,a]=0
195                 Energy_loss_bis[a]=0
196
197
198             #We sum up all the absorbed doses due to the different energies
199             Dose[:,:,z]+=(fluence_per_energy_3D[:,:,z-start_water_z,a-start_tetrahedron_z
    ]*Energy_loss_bis[a]*(-not_in_block[:,:,z]+np.ones((length_matrix,length_matrix))))
    *1.60217733*10**-13*10**6
200
201      #We are not in the water nothing to change
202      else:
203         fluence_3D[:,:,z]= fluence_3D[:,:,z-1]
204         E[z]=E[z-1]
205         Energy_loss[z]=0
206
207       #We are before in the tetrahedron
208        else:
209      #condition do not put a water block in 0
210
211
212      if start_tetrahedron_z<=z<start_tetrahedron_z+height_tetrahedron:
213          element_in_obstacle=np.zeros((length_matrix,length_matrix))
214
215         #Binary matrix to see if we are in the tetrahedron or not
216          for x in range(length_matrix):
217              for y in range(length_matrix):
218                  in_block=Is_in_tetra[x,y,z]
219                  element_in_obstacle[x,y]= fluence_3D[x,y,z-1]*in_block
```

```
                not_in_block[x,y,z]=(in_block-1)*(-1)


        #We check if the sigma is greater than 0 for the convolution
         if float(file_scattering_sigmas[in_water_since])>0:
             #function that performs a multidimentional gaussian filter
             new_fluence_3D[:,:,z]= ndimage.gaussian_filter(element_in_obstacle,float(
    file_scattering_sigmas[in_water_since]),mode='constant',truncate=6)

             #We look at the total fluency
             fluence_3D[:,:,z]= (fluence_3D[:,:,z-1]*not_in_block[:,:,z]+new_fluence_3D
    [:,:,z])


         else:
             fluence_3D[:,:,z]=fluence_3D[:,:,z-1]

             new_fluence_3D[:,:,z]=element_in_obstacle


         Energy_loss[z]=interpolation(Kinetic_energy,stopping_power_water,E[z-1])
         E[z]=E[z-1]-Energy_loss[z]


         if E[z]<=0:
             E[z]=0
             Energy_loss[z]=0
         in_water_since+=1

        #Only the new_fluence is in the tetrahedron and has this energy loss
         Dose[:,:,z]=(new_fluence_3D[:,:,z]*Energy_loss[z]*(not_in_block[:,:,z]-1)*(-1))
    *1.60217733*10**-13*10**6


     else:
         fluence_3D[:,:,z]= fluence_3D[:,:,z-1]
         new_fluence_3D[:,:,z]=new_fluence_3D[:,:,z-1]
         E[z]=E[z-1]
         Energy_loss[z]=0


       #the next obstacle is the area where we want a homogeneous absorption
     if z>=start_tetrahedron_z+height_tetrahedron:
         in_water=True
         #fluence by energy for the beginning of the block
         #new fluence and not fluence because fluence is the sum of different energy
    levels
         fluence_per_energy_2D=new_fluence_3D[:,:,start_tetrahedron_z-1:
    start_tetrahedron_z+height_tetrahedron]

 return Dose
```

UNIVERSITÉ CATHOLIQUE DE LOUVAIN
École polytechnique de Louvain
Rue Archimède, 1 bte L6.11.01, 1348 Louvain-la-Neuve, Belgique | **www.uclouvain.be/epl**